The September 18-20 2020 Medicane Ianos Impact on Greece

Phase I Reconnaissance Report

Geotechnical Extreme Events Reconnaissance Association

http://geerassociation.org/

To cite this report:

Zekkos D., Zalachoris G., Alvertos, A. E., Amatya P. M., Blunts P., Clark M., Dafis S., Farmakis I., Ganas A., Hille M., Kalimogiannis V., Karagiannidis A., Karantanellis E., Khan K., Kirshbaum D., Kourkoulis R., Kotroni V., Ktenidou O.-J., Lagouvardos K., Loli M., Makrinikas A., Marinos V., Manousakis J., Nikas K., Panousis D., Papathanassiou G., Saroglou C., Simopoulos A., Stanley T., Tsavalas A., Valkaniotis S. "The September 18-20 2020 Medicane Ianos Impact on Greece - Phase I Reconnaissance Report". Geotechnical Extreme Events Reconnaissance Report, GEER-068, https://doi.org/10.18118/G6MT1T.

DOI: https://doi.org/10.18118/G6MT1T

Source photo: USANews: https://inewsusa.com/world/cyclone-ianos-a-rare-medicane-batters-ionian-islands-of-greece/

List of Authors

Zekkos Dimitrios, PhD, PE, Associate Professor, University of California at Berkeley, USA (Lead), zekkos@berkeley.edu

Zalachoris George, PhD, Geotechnical Engineer, Elxis Group, Athens, Greece (co-Lead), gzalachoris@elxisgroup.com

Alvertos Antonios E., MSc, Civil Engineer, Grid Engineers, Athens, Greece, alvertos@utexas.edu

Amatya Pukar M., Researcher, Universities Space Research Association, Columbia, MD, USA, Goddard Earth Sciences Technology and Research, Columbia, MD, USA, Hydrological Sciences Laboratory, NASA Goddard Space Flight Center, Greenbelt, MD, USA, pukar.m.amatya@nasa.gov

Blunts Parker, PhD student, University of California at Berkeley, USA, parkerj@berkeley.edu

Clark Marin, PhD, Professor, University of Michigan, Ann Arbor, MI, USA, marinkc@umich.edu

Dafis Stavros, MSc, Meteorologist, National Observatory of Athens (NOA), Greece, sdafis@lmd.polytechnique.fr

Farmakis Ioannis, PhD Candidate, Queen's University, Kingston, Canada, farmakisig@gmail.com

Ganas Athanassios, PhD, Geologist, Research Director, National Observatory of Athens (NOA), Greece, aganas@gein.noa.gr

Hille Madeline, MSc student, University of Michigan, Ann Arbor, MI, USA, madhille@umich.edu

Kalimogiannis Vassilis, PhD Candidate, National Technical University of Athens (NTUA), Greece, vkallim@hotmail.com

Karagiannidis Athanasios, PhD, Meteorologist, National Observatory of Athens (NOA), Greece, thankar@noa.gr

Karantanellis Efstratios, PhD Candidate, Aristotle University of Thessaloniki (AUTH), Greece, skarantanellis@gmail.com

Khan Sana, PhD, Earth System Science and Interdisciplinary Center, University of Maryland, MD, USA; Hydrological Sciences Laboratory, NASA Goddard Space Flight Center, Greenbelt, MD, USA, sana.khan@nasa.gov

Kirshbaum Dalia, Hydrological Sciences Laboratory, NASA Goddard Space Flight Center, Greenbelt, MD, USA, dalia.b.kirschbaum@nasa.gov

Kourkoulis Rallis, PhD, Managing Director, Grid Engineers, Athens, Greece, rallisko@grid-engineers.com

Kotroni Vasiliki, PhD, Director of research, National Observatory of Athens (NOA), Greece, kotroni@meteo.noa.gr

Ktenidou Olga-Joan, PhD, Associate researcher, National Observatory of Athens (NOA), Greece, olga.ktenidou@noa.gr

Lagouvardos Kostas, PhD, Director of research, National Observatory of Athens (NOA), Greece, lagouvar@noa.gr
Loli Marianna, PhD, Geotechnical Engineer, Grid Engineers, Athens, Greece, m.loli@grid-engineers.com / Marie-Curie Fellow, University of Surrey, Guildford, Surrey, United Kingdom, m.loli@surrey.ac.uk
Makrinikas Antonios, MSc, Civil Engineer, Karditsa, Greece, amakrynikas@gmail.com
Marinos Vassilis, PhD, Assistant Professor, National Technical University of Athens (NTUA), Greecem, marinosv@civil.ntua.gr
Manousakis John, MSc, Geomatics Engineer, Elxis Group, Athens, Greece, jmanousakis@elxisgroup.com
Nikas Konstantinos, MSc, Civil Engineer, General Secretariat for Civil Protection, Athens, Greece, konstantinos.nikas@gmail.com
Panousis Dimitris, Geologist, Elxis Group, Athens, Greece, panousisdimitris@hotmail.gr
Papathanassiou George, PhD, Assistant Professor, Democritus University of Thrace (DUTH), Greece, gpapatha@civil.duth.gr
Saroglou Charalampos, PhD, Teaching & Research Associate, National Technical University of Athens (NTUA), Greece, saroglou@central.ntua.gr
Simopoulos Asterios, MSc, Head of Construction, Nea Odos S.A./Kentriki Odos S.A., Athens, Greece, Asimopoulos@neaodos.gr
Stanley Thomas, Universities Space Research Association, Columbia, MD, USA, Goddard Earth Sciences Technology and Research, Columbia, MD, USA, Hydrological Sciences Laboratory, NASA Goddard Space Flight Center, Greenbelt, MD, USA, thomas.a.stanley@nasa.gov
Tsavalas Alexandros, Data Analyst, Elxis Group, Athens, Greece, atsavalas@elxisgroup.com
Valkaniotis Sotiris, PhD, Geologist, Independent consultant, Greece, valkaniotis@yahoo.com

Table of Contents

1. Executive Summary

On September 17-20 2020 Medicane Ianos impacted Greece. The Medicane caused significant wind damage, and precipitation related impacts. The amount of precipitation during a duration of about ~48 hrs was among the highest recorded and exceeded, in certain areas, the mean annual precipitation. The extent of the affected area was very large and encompassed the western, central and southern Greece, all the way south to the island of Crete. The Ionian islands and the areas around Karditsa and Lamia in Central Greece were particularly affected.

Field deployments to collect perishable field performance data were supported by remote sensing tools and geospatial data analysis. The GEER team used optical and radar satellite imagery to generate a broad assessment of the conditions, as well as data-mined social media to identify sites of particular interest. On the ground, conventional site characterization tools were supplemented by Unmanned Aerial Vehicles to generate three dimensional models of target areas and sites. During field deployment, data collected in the field were uploaded on a shared Box folder and were projected on a web-based GIS map the next morning to facilitate collaboration among teams.

The amount of precipitation resulted in a wide variety of landsliding that included (a) landslides involving soils and fractured and weathered rocks, (b) rockslides, rockfalls and structurally controlled rock failures, as well as (c) debris flows. Just in the areas to the west of Karditsa, around Lake Plastiras, more than 1,400 landslides were mapped using satellite imagery, and some of them were documented in the field, although access in the mountainous areas affected data collection. In Cephalonia, one of a few major debris flows, a rare occurrence on the island, devastated the community of Assos. Extensive flooding was also observed throughout the affected areas nationwide. Lower-elevation areas were flooded, and portions of the town of Karditsa and surrounding communities became completely submerged. The amount of water compromised, in numerous areas, the road and railroad network by washing out roads or railroad lines, damaging the embankments that supported the pavements, or disrupting their functionality by landslide debris. Particularly pronounced was the damage to many bridges, ranging from minor damages (such as movement) to complete collapse due to foundation scour, or lateral loads by water and debris. Riverbanks and levees were also overtopped and scoured.

The extent of the affected area by Medicane Ianos far exceeds the extent of affected areas by other natural disasters, such as earthquakes or precipitation events. The diversity of damage observed also raises the need for community-level resiliency considerations, particularly in light of what appears to be a potentially new “norm” of more intense and larger precipitation events, such as this medicane. To that end, this report contributes to the condition assessment and perishable data collection from Medicane Ianos that can support engineers and community leaders in being prepared for future events. It also forms the basis for subsequent phases of investigation to better understand the causes of the recorded damage and the contributing factors.

2. Organization & Acknowledgements for the Medicane Ianos Deployment

2.1. Organization of Phase 1 reconnaissance

The landfall of Medicane Ianos on September 17 2020 triggered the interest of the National Science Foundation (NSF) sponsored Geotechnical Extreme Events Reconnaissance Association (GEER) to document the response of infrastructure to this high-intensity precipitation event.

Due to COVID19-associated travel restrictions, an interdisciplinary team of local only professionals, engineers and scientists performed field deployments to collect perishable field performance data. The field teams were supported by remote sensing tools and data analysis by Greek and US participants. Field deployments were undertaken by about five separate teams primarily during the period of September 25 to October 1 2020.

The multidisciplinary team used optical and radar satellite imagery for an overall assessment of data, and monitored social and mainstream media to identify sites of particular interest. On the ground, in addition to conventional site characterization tools, the team used extensively Unmanned Aerial Vehicles to facilitate and optimize the reconnaissance efforts, as well as to generate three dimensional models of selected areas of particular interest. Data collected in the field (i.e., routes, photos, and notes) were uploaded to a shared folder and projected on a web-based GIS map (Figure 2.1) the next day to facilitate collaboration among teams. The WhatsApp messaging tool was also used to promptly share information among team members.

2.2. Funding Resources

The work of the GEER Association, in general, is based upon work supported in part by the National Science Foundation through the Geotechnical Engineering Program under Grant No. CMMI-1826118. Any opinions, findings, and conclusions or recommendations expressed in this material are those of the authors and do not necessarily reflect the views of the NSF. Any use of trade, firm, or product names is for descriptive purposes only and does not imply endorsement by the U.S. Government. The GEER Association is made possible by the vision and support of the NSF Geotechnical Engineering Program Directors: Dr. Richard Fragaszy and the late Dr. Cliff Astill. GEER members also donate their time, talent, and resources to collect time-sensitive field observations of the effects of extreme events.

Members of the GEER team would also like to acknowledge funding by:

- The National Aeronautics and Space Administration (NASA) under grant No. 18-DISASTER18-0022.
- The European Union H2020-Marie Skłodowska-Curie Research Grants Scheme MSCA-IF-2019 (grant agreement No 895432: ReBounce-Integrated resilience assessment of bridges and transport networks exposed to hydraulic hazards).

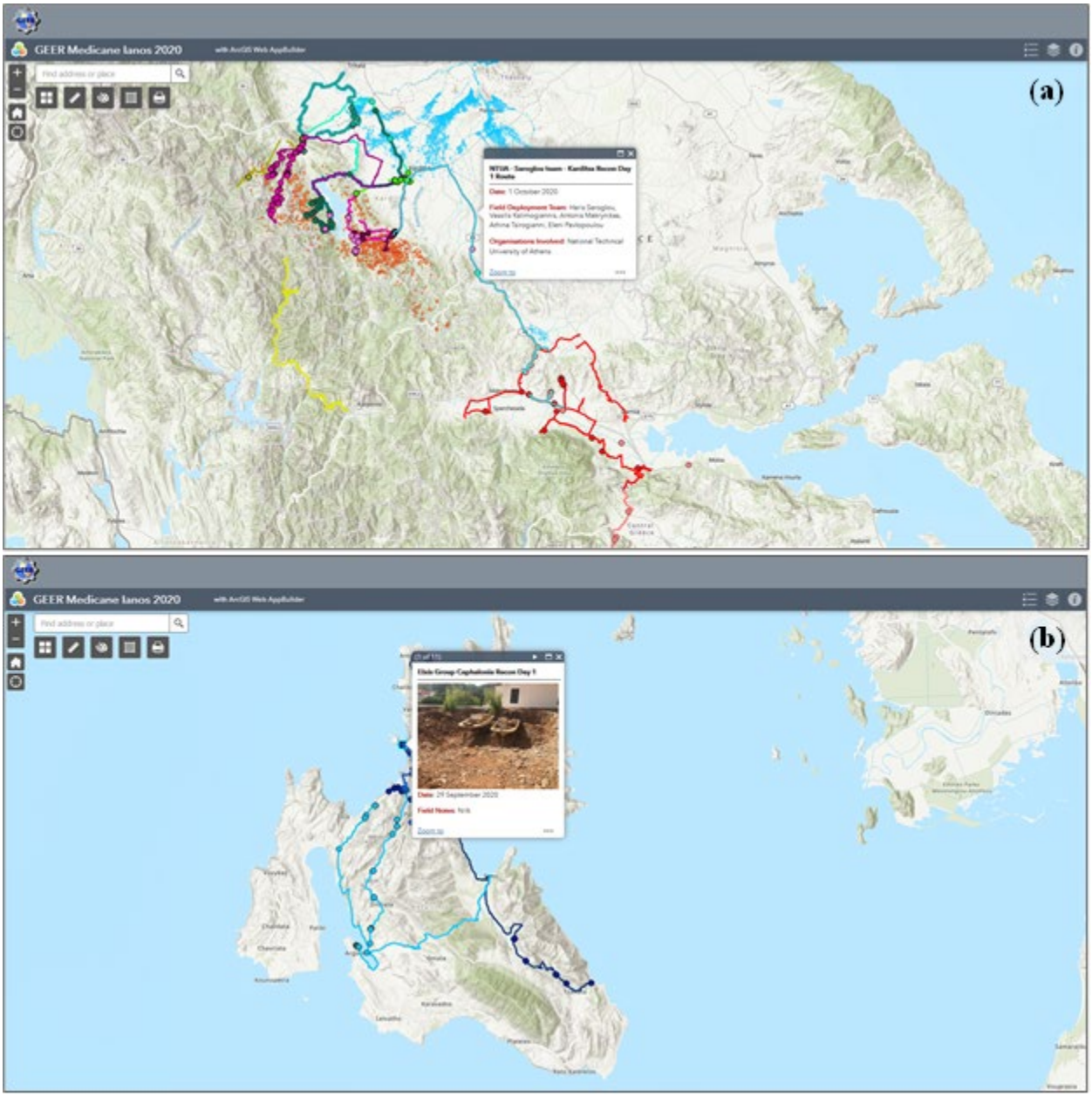

Figure 2.1. Medicane Ianos reconnaissance web-based GIS map: a) field deployment team route information, and b) site specific reconnaissance photos and notes

2.2. Collaborating Institutions, Authorities, Individuals

This report is the outcome of a collaboration among a large group of professionals and scientists from the following Greek and US-based organizations:

Universities (in order of appearance in the list of authors)
University of California at Berkeley, USA
University of Michigan, Ann Arbor, MI, USA
Queen's University, Kingston, Canada
National Technical University of Athens (NTUA), Greece
Aristotle University of Thessaloniki (AUTH), Greece
Democritus University of Thrace (DUTH), Greece

Organizations (in order of appearance in the list of authors)
Hydrological Sciences Laboratory, NASA Goddard Space Flight Center, Greenbelt, MD, USA
National Observatory of Athens (NOA), Greece
General Secretariat for Civil Protection, Athens, Greece

Consulting Firms (in order of appearance in the list of authors)
Elxis Group, Athens, Greece
Grid Engineers, Athens, Greece
Nea Odos S.A./Kentriki Odos S.A., Athens, Greece

In addition, the team would like to thank:

- Mr Charalambos Kolovos, president of the municipality Karitsa – Dolopon, for his help during the survey.
- Mr Konstantinos Pistrikas, hydraulic engineer from the city of Karditsa for his valuable directions, especially on the first days of our surveying in Karditsa, and access to past reports.
- Mr Nikos Kourtis (civil engineering consultant) and Ms Vaso Petsia (Karditsa council services) for their input regarding the construction of damaged bridges in Mouzaki.
- Mr Spyros Ligdas, deputy Mayor, and Mr Nikos Argyros, civil engineering consultant, of the municipality of Apollonion for guiding us around Valisiki, Lefkada, river scourge and providing us with photographs from the day of the flood, as well as Dr Vivi Diamantopoulou for sharing her early insights into the Cephalonia damage.
- Mrs. A. Tsirogianni, Civil Engineer, MSc and Mrs. E. Pavlopoulou, Civil Engineer, PhD candidate for their assistance in the fieldwork.

3. Introduction - About Mediterranean Cyclone Ianos

3.1. General Information

Torrential rainfall can generate landslides, flash floods, and debris flows which might become disasters, causing loss of life and damage to property and infrastructure. To respond opportunely to hydrometeorological hazards, it is necessary to assess, rapidly and accurately, damage to the affected area. Ianos medicane impacted Greece in the period from 17 to 20 September 2020. The METEO Unit of the Institute for Environmental Research and Sustainable Development (IERSD) at the National Observatory of Athens (NOA) has assigned a name to this weather system, following its practice -established in 2017- to name all meteorological systems that are expected to have significant (socio-economic) impact over Greece.

A medicane (from the words Mediterranean-hurricane) or Mediterranean Tropical-Like Cyclone is a deep barometric low which draws its energy through the transfer of heat from the warm Mediterranean waters and the release of heat with thunderstorms which develop near its center. Medicanes exhibit characteristics similar to tropical cyclones, for example, a deep warm core, an axisymmetric structure with a windless center (the "eye"), and sustained wind speeds close to hurricane-force strength. The medicane characteristics are hybrid, between tropical and extratropical cyclones. These medicanes were initially discussed in the work of Lagouvardos et al. (1999), while the most recent study by Dafis et al. (2020) provides a discussion on a series of medicanes that developed from 2005 up to 2018. Medicanes are observed in the Mediterranean with a frequency of 1.5 times per year. Specifically in Greece, we have recorded six Mediterranean Cyclones since 1982, four of which during the period 2016-2020. Therefore, this is not an unprecedented weather phenomenon in our region, but the increasing trend of occurrence and intensity in the Eastern Mediterranean raises concerns. Indeed, recent climatological studies suggest that in a warming climate, even though the number of medicane occurrences may remain stable, their intensity and duration may increase dramatically (González-Alemán et al., 2019).

Figure 3.1 depicts the axisymmetric distribution of convective clouds in a snapshot of the path of Ianos, on 17 September 2020 at 14.40 UTC. The analysis is based on satellite data from METEOSAT-11, and uses red shading to depict cloud tops that locally exceeded the height of 13 km. Overlaid (with asterisks) are shown the lightning strikes provided by the ZEUS lightning detection network operated by the METEO Unit at NOA (Kotroni and Lagouvardos, 2008). The medicane eye is evident, as well as the concurrent thunderstorms, as evidenced by the lightning occurrence. Figure 3.2 provides an estimate of the medicane track from its genesis on 12 September 2020 over Libya, up to its dissipation over the northern coasts of Egypt. This track is a first estimate based on the analysis of satellite data. The METEO unit at IERSD/NOA is currently performing an in-depth analysis of the available data (in-situ and satellite) in order to understand and describe in detail Ianos' life-cycle.

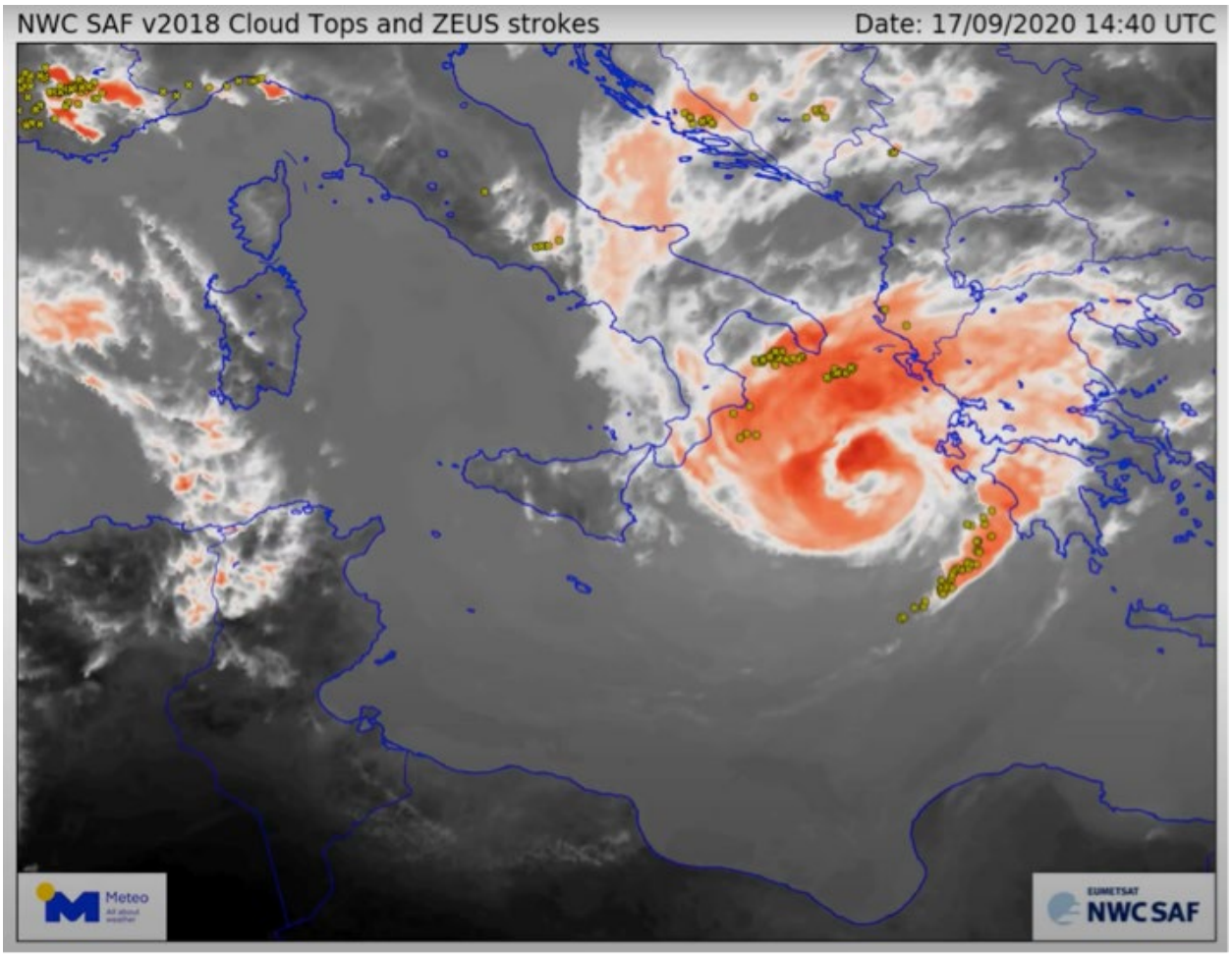

Figure 3.1. Satellite image from METEOSAT-11 on 17/09/20 at 14.40 UTC. Overlaid are shown with asterisks the lightning strikes provided by the ZEUS lightning detection network.

3.2. Precipitation data

Ianos medicane was an extreme weather event in terms of the rainfall it produced, but also in terms of its long lifetime, with tropical characteristics, and its intensity, which classify this medicane as one of the most powerful Mediterranean Cyclones recorded since 1969, i.e., since the beginning of satellite observations.

During the catastrophic passage of IANOS medicane over Greece, torrential rainfall was observed, initially in Western and then in Central Greece, which resulted in extensive floods. Figure 3.3 presents the highest rainfall accumulations during the period 17-19 September 2020. The rainfall data are provided by the network of automatic meteorological stations operated by the METEO Unit at NOA (Lagouvardos et al., 2017).

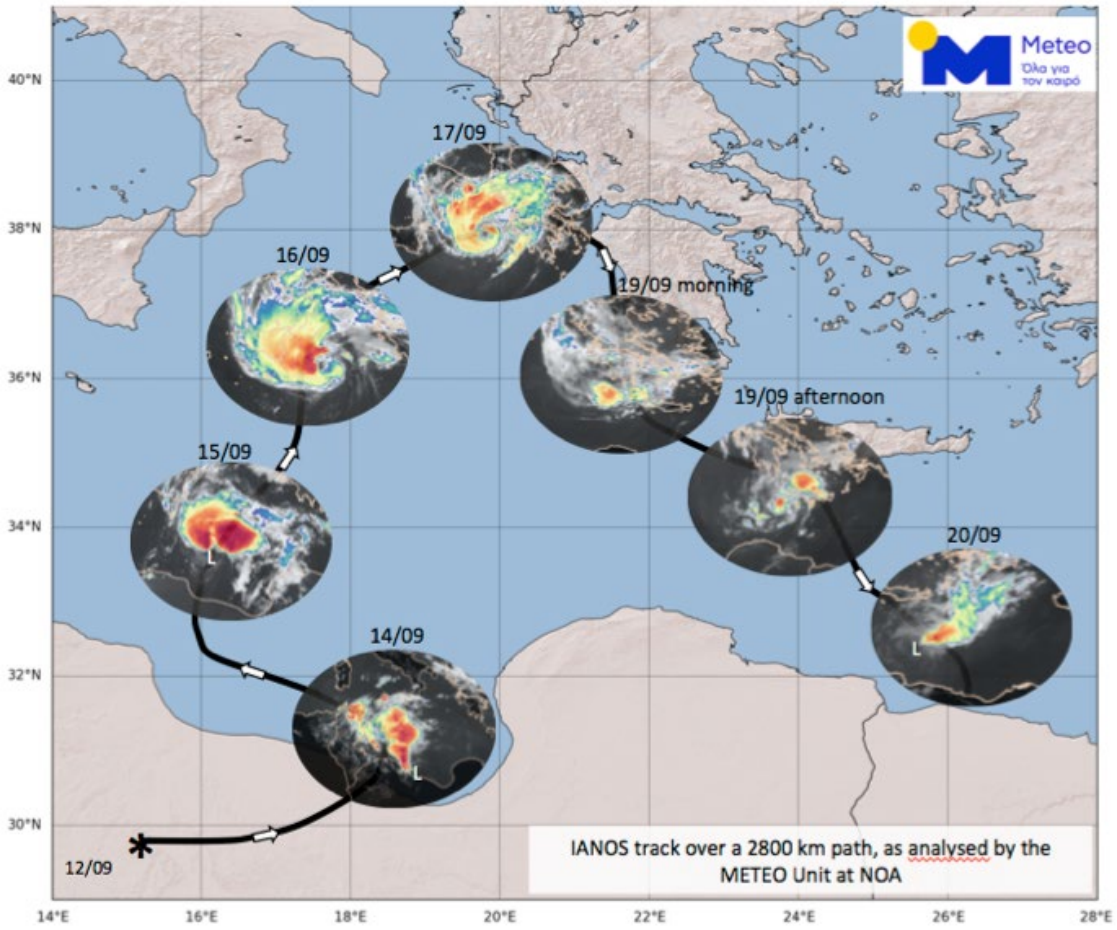

Figure 3.2. Initial estimate of IANOS track over a distance of 2,800 km, as analyzed by the METEO unit of IERSD/NOA.

In Ithaki, an island in the Ionian Sea in Western Greece, the total accumulated rainfall (storm total) as per METEO was 228 mm. Nearby stations over western continental Greece recorded more than 120 mm in less than 24 hours. Heavy rainfall, exceeding 180 mm, was also estimated over the maritime areas in the Ionian Sea from the analysis of satellite data as estimated by the NWCSAF (Figure 3.4). Over Central Greece, METEO station Pertouli (Thessalia) recorded 317 mm during the period 17-19 September 2020, while storm maxima of 274 mm and 213 mm were recorded in the same time interval at Mouzaki and Karditsa stations, respectively. The daily accumulated rainfall recorded during the Ianos passage over Greece was among the highest recorded during the last 10 years by the METEO network of surface meteorological stations. For comparison, we note the following all-time daily extremes: 417 mm at Makrinitsa (10 December 2019, Central Greece), 393 mm at Gardiki (28 October 2012, Central Greece), 373 mm and 364 mm at Chania prefecture (25 February 2019, Crete island, see Lagouvardos et al, 2020). Although the Ianos daily values did not exceed these all-time maxima, they do figure among the very highest values of the past decade and can be considered as extremes on a local and national scale.

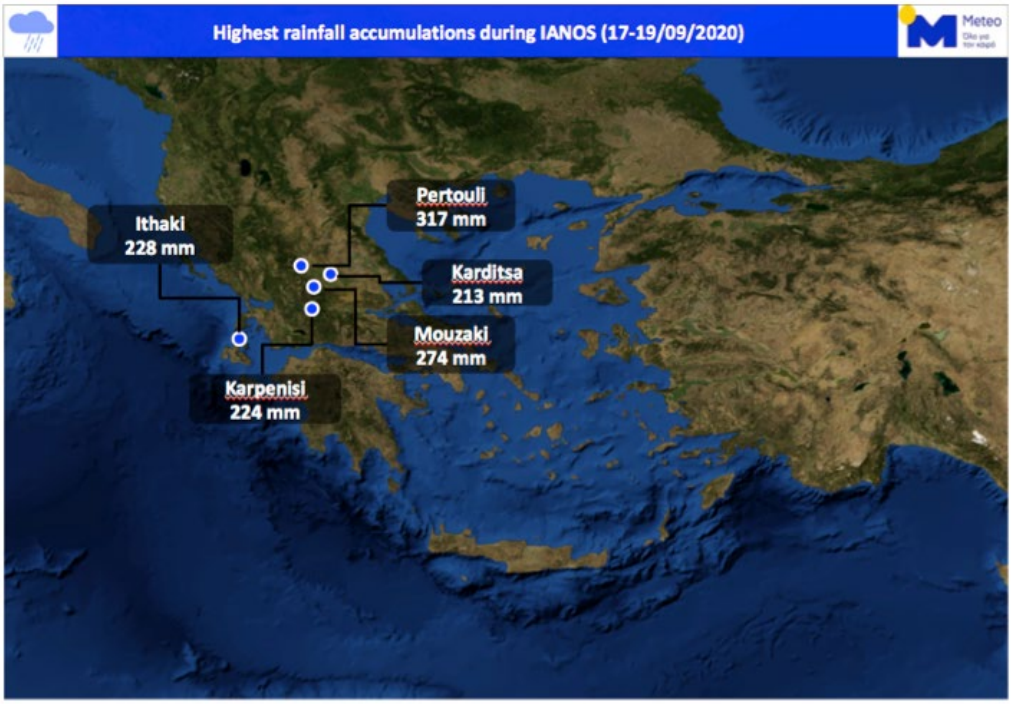

Figure 3.3. Highest rainfall accumulations during IANOS, as reported by the METEO unit at NOA.

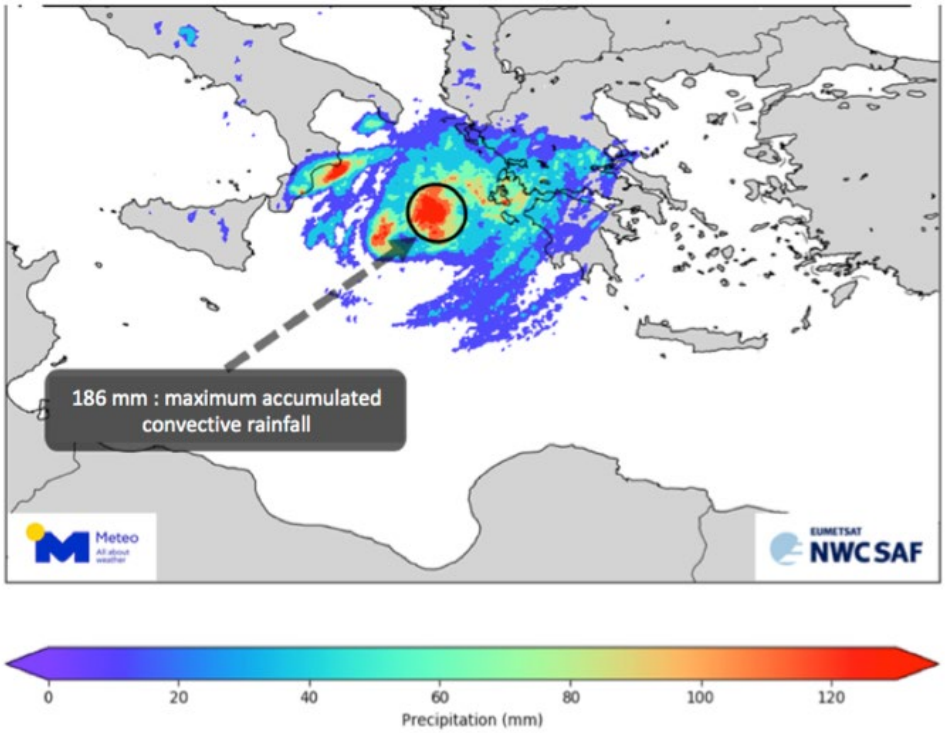

Figure 3.4. Accumulated convective rainfall (in mm) in the time interval 00.00 UTC 17 September 2020 up to 08.15 UTC, 18 September 2020, as estimated by the NWCSAF (http://www.nwcsaf.org/) product.

3.3. Precipitation Estimates based on Global Precipitation Measurement (GPM) Satellite Data

Precipitation data from the Global Precipitation Measurement (GPM) satellite mission is publicly available from NASA. We compare intensity-duration records at four locations. We average reported 30-minute rainfall amounts at 0.1x0.1 km grid cells covering each area of interest (Huffman et al., 2019). Thirty-minute rainfall time series over Lefkada, Cephalonia and Zakynthos islands, as well as the mountains southwest of Karditsa, are presented here (Figure 3.5). Overall, the average intensity of rainfall from the four areas during the medicane are similar (~5-7 mm/hr), however the duration and peak of intensity was highest for the western Ionian islands compared to central Greece at Karditsa. The intensity of rainfall reached peak rates of ~23 mm/hr during the period that the medicane affected the island of Cephalonia and notably little to no rainfall occurred in the two weeks prior for all regions. The duration of rainfall over the mountains southwest of Karditsa was approximately half of the rainfall experienced on the Ionian islands. However, the peak storm intensity reached 14.67 mm/hr, which is similar to the peak intensity measured in the southern Ionian islands. The timing of peak storm intensity during the duration of storm is variable at each location, as well as the volume of antecedent rainfall prior to the storm peak (Figure 3.5). For example, precipitation over Lefkada reached peak intensity at the end of the storm (i.e. after the greatest volume of rain fell (263.6 mm)), but the total storm event volume was ~100 mm less than total rainfall over Cephalonia, which experienced the rainfall highest intensities during the midpoint of the storm duration. It is worth mentioning that the storm total reported by the rain gauge at Lefkada was 109.8 mm (compared to the 277 mm by GPM), while, at the area of Karditsa, the measured storm totals were 212.4mm, 274.6mm and 317mm, in the city of Karditsa, at Mouzaki and Pertouli (mountainous area northwest of the city), respectively, compared to the estimated 155.67 mm by GPM. A comparison between rain gauge measurements and GPM estimates of precipitation is under way in order to better describe the spatiotemporal distribution of rainfall during the passage of the medicane over the affected areas.

3.4. Landslide Prediction using LHASA

The global landslide nowcast produced by the Landslide Hazard Analysis for Situational Awareness (LHASA) model version 2.0 merges dynamic observations of precipitation and soil moisture from the GPM and SMAP missions with static variables to produce a global map of relative landslide hazard in nearly real time. LHASA showed high levels of landslide hazard on September 17 in the Ionian Islands, especially Cephalonia (Figure 3.6). The probability of landslide occurrence increased on the following day, with potentially affected areas expanding to include Lefkada, the Adriatic coast, and much of the interior. The hazard rapidly declined in the following days.

3.5. Social Media Data Mining for Condition Assessment

In addition to resources made available through mainstream media, the GEER team also collected social media data to identify affected areas and occurrence of particular events of interest. This was done on an ad-hoc basis by members of the GEER team, but also on a concerted basis data mining effort through Twitter by Elxis Group. A total of 2,154 tweets were collected over the course of Ianos' passage through Greece. The tweets contained the following keywords: "cyclone", "mediterranean", "bad weather" and "landslide". Figure 3.7 shows a time history of tweets. The drop-off of Twitter activity is evident following the passage of the Ianos. Figure 3.8 is a collection of example tweets used to evaluate the conditions on the ground.

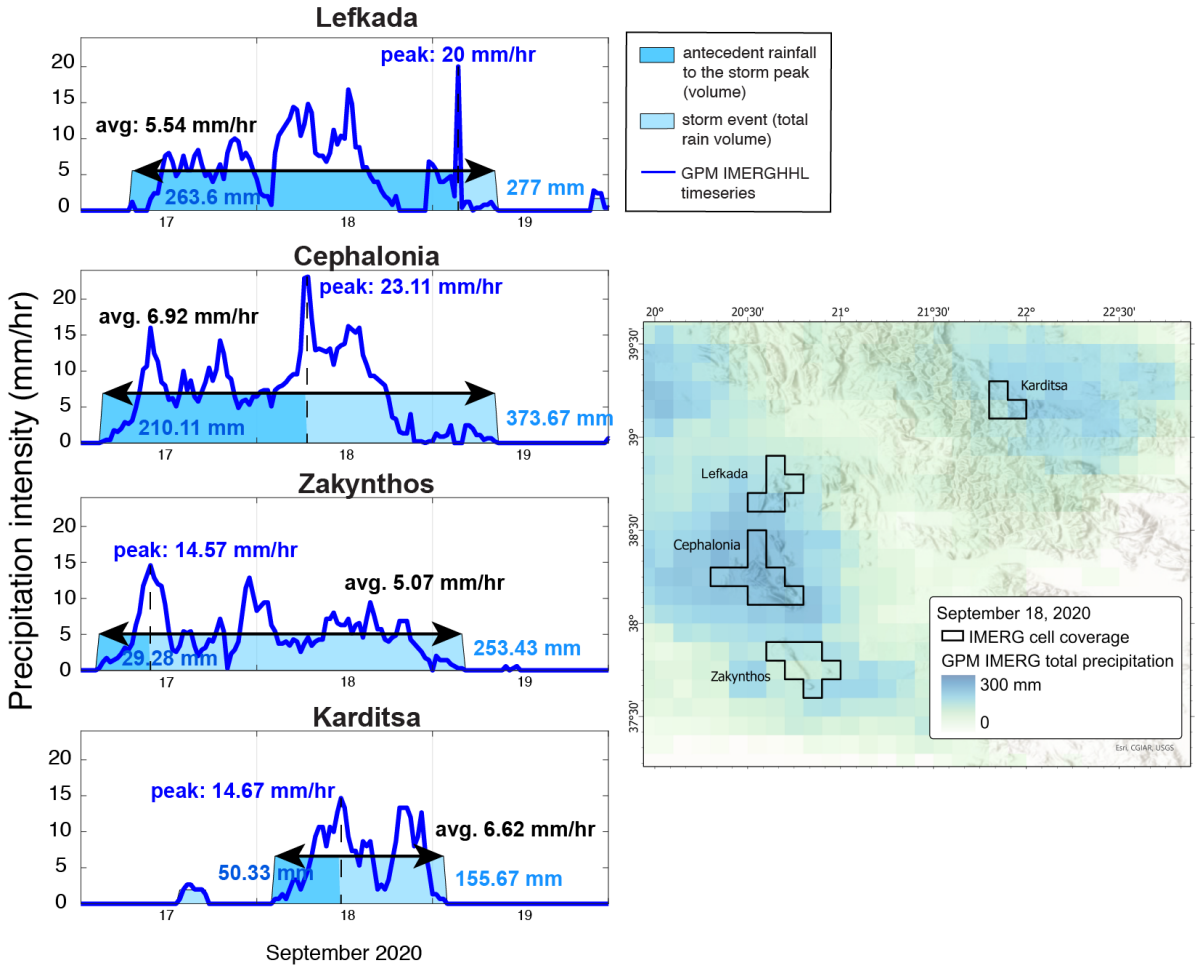

Figure 3.5. Precipitation intensity timeseries from NASA's GPM IMERG 30-minute Late product at four locations in Western Greece. Each location time series represents the average of 3 - 9 data cells.

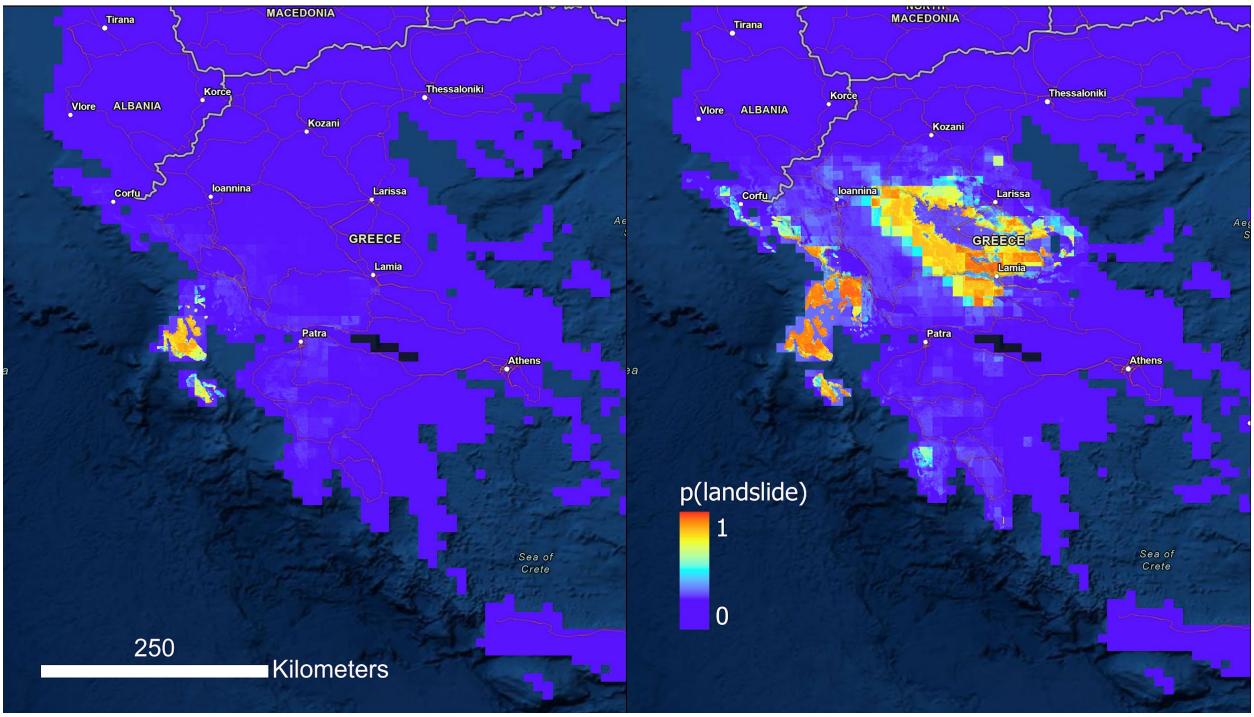

Figure 3.6. 1-day LHASA model landslide probability predictions for September 17 and September 18, 2020. (UTC)

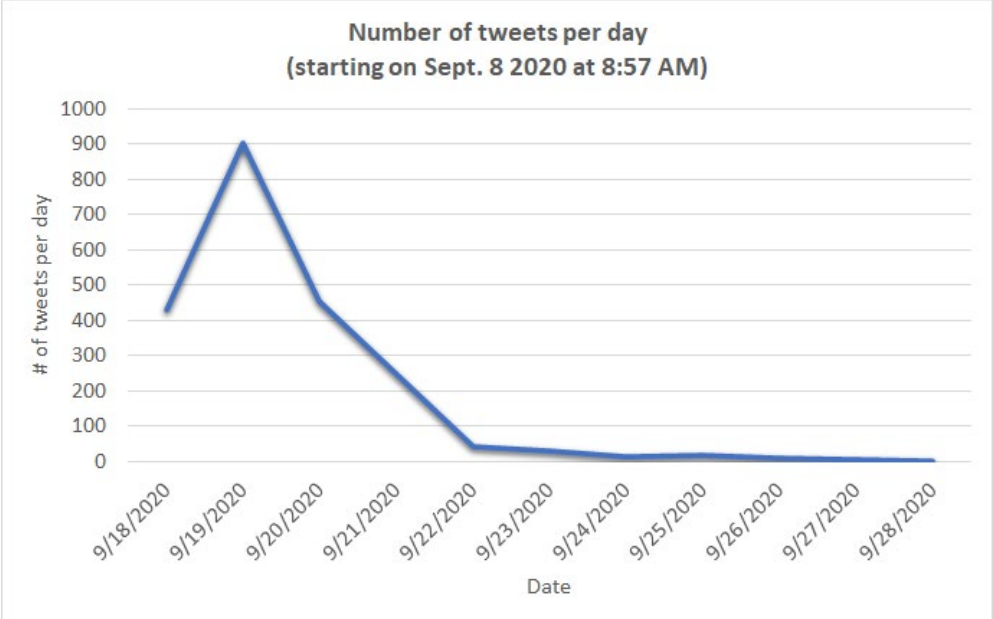

Figure 3.7. Twitter activity related to Ianos Medicane (in Greek language).

Figure 3.8. Example of tweets by locals describing the conditions in their area.

4. Affected Areas

4.1. General Description

Medicane Ianos caused severe damages as it stalled over western Greece. The most significant impacts occurred in the Ionian Islands, particularly the island of Cephalonia, in the mountains and plains of Thessaly, as well as in Fthiotida, along Spercheios river valley. Four people lost their lives due to flash flooding and one is reported missing (Wichmann, 2020; BBC News, 2020). Throughout the country, the Fire Service received 630 calls for help and proceeded to 450 rescue operations and 120 flood water pumping operations in urban areas (European Commission/Emergency Management Service – Mapping, 2020). Extensive damages were reported in agricultural land, and the urban areas of Farsala, Mouzaki and Karditsa. Numerous landslides and debris flows were reported, particularly in the mountainous region of Karditsa. The village of Assos in Cephalonia was buried under nearly two meters of debris. Several bridges collapsed and river scouring was extensive. Railroads as well as road networks were severely affected. Total economic and insured losses are expected to reach USD100 million (Aon Benfield, 2020). The map in Figure 4.1 shows the flooded areas of the Prefecture of Karditsa on 20 September 2020, as estimated by the European satellite Sentinel-2, while Table 1 tabulates the consequences in the area Karditsa, as estimated by Copernicus Emergency Management Service – Mapping. Figure 4.2 shows an example of the flooded area in the village of Mouzaki that caused damage to bridges, extensive river scouring and collapse of the local medical clinic.

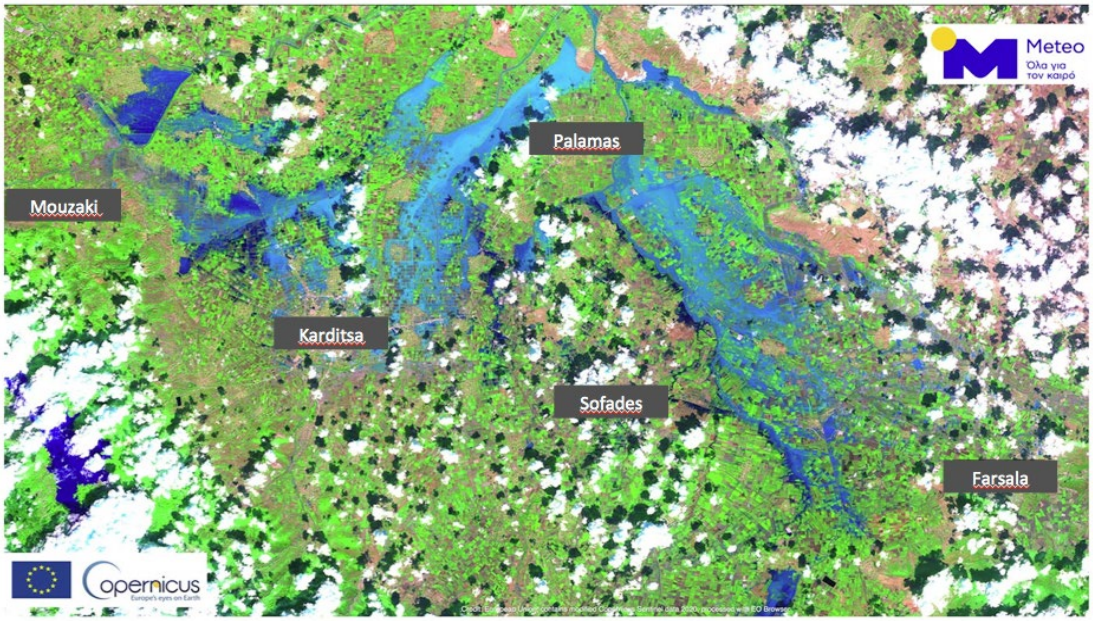

Figure 4.1. High resolution satellite image (10-m pixel resolution) from the European satellite Sentinel-2, at noon 20 September 2020. Flooded areas are shaded in blue (on the bottom left, Lake Plastira, about ~24 square km can be seen in deep blue), while clouds are white, forest and rural areas are green, and rocky/hilly areas are brown.

Table 4.1. Consequences within the Area of Interest (AOI) (Karditsa), as documented by the E.U. Copernicus Emergency Management Service - Mapping flood delineation product in the area of Karditsa (EMSR465) - situation as of September 20th 2020 (product provided by the General Secretariat for Civil Protection - Directorate for Emergency Planning and Response)

Consequences within the AOI				
	Unit of measurement		Affected	Total in AOI
Flood trace	ha		24398.4	
Flooded area	ha		4803.7	
Previous Flooded area	ha		5980.7	
Estimated population	Number of inhabitants		364442	
Settlements	Residential Buildings	ha	629.8	13452.9
	Industrial buildings	ha	192.5	1636.0
	Museums and libraries	ha	2.4	176.7
	Sports halls	ha	0.0	183.1
Transportation	Airfield runways	km	0.7	8.2
	Highways	km	0.0	17.6
	Primary Road	km	30.6	517.9
	Secondary Road	km	38.6	476.3
	Long-distance railways	km	40.8	225.2
Facilities	Constructions for mining or extraction	ha	4.4	358.6
	Dams	km	0.0	0.4
Land use	Arable land	ha	27680.8	248292.1
	Permanent crops	ha	40.9	1395.4
	Pastures	ha	935.1	6415.9
	Heterogeneous agricultural areas	ha	504.9	17650.3
	Forests	ha	34.2	26817.5
	Shrub and/or herbaceous vegetation association	ha	110.4	64074.5
	Open spaces with little or no vegetation	ha	0.0	1447.5
	Inland wetlands	ha	5.9	496.4
	Other	ha	1066.5	20622.2

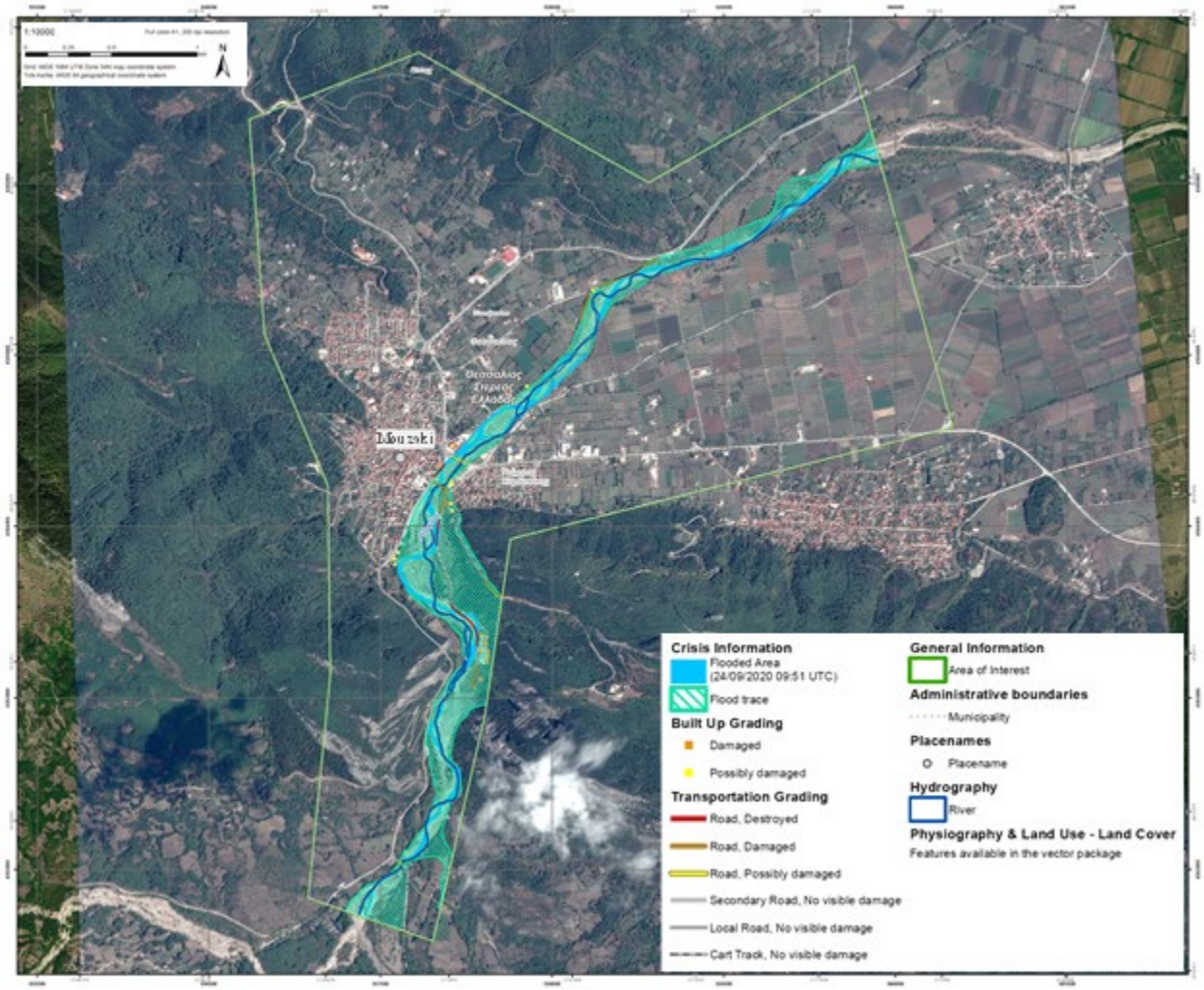

Figure 4.2. E.U. Copernicus Emergency Management Service - Mapping damage grade assessment product in the area of Mouzaki (EMSR465), situation as of September 24 2020 (product provided by the General Secretariat for Civil Protection - Directorate for Emergency Planning and Response)

4.2. Cephalonia and Lefkada Islands

4.2.1. Geology and Geomorphology

Cephalonia is part of the Ionian islands and is located at the westernmost part of Greece. Geologically, the island is within the outermost edge of the External Hellenides zone, which is an active part of the ongoing subduction of the African plate under the Eurasian plate. The bedrock of the island consists of two main formations (Figure 4.3):

1. The Pre-Apulian unit, which covers most of the island and consists mainly of a thick sequence of limestone and dolomite, overlain by a much thinner sequence of marl and pelite, and
2. The Ionian unit, which covers part of the southeastern coastal areas of Cephalonia and the entire Ithaca island and consists of limestone, shale, and breccia. The contact between the two units is defined by a thrust of NNW-SSE direction.

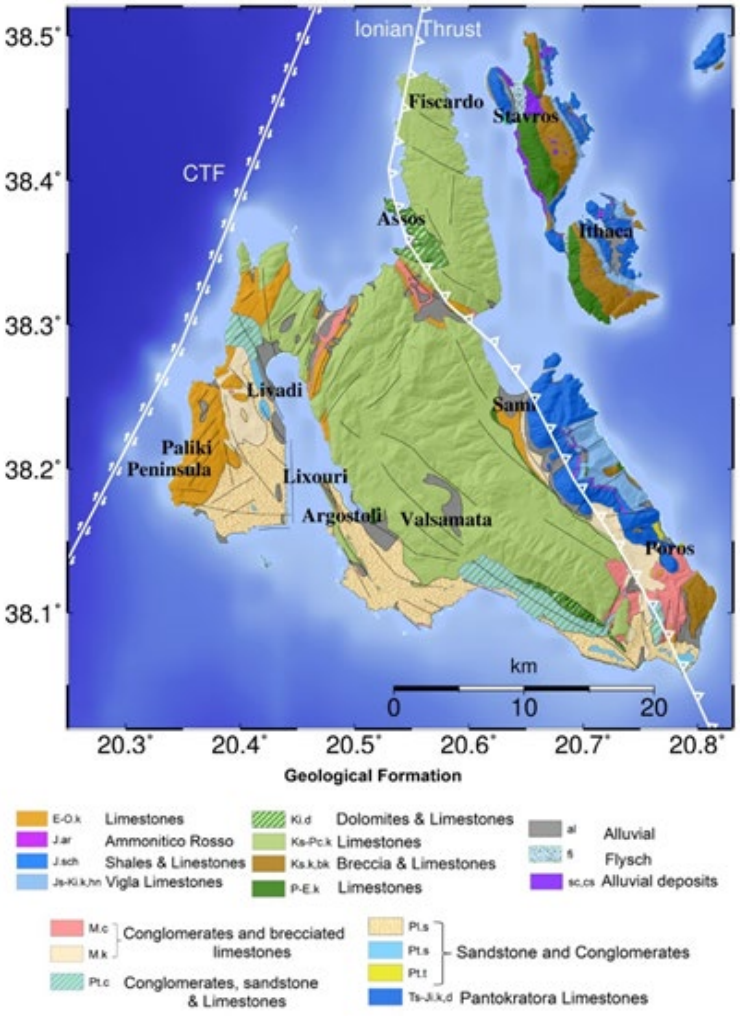

Figure 4.3. Geological map of Cephalonia (Briole et al., 2015)

The basement is overlain by extensive outcrops of sedimentary deposits in the southern and eastern part of the Paliki peninsula and the south part of the main island (Figure 4.3). These deposits consist of terra rosa and alluvial fans, mainly deposited along the stream channels. The dominance of carbonate rocks in combination with favorable climate conditions have facilitated the formation of karst units especially in the north and central part of the island. Dolines, sinkholes and caves can be found at several locations. In particular, the Erissos Peninsula is dominated by an extensive, and partially karstified, planation surface. The gradual tectonic uplift of the island has resulted in the formation of erosional planation surfaces on the carbonate bedrock.

The geomorphology of Cephalonia island is characterized by steep slopes, especially along its western shoreline (Figure 4.3). Indeed, the majority of the island's coastline is characterized by steep slopes. Ridges are arranged in a NNW-SSE direction. The main mountain mass of Cephalonia island is Aenos (1630 m), oriented in a NW–SE direction. The principal water divide has the same direction, with the main flow directions towards Sami Bay in the NE, and Poros in the SW. (Figure 4.4).

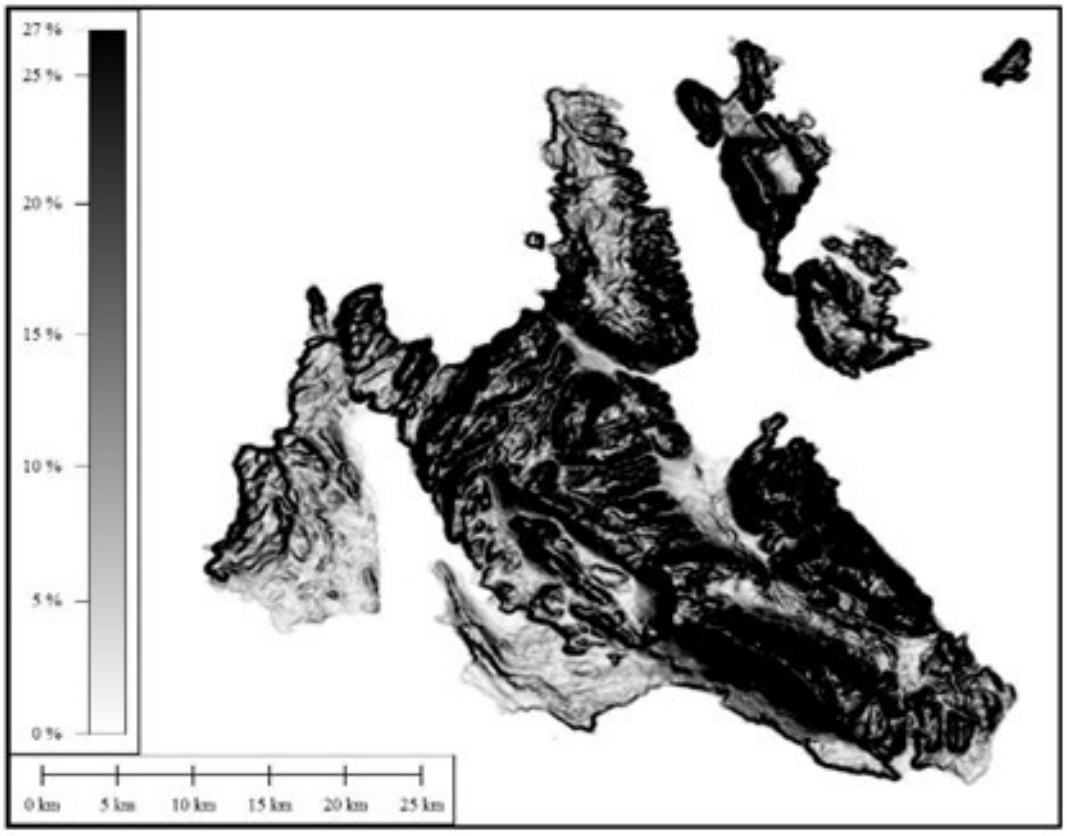

Figure 4.4. Slope map of Cephalonia and neighboring islands (GEER, 2014)

The island of Lefkada is located approximately 10 km north of Cephalonia. Geologically, similar to Cephalonia, it belongs to the External Hellenides zone, and its main geologic formations include

sedimentary rocks of the Pre-Apulian and Ionian zones. Most of these units consist of limestones, dolomites, and marls (Figure 4.3). Coastal deposits are found in the northern part of the island, and in the plains of Nydri and Vassiliki, while flyschoid sediments are found along the Dragano valley and the slopes of the eastern and northern Vassiliki valley. Pockets of scree and talus cones are encountered throughout the island (Figure 4.3).

Due to the transform fault system (Cephalonia Transform Fault, CTF) that runs parallel to the western coast of Lefkada and Cephalonia islands (Scordilis et al., 1985), as well as its onshore sub-parallel fault, i.e., the Athani-Dragano fault (Rondoyanni et al., 2012), the island is characterized by steep mountainous morphology, and a particularly landslide-prone western coastline.

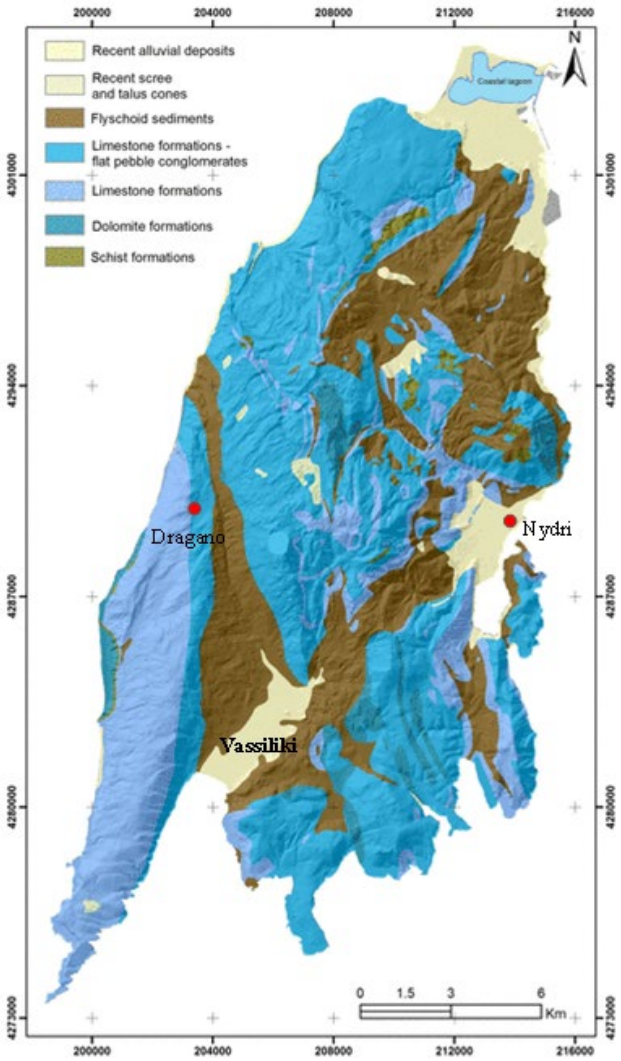

Figure 4.5. Geological map of Lefkada (Tsangaratos et al., 2018)

4.2.2. Brief Description of Damages

Cephalonia island was heavily impacted by Medicane Ianos. In particular, the northern part of the island towards Erissos peninsula, was the hardest hit. Flooding was extensive with the towns of Ag. Efimia and Fiskardo being partially inundated. Debris flows occurred in several locations across the island. Often the debris flows covered wide areas (~40-70 m in width), while typically the average size of the pebbles/debris reached 20-50 cm (Figure 4.6d). The small, coastal village of Assos was covered by approximately 1.5 m of earth/debris material (Figures 4.6a and 4.6b). Moreover, the earth flows were often associated with road embankment failures (Figure 4.6c). The latter was also observed in cases of severe riverbank erosion/scour. The road network of the island was damaged and/or obstructed in several locations due to landslides, while a critical simple-span reinforced concrete bridge near the village of Agkonas collapsed (Figure 4.6e), heavily impacting the transportation network of the island.

Figure 4.6. Characteristic damages in Cephalonia island following Medicane Ianos: a) Riverbank Erosion, b) debris flow within a rural community, c) road embankment failure, d) extensive debris flow, e) bridge collapse.

Lefkada island was less severely affected by Medicane Ianos. In the southern part of the island, and particularly the town of Vassiliki and the surrounding lowland-situated villages, extensive

flooding occurred (Figure 4.7), while minor erosional features and road embankment failures were observed along the river bank of the Vassiliki valley (Figure 4.8). Sediment movement and landslide activity was also observed along the western coastline of Lefkada where significant landsliding occurred during the 2015 Lefkada earthquake.

Figure 4.7. a) Flooding along the seaside at Vasiliki village, Lefkada, as photographed by an eye witness on the day vs. b) reference photo from GoogleMaps (38.627504°N, 20.607268°E). c) flooding at the same spot on the day vs. d) reference photo (38.627504°N, 20.607268°E).

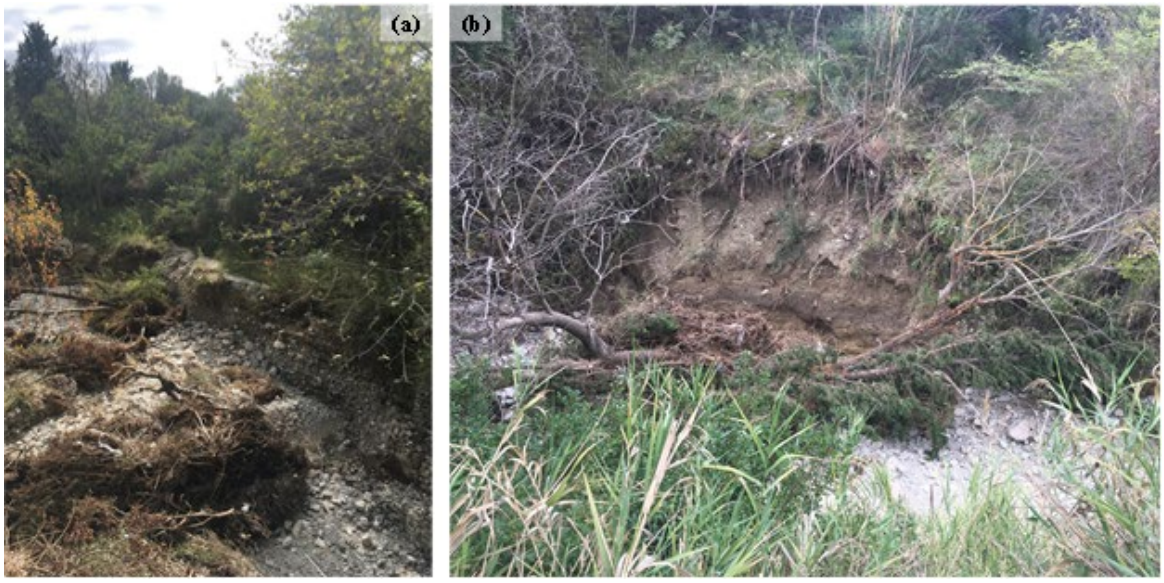

Figure 4.8. Riverbank erosion features in Vassiliki valley, Lefkada: a) 38.6658694°N, 20.6202861°E; b) 38.6638861°N, 20.624483°E

4.2.3. Areas Covered during Reconnaissance

- Cephalonia Island

A reconnaissance team consisting of George Zalachoris and John Manousakis of ElxisGroup was deployed to Cephalonia island on 9/29/2020. The field work lasted for three days, during which most of northern Cephalonia was visited. For the optimal documentation of the damages, apart from collecting typical reconnaissance data (i.e., photos, notes, etc), the field deployment team employed aerial photography and videography, as well as aerial mapping using Unmanned Aerial Vehicles (UAVs). Therefore, remote, and not easily accessible areas were covered. The reconnaissance work during the three-day deployment is summarized as:

Day 1

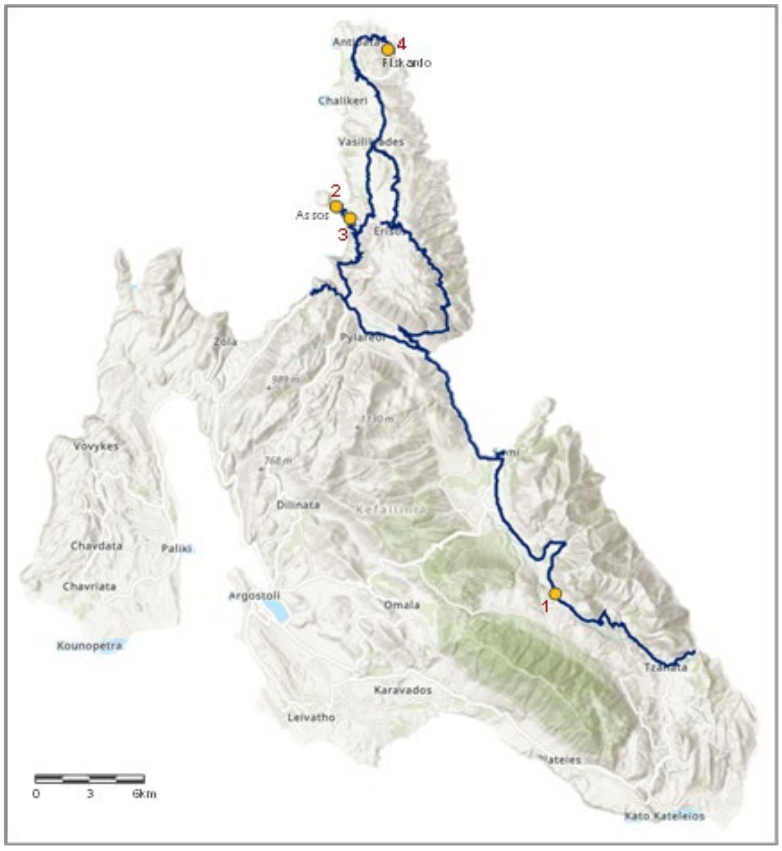

Figure 4.9. Area covered during day 1 of reconnaissance mission to Cephalonia

Route:

- Port of Poros to the coastal town of Sami;
- Sami to the village of Assos, through Divarata;
- Assos to the town of Fiskardo;
- Fiskardo to Sami, through the villages of Vary and Komitata

Field Work Performed:

1. Reconnaissance along the E.O. Samis-Tzanata;
2. Documentation of damages within Assos village;
3. Aerial videography of debris flow outside of Assos village;
4. UAV-enabled mapping of debris flow outside of Fiskardo village.

Day 2

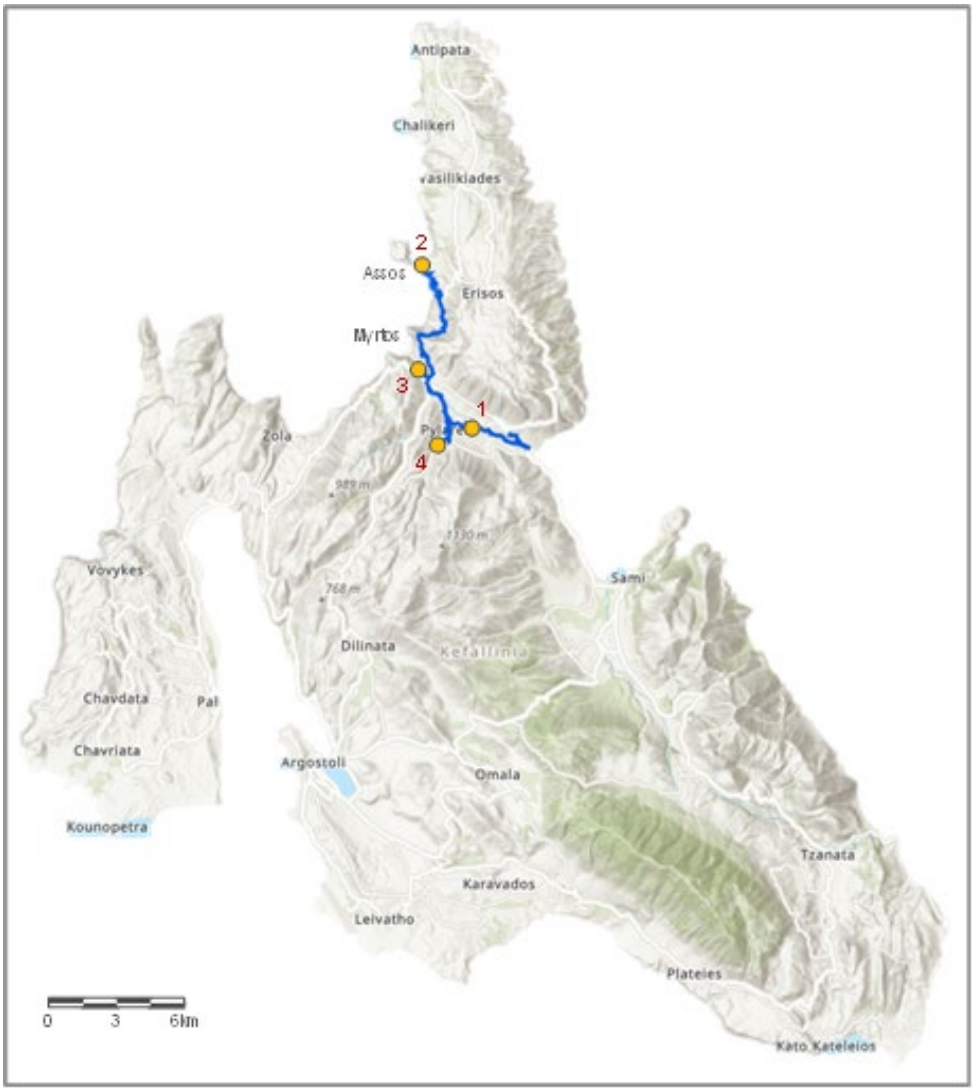

Figure 4.10. Area covered during day 2 of reconnaissance mission to Cephalonia

Route:

- Ag. Efimia to Assos;
- Assos, through Divarata to Myrtos Beach;
- Myrtos Beach to Ag. Efimia, through the Pylareoi region.

Field Work Performed:

1. Reconnaissance along the E.O. Samis-Sinioris;
2. Detailed UAV-enabled mapping of the debris flow and the entire village of Assos;
3. Reconnaissance and aerial photography/videography of the landslides and road embankment failures along the road leading to Myrtos Beach;
4. Aerial photography/videography of the entire earth/debris flow from the hills of Pylareoi region to the town of Ag. Efimia.

Day 3

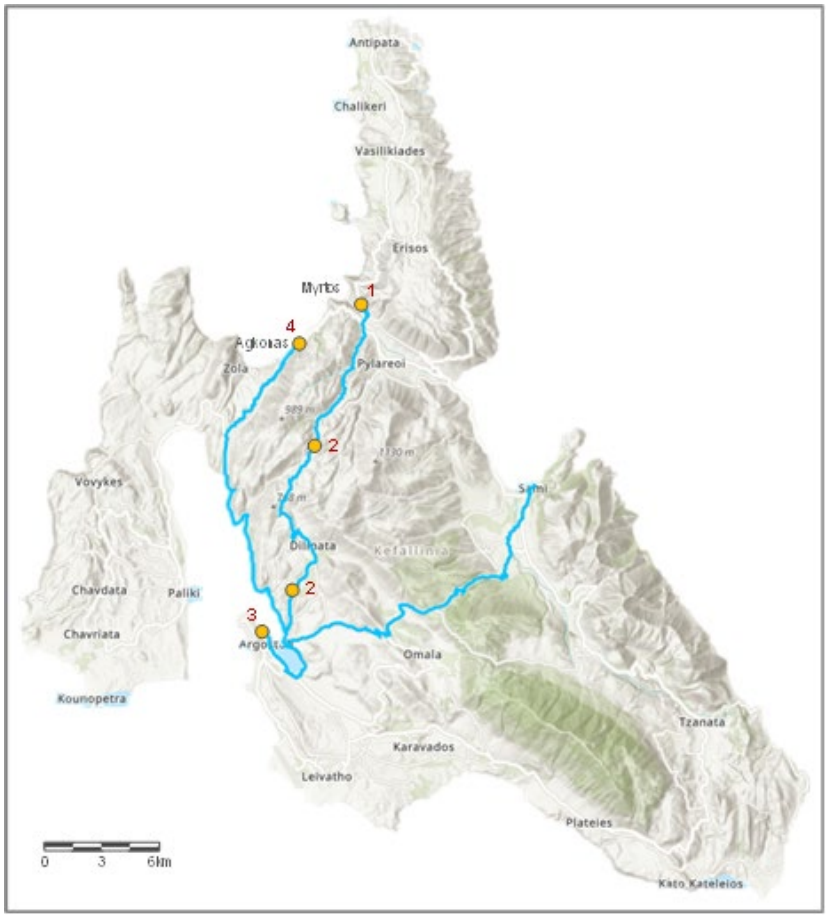

Figure 4.11. Area covered during day 3 of reconnaissance mission to Cephalonia

Route:

- Sami to Myrtos Beach;
- Myrtos Beach to the town of Argostoli, through Drakata and Dilinata;
- Argostoli to the collapsed simple-span bridge on E.O. Argostoliou-Fiskardou, through Farsa and Agkonas villages;
- Agkonas village to Sami, through Drapano-Razata-Mt. Ainos.

Field Work Performed:

1. UAV-enabled mapping of the landslide at Myrtos beach;
2. Reconnaissance along E.O. Faraklaton-Ag. Efimias;
3. Documentation of damages along the cruise-ship-deck promenade of the town of Argostoli;
4. Detailed UAV-enabled mapping of the collapsed bridge on E.O. Argostoliou-Fiskardou.

- Lefkada Island

A reconnaissance team consisting of George Zalachoris and John Manousakis of ElxisGroup, and Olga-Joan Ktenidou of the National Observatory of Athens was deployed to Lefkada island on 10/02/2020. The field work lasted for two days, during which major part of southern Lefkada was visited (Figure 4.12). The field work consisted of reconnaissance along the riverbanks and hillsides of Vassiliki valley, as well as along the steep mountainous slopes of the landslide-prone western coastline of the island.

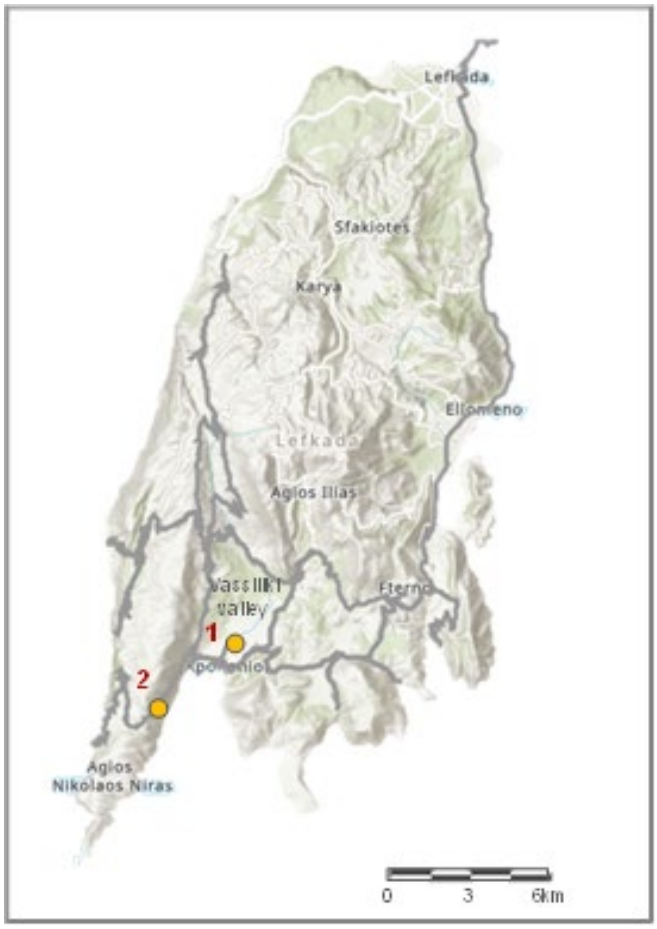

Figure 4.12. Area covered during the reconnaissance mission to Lefkada

4.3. Lamia Region

4.3.1. Geology and Geomorphology

Spercheios river basin is situated in eastern central Greece. Its primary boundaries are Othrys mountain in the north, Oiti Mountain in the south, Timfristos mountain in the west, and Maliakos Gulf in the east (Figure 4.13). Spercheios river basin covers an area of approximately 2000 km^2.

The main geological formations in the southern and western parts (Oiti and Tymfirstos mountains, respectively) of the basin are limestones and flysch, while in the northern and eastern parts of the basin (Othrys mountain), the main formations are limestone and schist/ophiolites. The lowland of Spercheios river valley is covered by quaternary deposits, i.e., conglomerates, lacustrine deposits, and quaternary alluvial deposits.

Spercheios river valley is characterized by steep slope gradients, particularly in the south part of the basin, while the north part has gentler slopes and lower elevations. Downstream, the river is transformed gradually into a lowland relief, where cases of severe flooding have been recorded. The largest part of the area is characterized by medium to high morphological slopes i.e. from 12% to 35%. The southwestern area of the basin exhibits the higher morphological slope inclination (>35%), while most of the riverbed flows through a lowland part.

4.3.2. Brief Description of Damages

Along the Spercheios river valley, in the region between the town of Makrakomi and the city of Lamia, significant damages were reported. These consisted of extensive flooding on both sides of the valley, erosion/scour of riverbanks (Figure 4.14a), road embankment failures (Figures 4.14d and 4.14e), bridge foundation erosion (Figure 4.14c), and tunnel portal failures. The infrastructure damages seem to be concentrated in the area defined by the villages of Stirfaka-Lygaria-Leianokladi-Zilefto-Moschokaria, while the south side of the river valley was affected primarily by flooding.

4.3.3. Areas Covered during Reconnaissance

Two separate expeditions to the region were made. The first (“Expedition 1”) took place on 09/25/2020 by George Zalachoris of ElxisGroup, while the second (“Expedition 2”) was undertaken on 10/01/2020 by an NTUA team led by Dr. C. Saroglou, whose members consisted of: V. Kallimogiannis, A. Makrinikas, A. Tsirogianni, and E. Pavlopoulou. The reconnaissance work during these deployments is summarized in the following paragraphs.

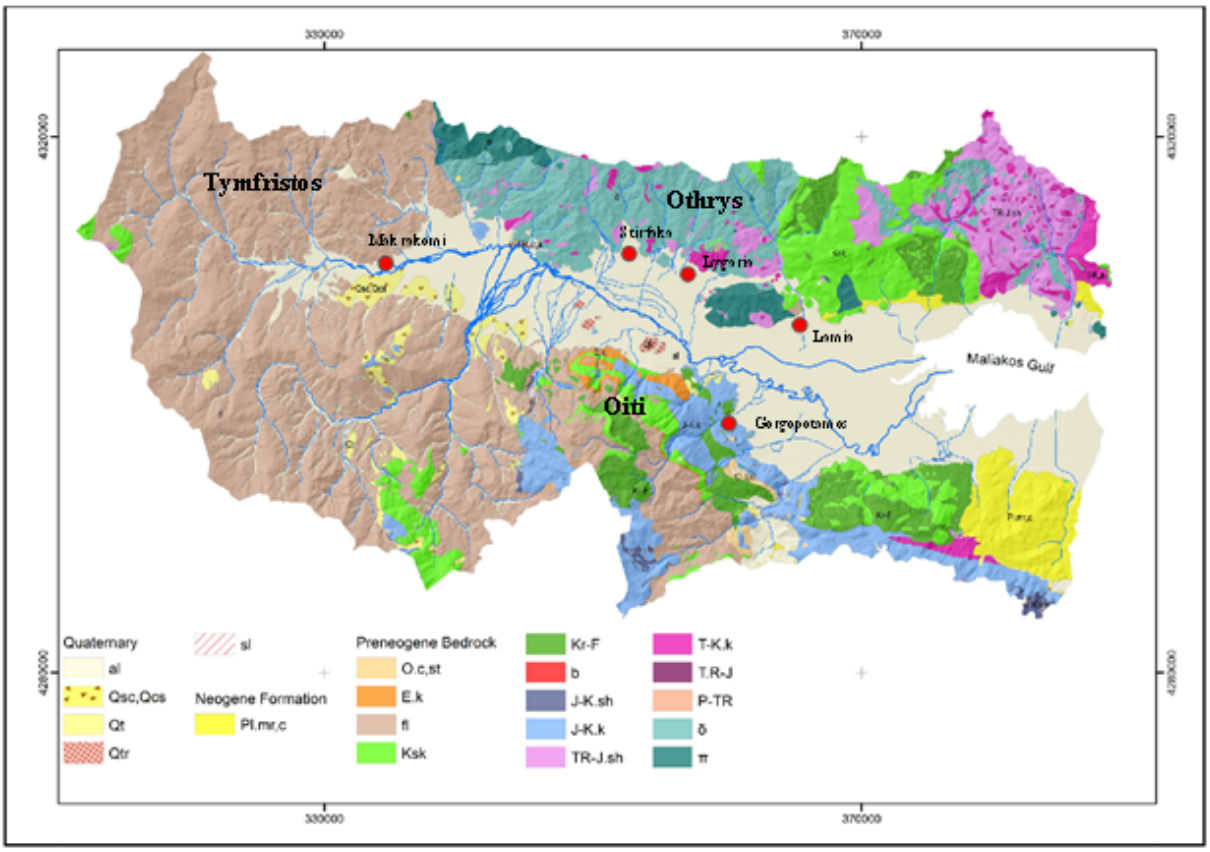

al: Alluvial deposits	**fl:** Flysch (sandstones, graywackes, conglomerates, marls)	**T-K.k:** Dolomite and limestone (Triassic-Jurassic)
Qsc, Qcs: Talus cones and scree	**Kr-F:** Upper-cretaceous Flysch	**T.R-J:** Radiolarite (Triassic-Jurassic)
Qt: Fluvial terraces	**Ksk:** Upper-cretaceous transgressive limestones	**P-TR:** Schists, Sandstones, Limestones (Upper Permio Lower Triassic
Qtr: Terra Rossa	**b:** Bauxite	**Ol:** Ophiolite:
Pl.mr,c: Neogene Formation (marls, conglomerates etc)	**J-K.k:** Limestones (Jurassic-Lower Cretaceous)	**δ:** Diabas-Dolerite. Tuffs of igneous basic rocks
O.c,st: Molassik sediments	**J-K.sh:** Shale-Sandstone-cherty formation (Jurassic)	**π:** Peridotite
E.k: Thinly bedded limestones (Eocene)	**TR-J.sh:** Shales-cherts group with ophoplites (Up Triassic-Jurassic)	**Sl:** Landslides

Figure 4.13. Geologic map of Spercheios river valley (after Stathopoulos et al., 2017)

Figure 4.14. Characteristic damages in the region of Lamia following Medicane Ianos: a) riverbank erosion and road embankment failure, b) extensive debris flow, c) bridge foundation scour, d) riverbank erosion, and e) road embankment failure

Expedition 1 - Elxis Group

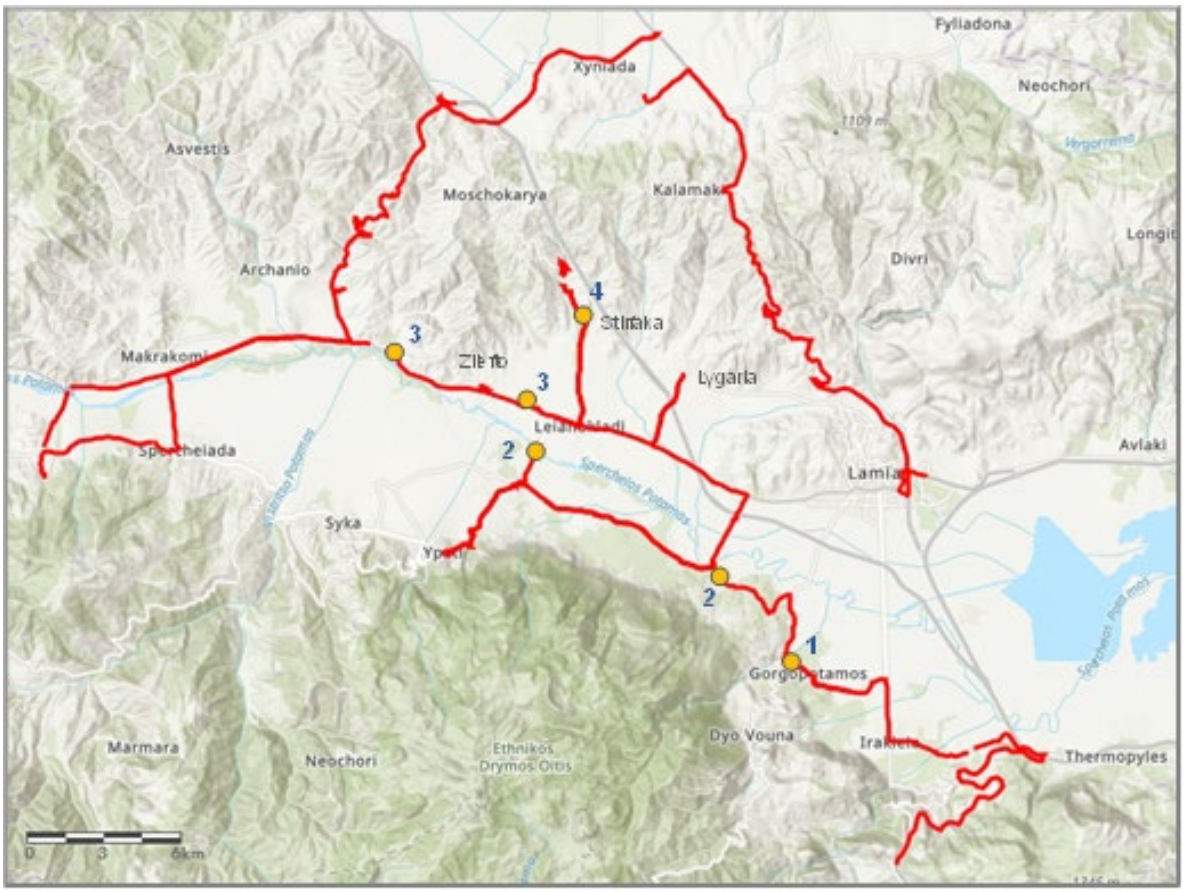

Figure 4.15. Area covered during Expedition 1 to the region of Lamia

Route:

- Hills of Bralos to the village of Gorgopotamos;
- From Gorgopotamos to the village of Ypati;
- From Leianokladi to Makrakomi;
- Makrakomi to the village of Xyniada, through Trilofo;
- Xyniada to Lamia, through the village of Agrilia.

Field Work Performed

1. Documentation of riverbank erosion and road failure at Gorgopotamos;
2. Reconnaissance along the south side of Spercheios river valley and the hillside of Oiti mountain;
3. Reconnaissance along E.O. Leianokladiou-Makryrachis;
4. Documentation of road failures along the north riverbank of Spercheios river

Expedition 2 - NTUA

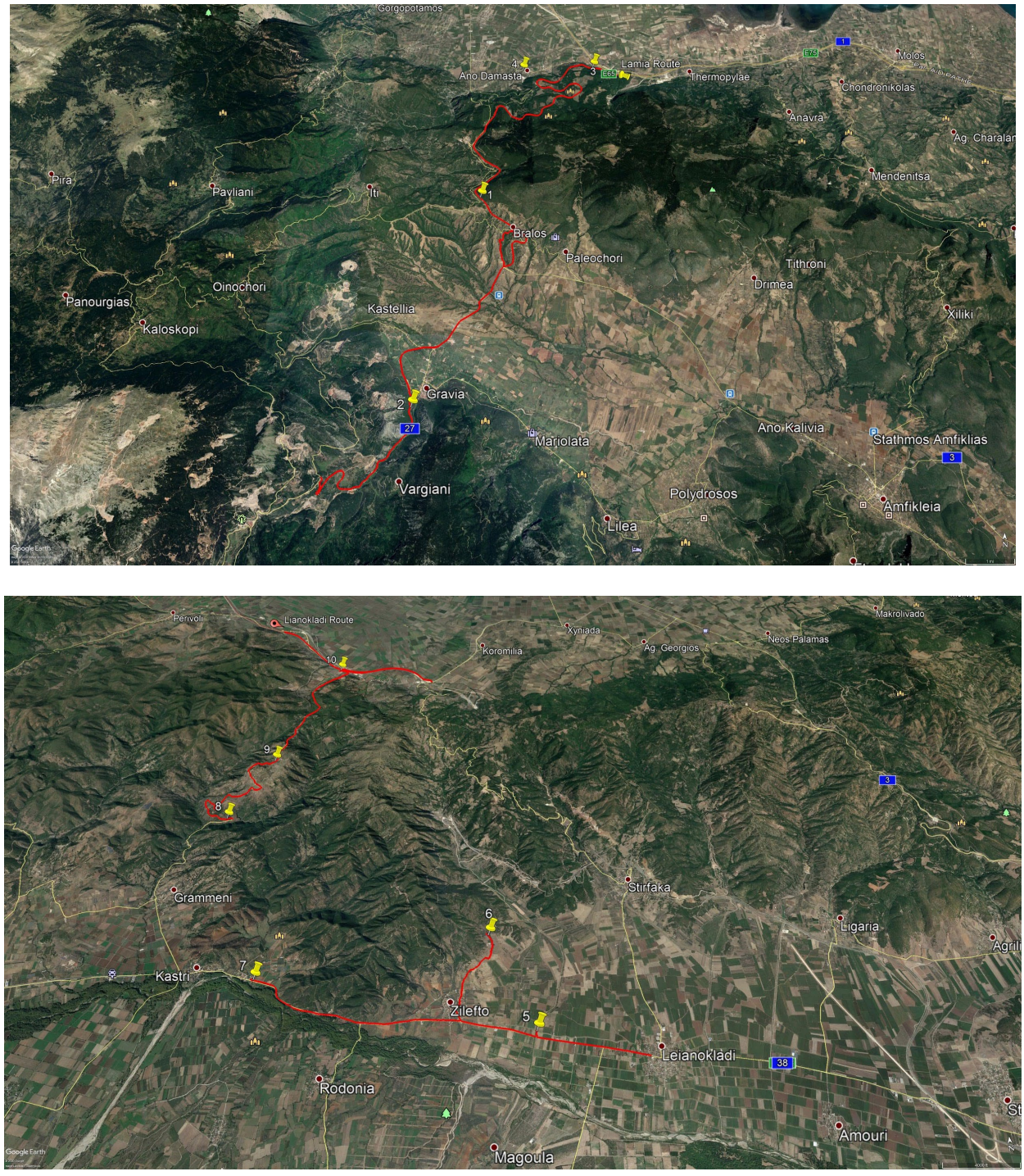

Figure 4.16. Areas covered during Expedition 2 to the region of Lamia: a) from Thermopylae to the village of Gravia, and b) from Lianokladi to the village of Perivoli

Route a:

- From the wider area of Thermopylae to the village of Bralos;
- From the village of Bralos to the village of Gravia;
- Southwest of the village of Gravia on the Amfissa-Bralos road and back.

Route b:

- From Lianokladi to the village of Kastri;
- From Kastri to the village of Trilofo;
- From Trilofo to the village of Ag. Stefanos;
- From Ag. Stefanos to the village of Perivoli.

Field Work Performed:

1. Documentation of surface erosion near the village of Bralos;
2. Documentation of rockfalls along the Amfissa-Bralos road near the village of Gravia;
3. Documentation of gully erosion near Thermopylae;
4. Reconnaissance of field flooding in the wider area of Ano Damasta;
5. Documentation of riverbank erosion, gully erosion and road failures in the region between Lianokladi, Zilefto and Kastri;
6. Documentation of landslide, surface erosion, rockfalls and road undercut between Trilofi, Ag. Stefanos and Perivoli.

4.4. Karditsa Region

4.4.1. Geology and Geomorphology

The main geological formations encountered in the wider area of Karditsa are the following (as presented in the geological map in Figure 4.17):

1. Alluvial deposits (Qc, Qf) encountered in Karditsa plain, consisting of cobbles, gravels, sands and clays. The deposits are loose at the upper layers and slightly to moderately dense in deeper layers. Their thickness is up to a few tenths of meters. It is mainly characterized by the presence of flysch formation.
2. Flysch formation (Fc) (central Greece unit) encountered west of Karditsa plain with a surface exposure along a NW-SE direction. The formation consists of alternations of sandstone, shales, siltstones and more seldom conglomerates. The formation is encountered totally weathered at the surface in many locations, forming a weathered mantle especially in places where the flysch is more clay rich.
3. Flysch formation (Fw) (western Greece unit) encountered west of Vraggiana. The formation consists of alternations of sandstone, marls, silty sandstones, thin bedded limestones and conglomerates. The thickness of this flysch formation reaches a total of 4500 m.
4. Transitional formation (K-Pc) from the Cretaceous limestones (Lc-C) to the flysch formation (Fc) consisting from alternations of limestones, sandstones, shales and marls. The formation is encountered west and northwest of Plastiras reservoir.
5. Thin-bedded Cretaceous limestones (LcC) with thin interlayers of cherts and locally shales, Triassic - Jurassic limestones (Lc-Tj) and flysch (Fc) are encountered as nappes in the area west and northwest of Plastiras reservoir.
6. Alternations of cherts, siltstones, shales, schists, thin bedded limestones and sandstones (sh) with intrusions of volcanic tuffs are encountered in the broad area south of Mouzaki.
7. Molassic formation (Mo-K) in the area around Kanalia consisting of conglomerates with layers of sandstones, siltstones and agglomerates at the base of the formation.

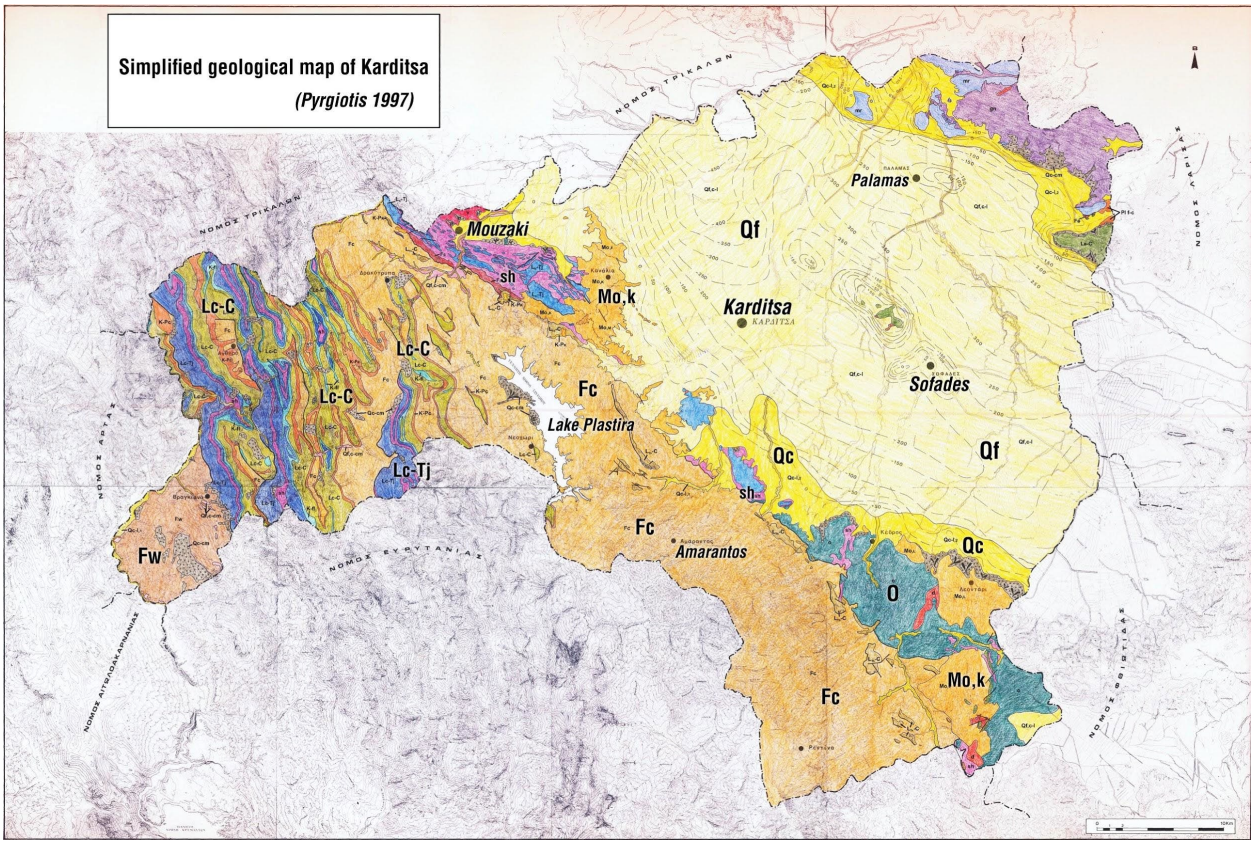

Figure 4.17. Geological map of Karditsa area (Pyrgiotis, 1997).

The geology of the most affected areas west of Karditsa are mainly characterized by the presence of flysch formations (Fc). The following flysch types are encountered in the area (according to the geological map of Pyrgiotis, 1997), as seen in Figure 4.18:

A. Shale flysch type: Shales alternating with thin and medium bedded sandstones
B. Mixed flysch type: Alternations of thin to medium (and occasionally thick) bedded sandstones with shales, either sandstone or shale dominates
C. Sandstone flysch type: medium or thick bedded sandstones with alternations of shales.
D. Conglomerate flysch type
E. Additionally, the weathering mantle is formed in most of these types. The mantle thickness is greater in the shale type and the mixed flysch type.

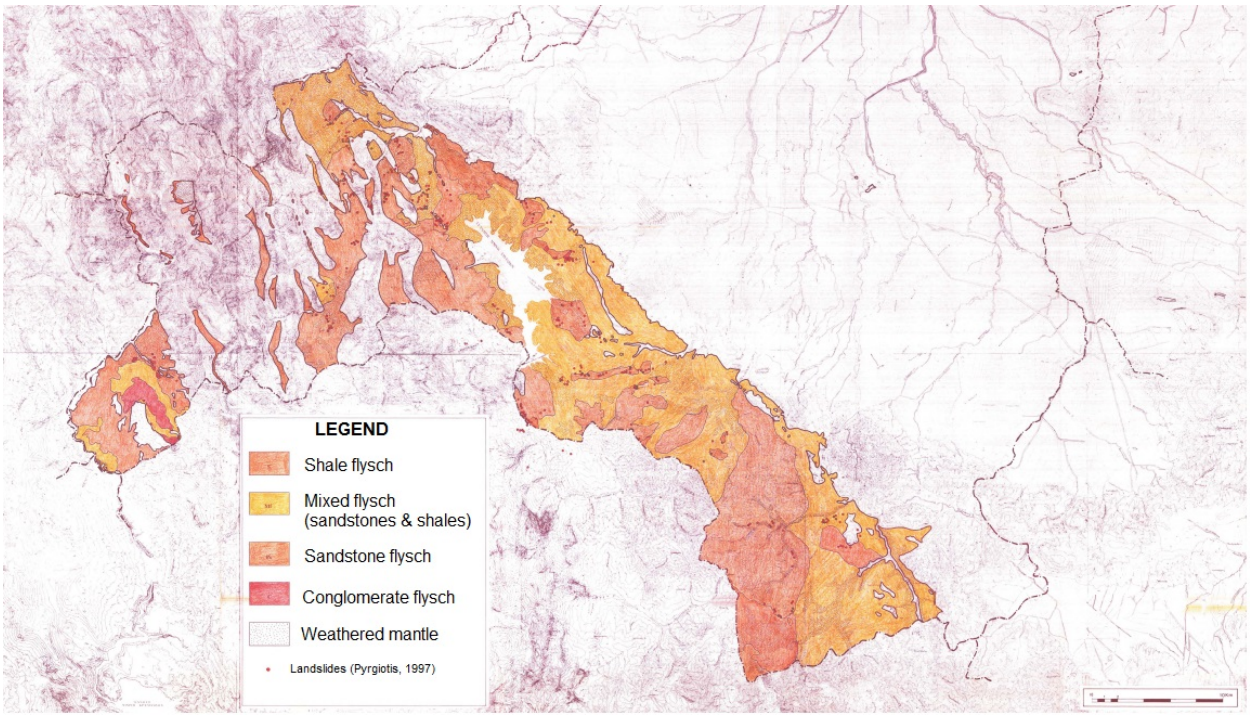

Figure 4.18. Geological map of flysch in study area (Pyrgiotis, 1997).

The following categories of slope failures are encountered in the different types of flysch (as presented later in the report):

1. Complex landslides: Translational - earth slides or earth flows in A and B type
2. Rotational slides (small to medium scale landslides) in A, D and E type
3. Earth flows in A and E type
4. Debris flows in D type but also in areas where fractured limestones outcrop at higher elevation
5. Rockfalls (& planar slides) in C flysch type and in limestones

4.4.2. Brief description of damage

The wider area of Karditsa has been heavily struck by secondary phenomena triggered by the Medicane Ianos. The induced structural damage could be preliminary separated into two general types based on the failure mechanism: slope failures and riverbank erosion-flooding phenomena.

The former type of failures is reported on the mountainous area of the Karditsa region, delineated by the village Argithea on the north, the village of Amarantos to the south and the village Vlassi at the western part of Lake Plastira. At this area, various types of slope failures i.e. landslides, rock falls, complex landslides, debris and earth flows were widespread causing severe damage to the manmade environment. Debris flows were most destructive, and in most cases damaged roads, bridges, and part of villages (i.e. Rafina).

Landslides classified as complex or rotational were mainly documented in areas geologically dominated by shale flysch and mixed type flysch, and where thick weathered mantle is mapped. They are characterized as relatively shallow failures and most of the time the landslide debris completely covered the road.

Considering the riverbank erosion-flooding phenomena, it is pointed out that the road network was heavily damaged in many places due to embankment failure and/or bridge collapse. The area that is delineated as the most impacted is the city of Mouzaki and the roads leading to the mountainous area i.e. Oxya and Pefkofito. In addition, large areas of the basin of Karditsa, including the town of Karditsa, were flooded.

4.4.3. Areas Covered during Reconnaissance

A three days (1-3 October) reconnaissance field survey conducted by teams at the affected region aiming to document the failures triggered by the Medicane Ianos. More specifically, geologists and engineers from universities (NTUA, and DUTh), individuals highly experienced in flooding, scouring and post disaster reconnaissance surveys, and young professionals worked as a team at the wider area of Karditsa.

As shown in Figure 4.19, George Papathanassiou and Sotiris Valkaniotis focused their survey on the western part of Lake Plastira mainly aiming to document landslides, rock falls, debris flows and the relevant damage to the man-made environment. The covered area included the villages of Nevropoli, Pezoula, Kalivia, Neochori, Belokomiti and Rafina. Also surveyed the flooded areas between Trikala and Karditsa. At the same period, two teams from NTUA, coordinated by Vassilis Marinos and Haris Saroglou conducted post reconnaissance surveys at the northern and southern part of Lake Plastira where large size slope failures were activated. The former team (Marinos, Karantanellis and Farmakis) investigated the failures along the road Mouzaki – Oxia - Argithea with specific interest in the zone of Argithea where large failures occurred. The latter team (Saroglou, Kallimogiannis, Makrinikas, Tsirogianni, Pavlopoulou) investigated the failures at the area Rachoula – Amarantos (southern part of Lake Plastiras) and along the roads Mouzaki - Pefkofito – Vlasi – Livadia – Petrilo and Mouzaki – Oxia - Argithea. The documentation of the flooding phenomena and the induced damages to the bridges at the basin of Karditsa was realized by Marianna Loli and Antonios E. Alvertos. All mobilized teams used a GPS unit for tracking their visited locations while UAV mapping technology applied in selected sites of interest.

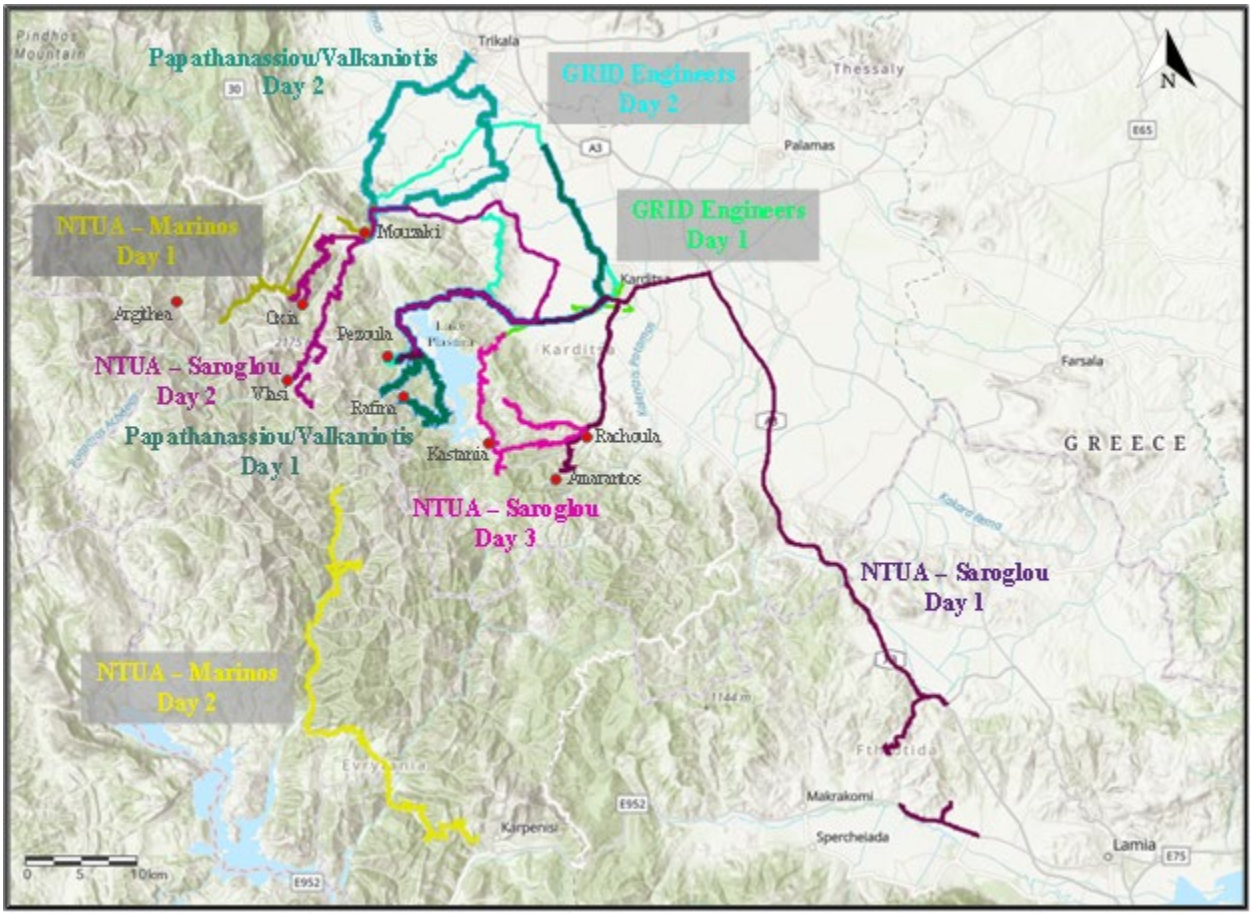

Figure 4.19. Reconnaissance routes of all deployment teams in the region of Karditsa.

Expedition 1 – Papathanassiou & Valkaniotis

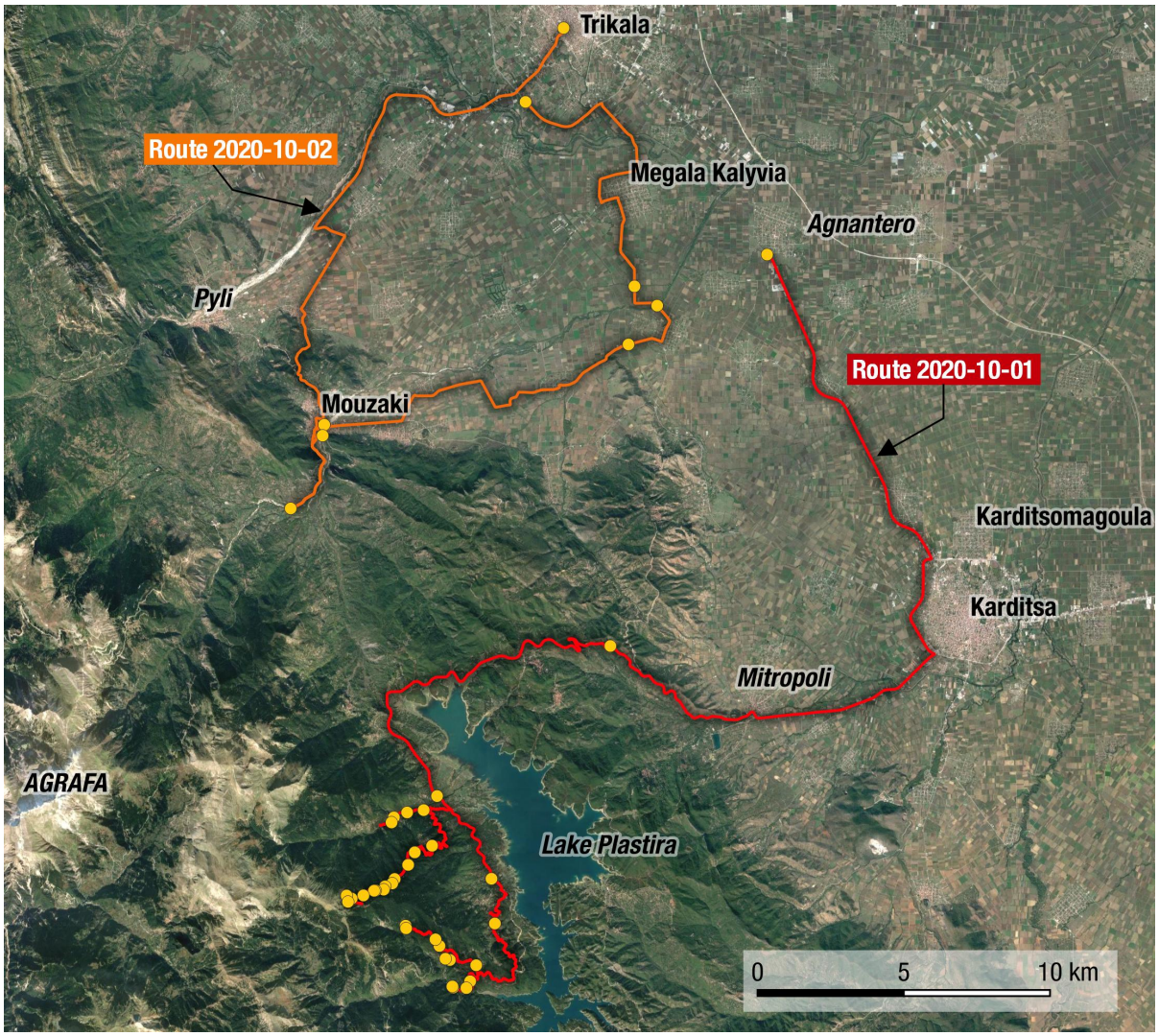

Figure 4.20. Areas covered during Expedition 1 to the region of Karditsa

Expedition 2 – NTUA - Marinos team

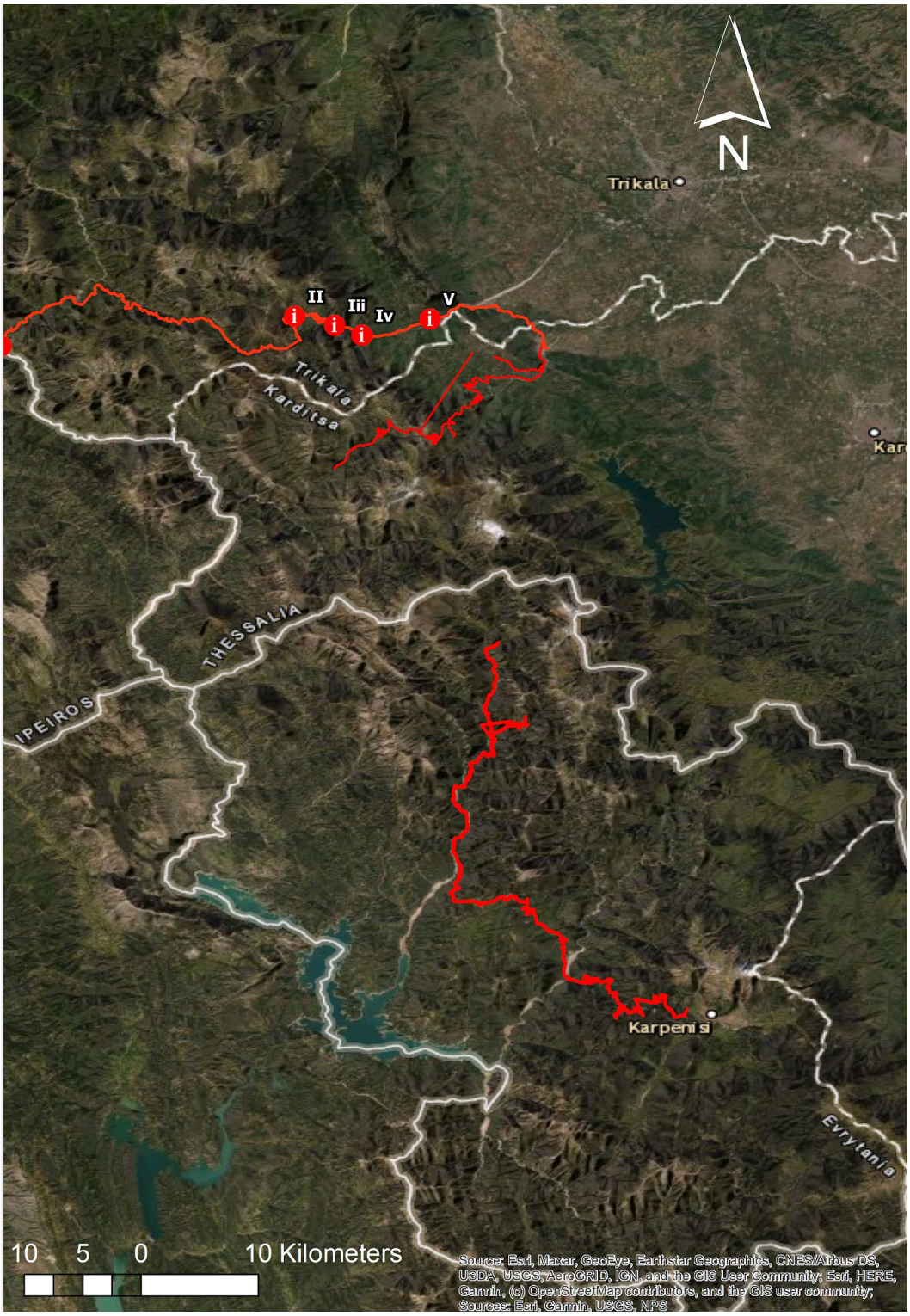

Figure 4.21. Areas covered during Expedition 2 to the region of Karditsa

Expedition 3 – NTUA - Saroglou team

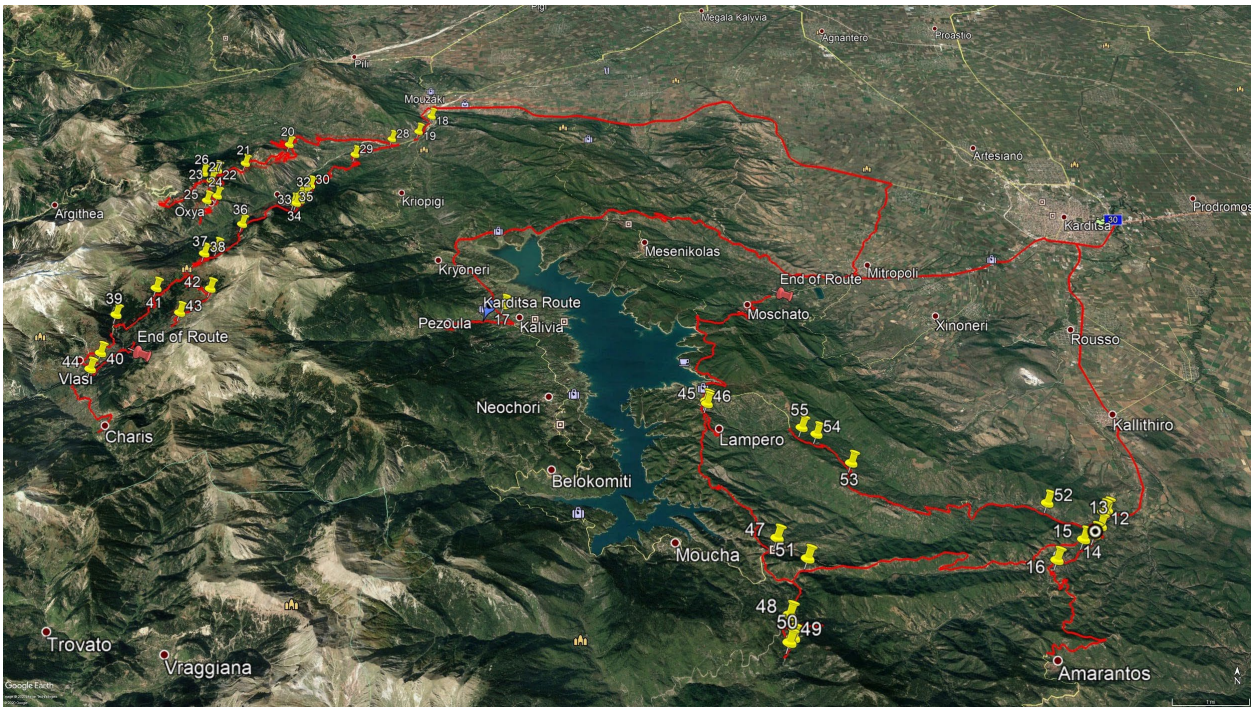

Figure 4.22. Areas covered during Expedition 3 to the region of Karditsa

Route a:

- From the city of Karditsa to the village of Rachoula;
- From Rachoula to the village of Amarantos;
- From Amarantos to the village of Pezoula through the city of Karditsa

Route b:

- From the village of Pezoula to the town of Mitropoli;
- From Mitropoli to the village of Mouzaki;
- From Mouzaki to the Nisia settlement;
- From Nisia to the villages of Platania and Paleochori;
- From Paleochori to the village of Oxya;
- From Oxya west to the Karditsa-Argithea road and back to Nisia settlement;
- From Nisia to the village of Vlasi;
- From Vlasi to the villages of Livadia and Petrilo.

Route c:

- From the town of Mitropoli to the village of Lampero;
- From Lampero to the village of Kastania;

- From Kastania to the village of Itamos;
- From Itamos to the village of Rachoula;
- From Rachoula to the village of Karafigio.

Field Work Performed:

1. Documentation of surface erosion, landslides and riverbank erosion in the area between Rachoula and Amarantos;
2. Documentation of surface and gully erosions, rockfalls, landslides, bridge scour and bridge failure in the route between Mouzaki and Oxya village;
3. Documentation of riverbank erosion, debris flows, landslides and road failures in the area between Nisia settlement and Vlasi;
4. Documentation of gully erosions, earth flows, landslides, retaining wall collapse and road failures in the route between Lampero, Kastania, Itamos, Rachoula and Katafigio.

4.5. Evritania Region

4.5.1. Geology and Geomorphology

The main geological formations encountered in the examined area, from Karpenissi towards Agrafa and Vraggiana, are the following (as presented in the geological map in Figure 4.23):

1. Bedded limestones ($K_{8-9}^{κ}$): Thin to medium bedded limestones with chert intercalations. The deposits are loose at the upper layers and slightly to moderately dense in deeper layers. Their thickness is up to a few tenths of meters. The formation is mainly characterized by the presence of flysch formation.
2. First flysch (K_{2-8}^{fl}): The formation consists of alternations of red pelitic layers and limestones. The heterogeneous nature of the formation is associated with favorable conditions for extensive anisotropic slides. In general, many slides are encountered in this formation, but none were met in the aftermath of Medicane Ianos.
3. Limestones (J_{13-K2}^{k}): The formation consists of alternations of sandstone, marls, silty sandstones, thin bedded limestones and conglomerates. The thickness of this flysch formation reaches a total of 4500 m.
4. Thin bedded alternations of cherts, siltstones and limestones (J_{6-12}^{hn})
5. Limestones (Ji.K): Series of thin bedded limestones with chert alterations

All the above formations are structured in a “belt” sequence due to successive thrusts with N-S direction (Figure 4.23). Even though the medicane hit this mountainous area, the extensive presence of the competent limestone beds supported and prohibited sliding phenomena. Rock falls and small rotational slides only occurred. Nonetheless, such phenomena are typical along this road network during any intense rainfall.

4.5.2. Brief description of damage

The Evritania prefecture territory has been moderately damaged by Ianos Medicane. Sparse landslide phenomena are observed. The failures are observed to have occurred within the flysch formations causing slight to moderate damage to the mountainous local road network. Landslide and rockfall phenomena are controlled by the limestone-siltstone heterogeneity, the tectonic disturbance and the regional setting. Planar and wedge slides mainly occurred in the studied area. The controlling factors are the potential kinematic favorable conditions and shear strength of discontinuities (soft pelitic interbedded layers). New rotational landslides were not identified.

The wider area of Agrafa is observed to have been most affected with evidence of temporary road closure at certain locations. However, Vragianna village was still inaccessible (from Agrafa) during the time of reconnaissance due to bridge damage by boulder-sized debris flow.

Furthermore, minor to no evidence of damage by Ianos Medicane is found within the wider Karpenisi area.

4.5.3. Areas Covered during Reconnaissance

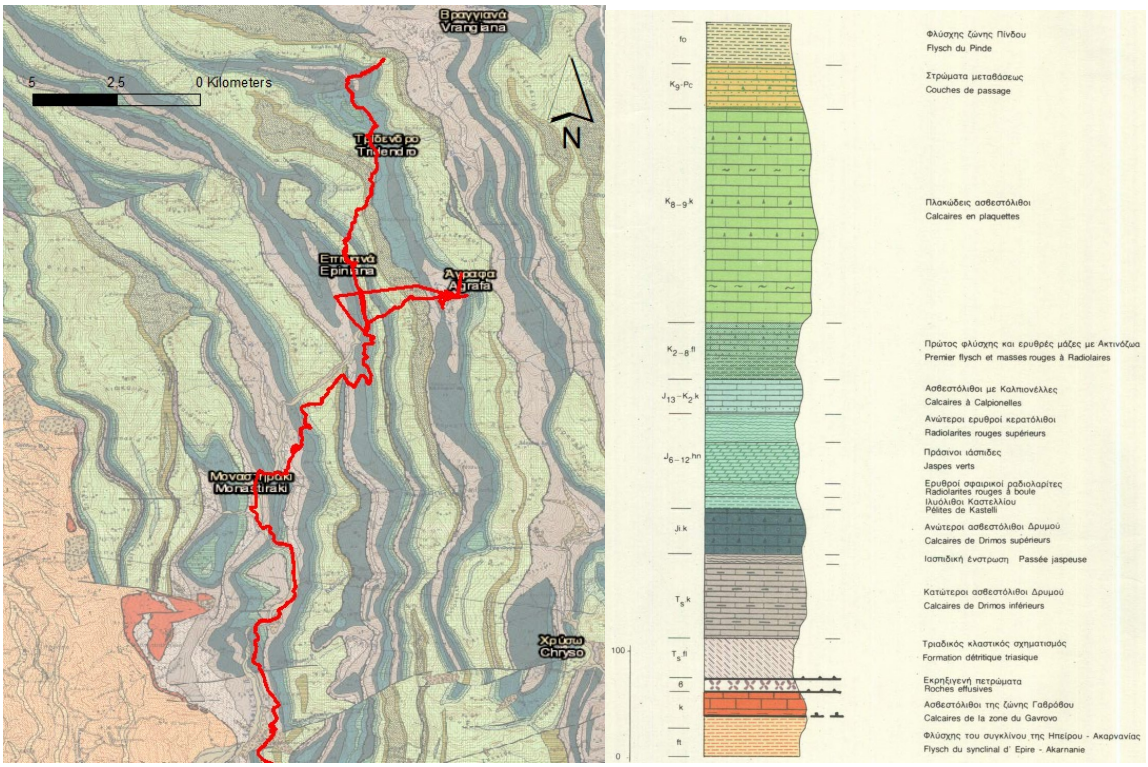

Figure 4.23. Evritania region geological map and reconnaissance route from Karpenisi to Vraggiana and Agrafa.

4.6. Flooding in Western Thessaly region

4.6.1. Introduction - Geomorphology - Flood History

Western Thessaly plain is a large alluvial plain in central Greece, mainly in the administrative regions of Trikala and Karditsa, and to a lesser extent by parts of Larisa and Fthiotida (Lamia) regions. Western Thessaly sub-basin is part of Pinios hydrologic basin. The largest rivers crossing western Thessaly basin is Pinios river in the northern part, and Enipeas river in the eastern part. Other significant rivers are Litheos, Portaikos, Pamisos, Kalentzis, Sofaditis, Farsaliotis and Megalo Rema (a former swamp/lake area that was drained). The major watersheds contributing into the west Thessaly plain are shown in Figure 4.24.

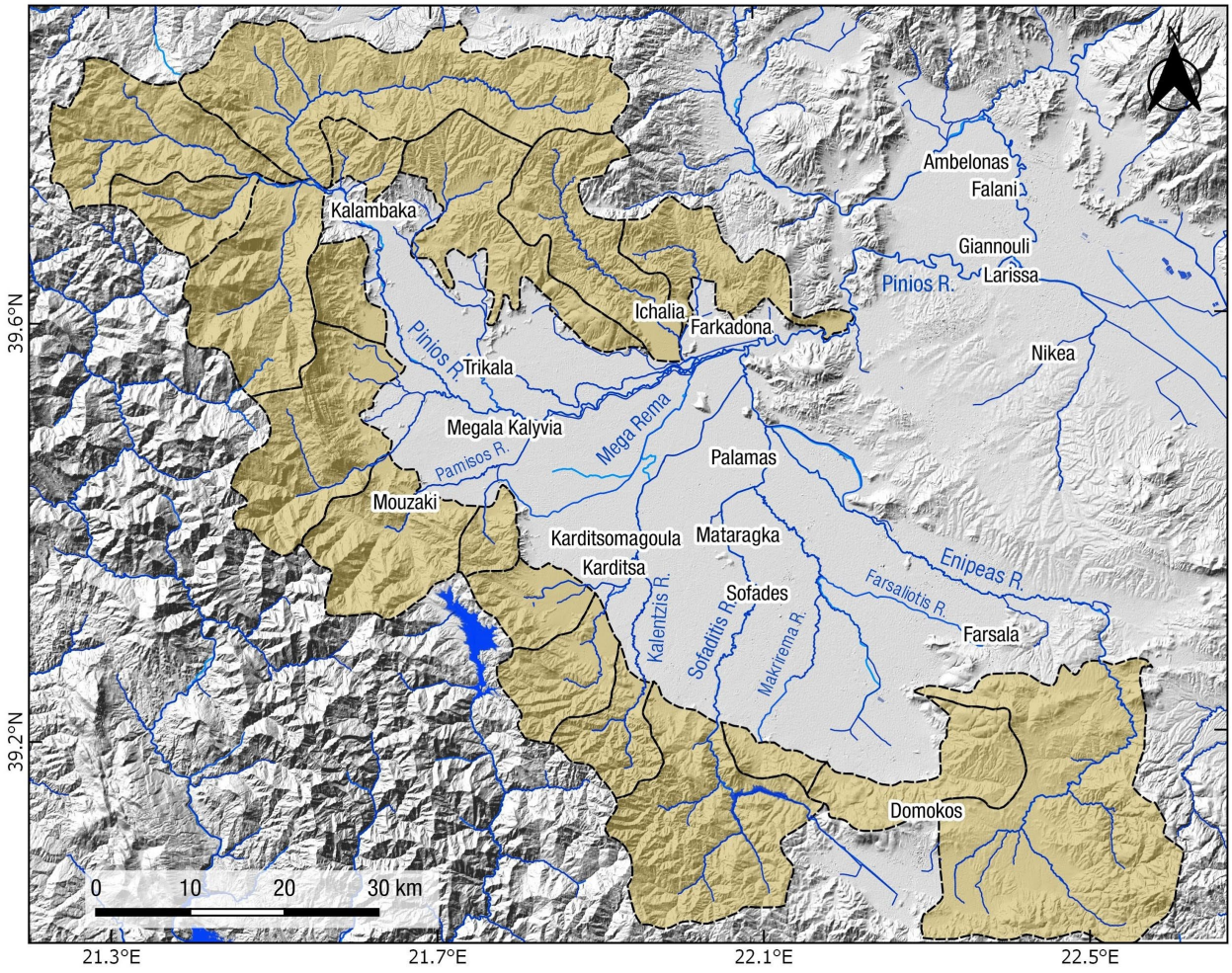

Figure 4.24. Major mountainous basins (light brown colour) contributing into the west Thessaly plain and Pinios river basin.

Pinios river and its tributaries are collecting surface water by large watersheds of Pindos mountain range to the west, and Othris mountain to the south. Extensive and damaging flooding is quite

frequent in the western Thessaly plain. The areas most susceptible to flooding are the narrow Pinios gorge area between Trikala and Larisa (Piniada valley), the central part of the basin between Trikala and Karditsa, and the eastern part (Enipeas, Farsaliotis).

Table 4.1. Significant recent flood events in western Thessaly.

1979-11-19	2004-07-28
1987-03-23	2010-09-11
1990-08-24	2015-02-01
1994-10-22	2016-11-12
2003-01-24	

Using available satellite imagery, we demonstrate in subsequent figures (Figures 4.25-4.28) an overview of four of the flooding events listed in Table 4.1. We used Landsat 5TM and Landsat 7ETM+ optical satellite imagery acquired shortly after flooding. Landsat raw imagery data were acquired from USGS, while some frames that were missing from the USGS archive were acquired from European Space Agency Landsat archive.

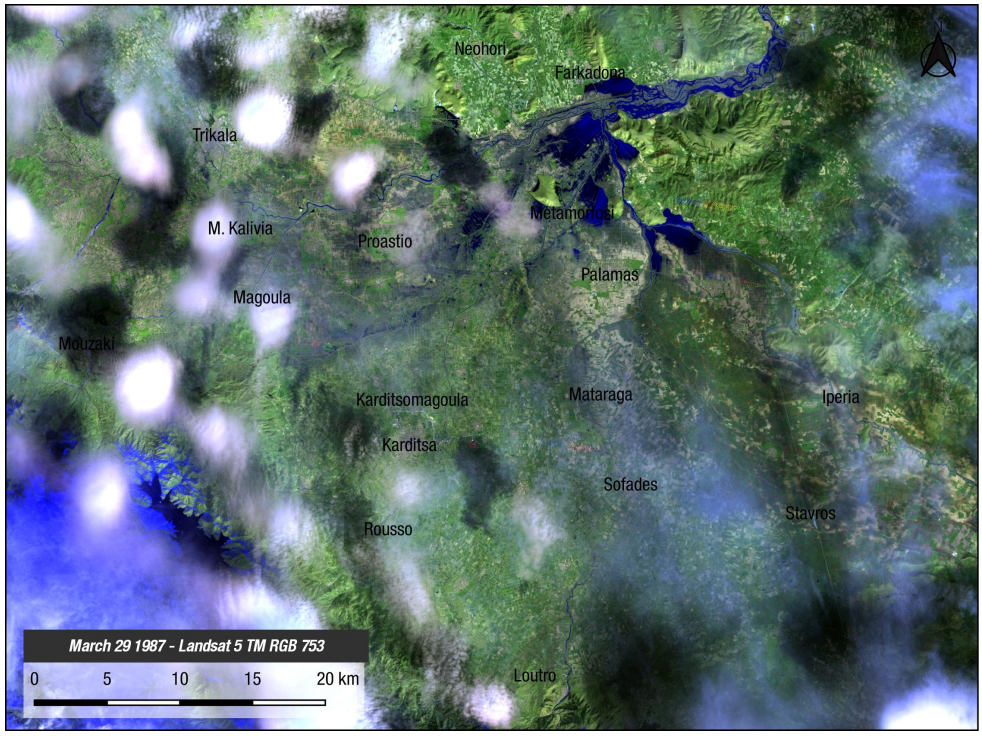

Figure 4.25. Flooded areas (blue colors) in western Thessaly from the 3-1987 flood event, as visualized by Landsat 5TM satellite imagery. Landsat 5TM pseudo-color composite (Bands 7-5-3), acquired in March 29 1987.

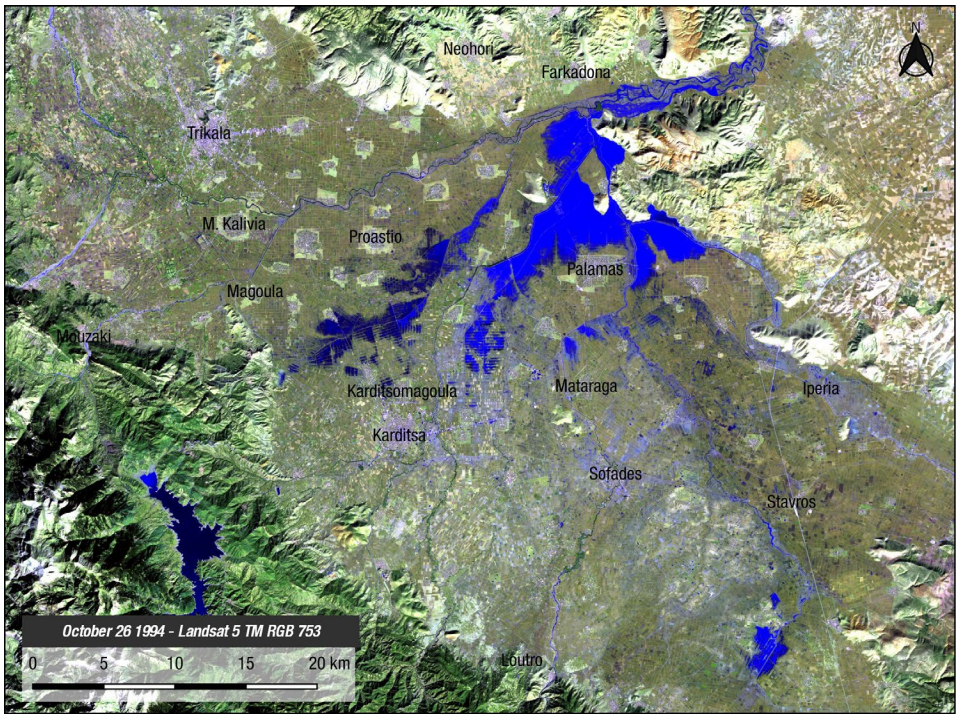

Figure 4.26. Flooded areas (blue colors) in western Thessaly from the 10-1994 flood event, as visualized by Landsat 5TM satellite imagery. Landsat 5TM pseudo-color composite (Bands 7-5-3), acquired on October 26 1994.

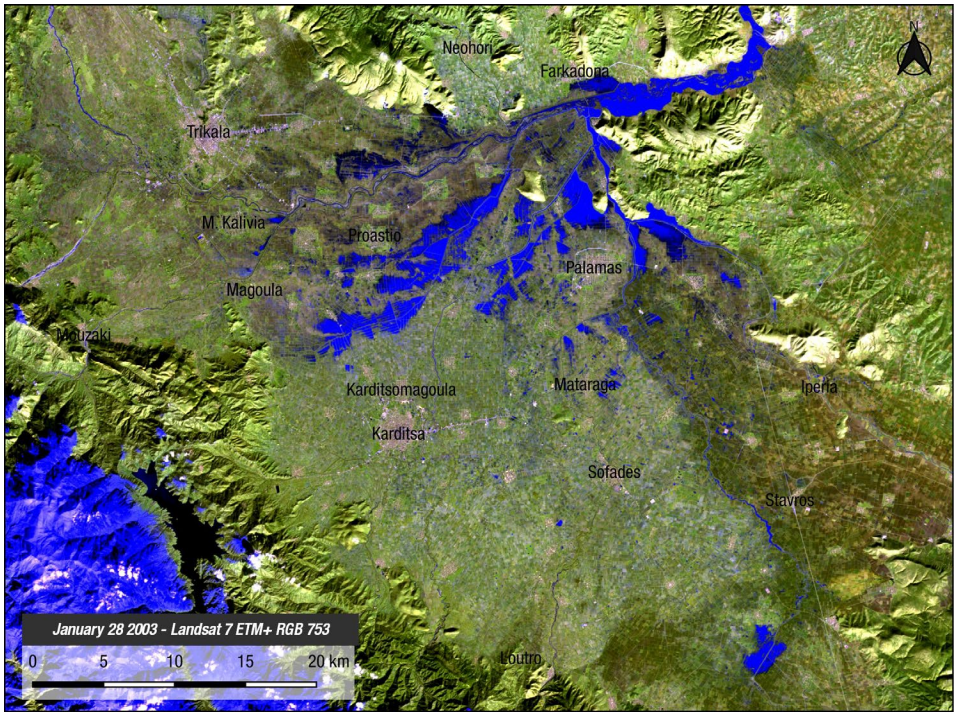

Figure 4.27. Flooded areas (blue colors) in western Thessaly from the 1-2003 flood event, as visualized by Landsat 7 ETM+ satellite imagery. Landsat 7 ETM+ pseudo-color composite (Bands 7-5-3), acquired on January 28 2003.

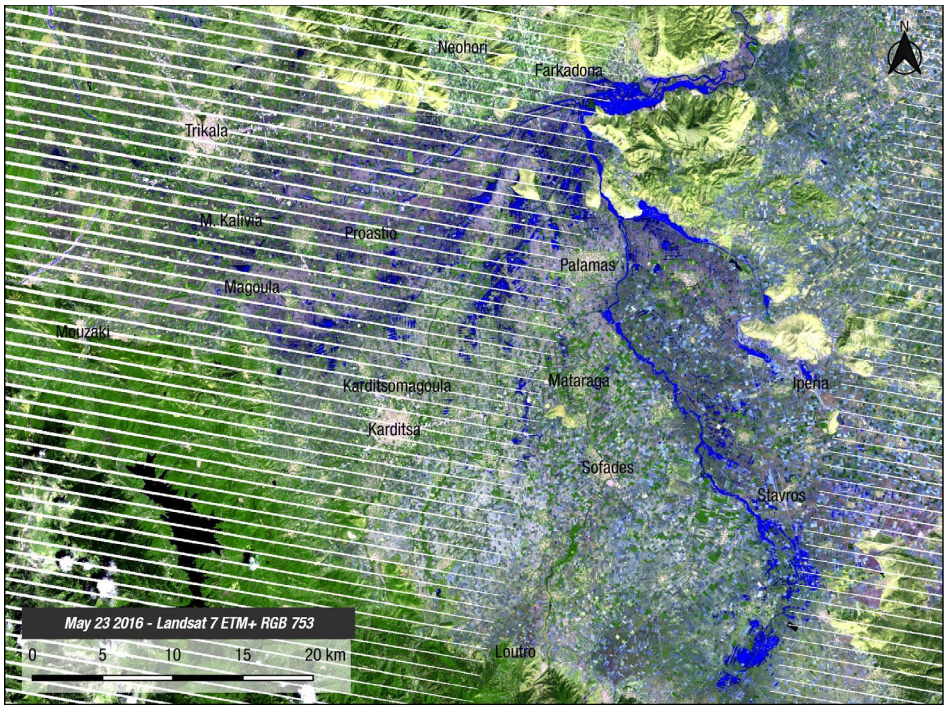

Figure 4.28. Flooded areas (blue colors) in western Thessaly from the 5-2016 flood event, as visualized by Landsat 7 ETM+ satellite imagery. Landsat 7 ETM+ pseudo-color composite (Bands 7-5-3), acquired on May 23 2016. Diagonal stripes are missing data due to Scan Line Corrector instrument failure.

4.6.2. Flood mapping using satellite imagery

In order to accurately map the extent of flooding over western Thessaly, we used optical multispectral satellite imagery (Copernicus Sentinel-2 with a resolution of 10-20 meters) and radar satellite imagery (Copernicus Sentinel-1 with a resolution of 5x20 meters) as shown in Figure 4.29. The use of standard indices (NDWI, NDMI etc) in Sentinel-2 imagery was found to be not optimal, as it underestimated the inundated areas. We used a combined methodology; first a series of short-wave infrared band combinations (12-11-4 & 12-8A-4) were created that visualize inundated areas with dark/blue colors. We classified the images using these colors at the low elevation areas. Radar imagery (Sentinel-1) has the advantage of cloud canopy penetration, and thus, scans can be acquired regardless of weather conditions. For Sentinel-1 SAR imagery, we used the COIN service in Geohazards TEP (https://geohazards-tep.eu/) that calculates coherence and intensity changes from an interferometric pair of Sentinel-1. The extracted inundated area from Sentinel-1 had some differences from the one extracted from Sentinel-2; total area extent was smaller, as radar imagery changes were less sensitive in very shallow water presence, and also optical Sentinel-2 can identify subtle changes in reflectance in areas that were flooded recently, but there was very little or no water present at the time of acquisition. The temporal difference between Sentinel-1 & 2 acquisitions also affects the result, as flood water retreated or propagated in some areas. Resulting areas were merged, and remaining areas are manually traced by photo interpretation.

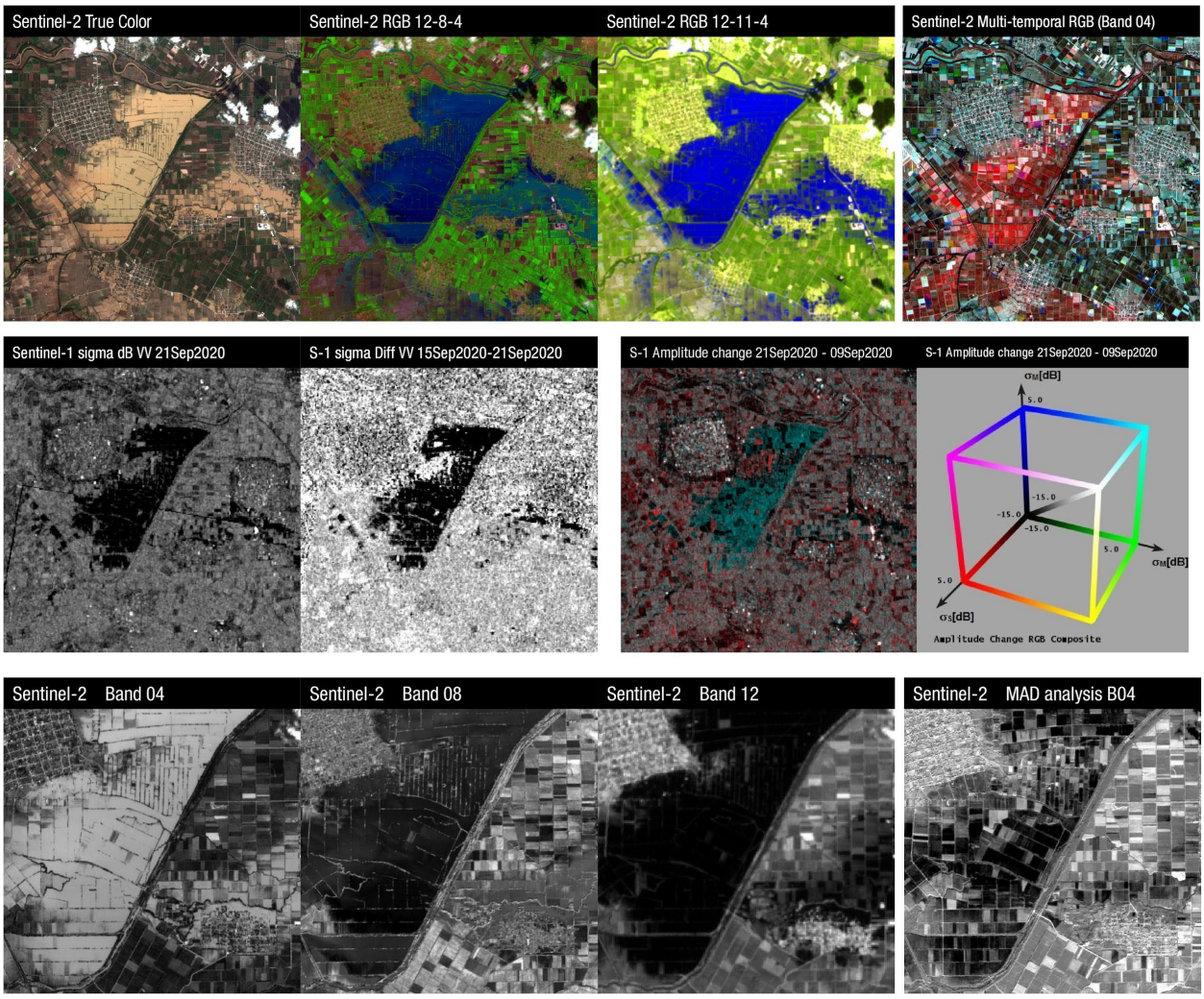

Figure 4.29. Various satellite data and analysis products used for west Thessaly flood mapping.

4.6.3. Results - Comparison with Flood Hazard Maps

Results are shown in Figure 4.30. Total area that was flooded or overrun by flood waters is calculated as 475,5 km^2. Area measured includes western Thessaly plain, Pinios gorge between Trikala and Larisa, and Xiniada plain to the south.

The total extent of the flooded areas in western Thessaly did not exceed the one estimated by the Flood Hazard Management Plan of Thessaly district (FHMP 2018). In Figure 4.31 we show a comparison between the Ianos flood extent and the scenario maps for flooding with return period of T = 50, 100 and 1000 years.

Figure 4.32 to 4.36 show interpretations of flooded regions in selected areas.

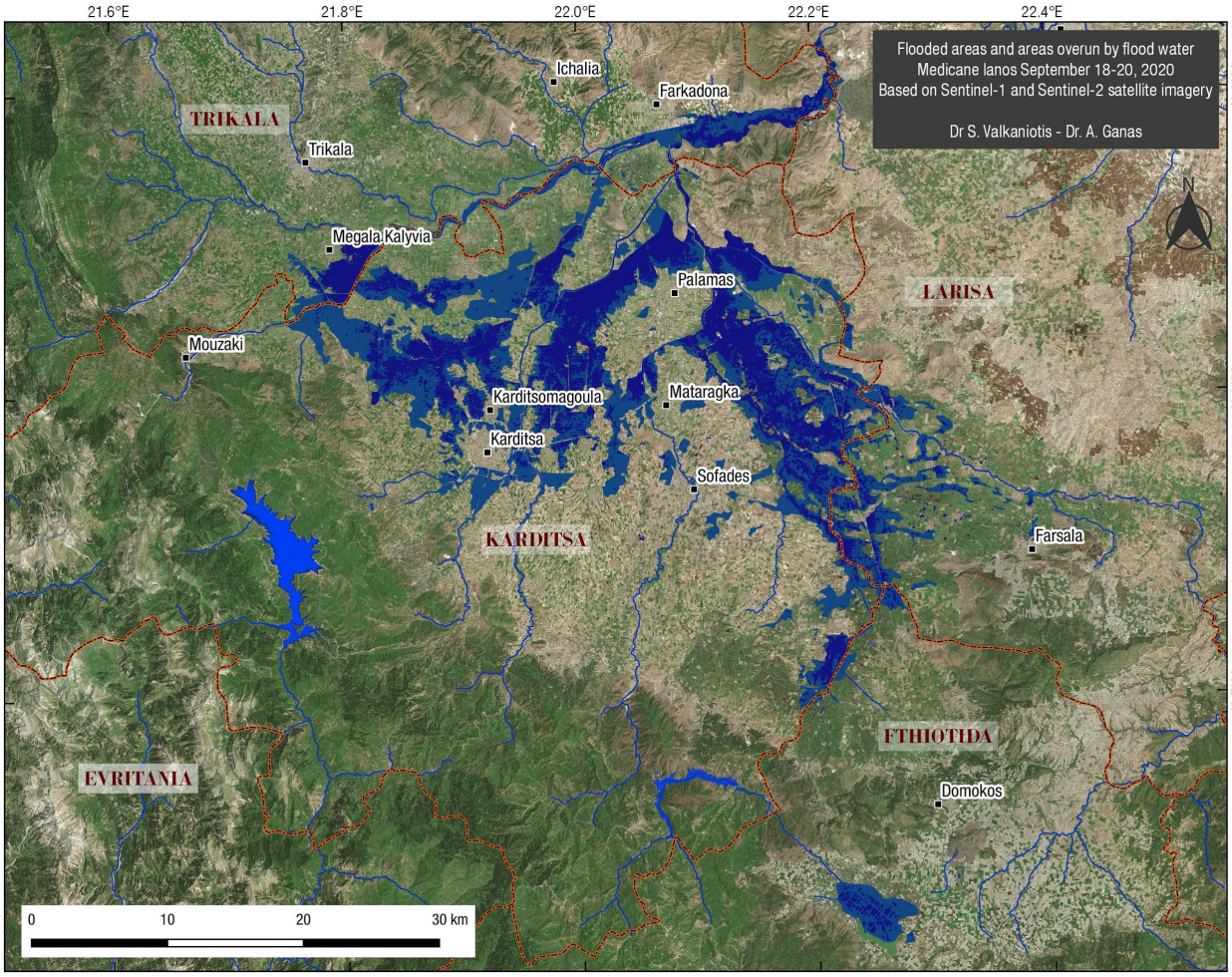

Figure 4.30. Flooded areas and areas overrun by flood waters, mapped using Copernicus Sentinel-1 and Sentinel-2 satellite imagery. Dark blue are water inundated areas, while cyan colors mark areas that did not retain significant water but were overrun by flood waters during the flood event. Total area is 475,5 km^2.

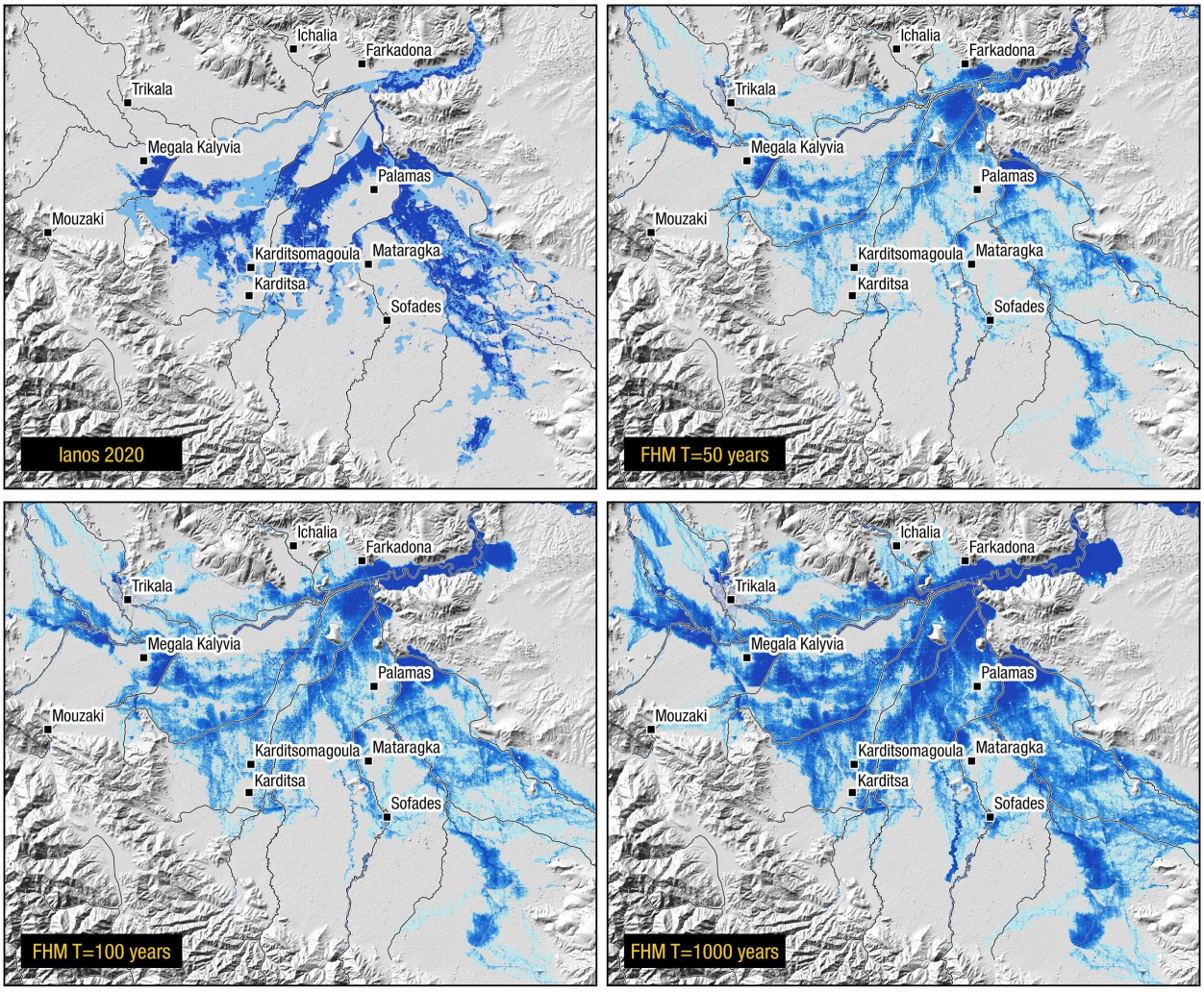

Figure 4.31. Comparison of the 2020 Medicane Ianos flooded areas mapping (upper left) with the Flood Hazard Maps for return periods of T=50/100/1000 years (FHMP 2018).

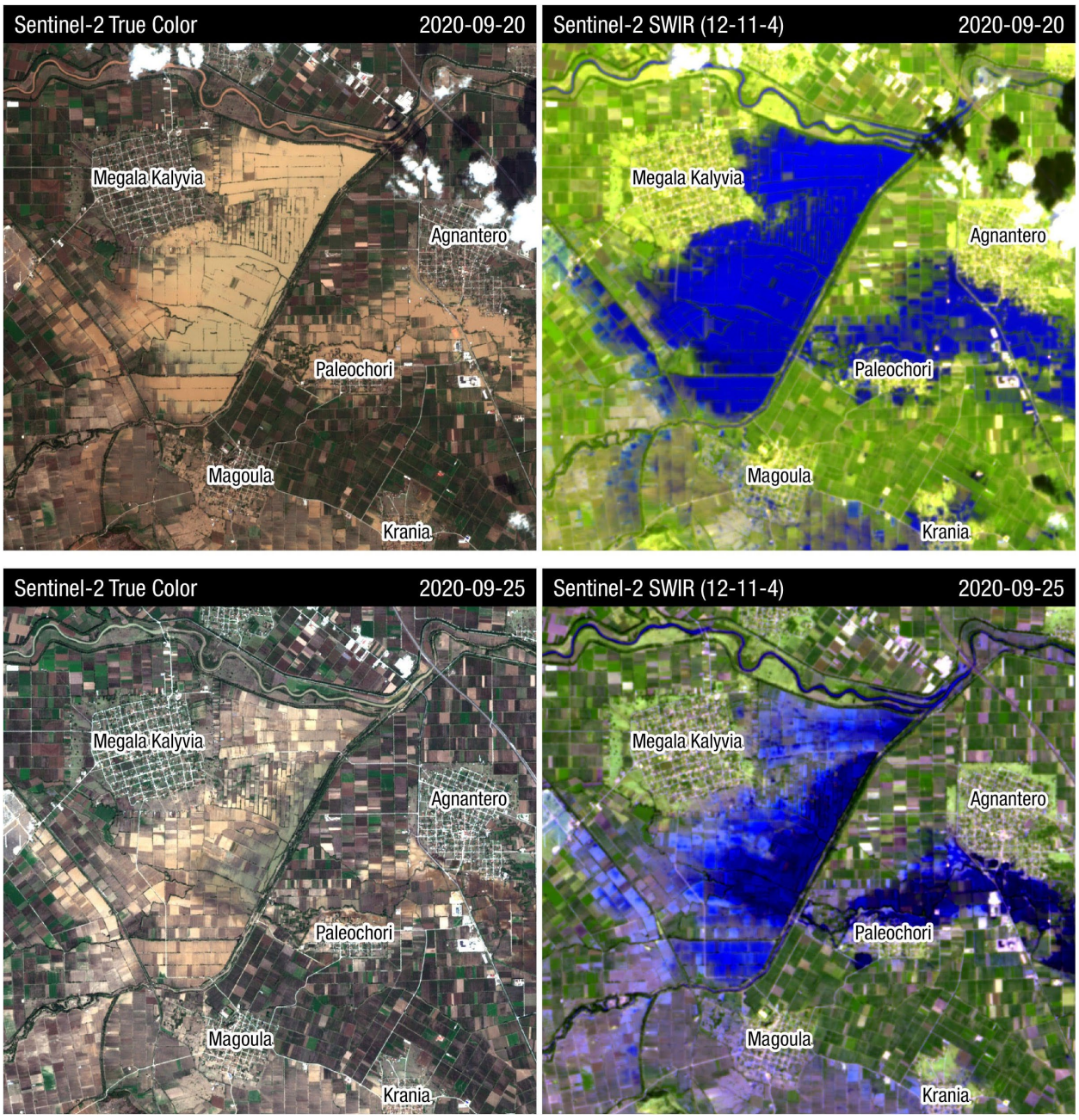

Figure 4.32. Flooded areas between Trikala and Karditsa. Top: Sentinel-2 image (True color and Short-wave infrared composite) on September 20, 2020. Bottom; Sentinel-2 image (True color and Short-wave infrared composite) on September 25, 2020.

Figure 4.33. Flooded areas from Enipeas and Farsaliotis rivers. Top: Sentinel-2 image (True color and Short-wave infrared composite) on September 20, 2020. Bottom; Sentinel-2 image (True color and Short-wave infrared composite) on September 25, 2020. Accumulation of water east of Palamas occurred in the days following the flood event, as water moved downstream.

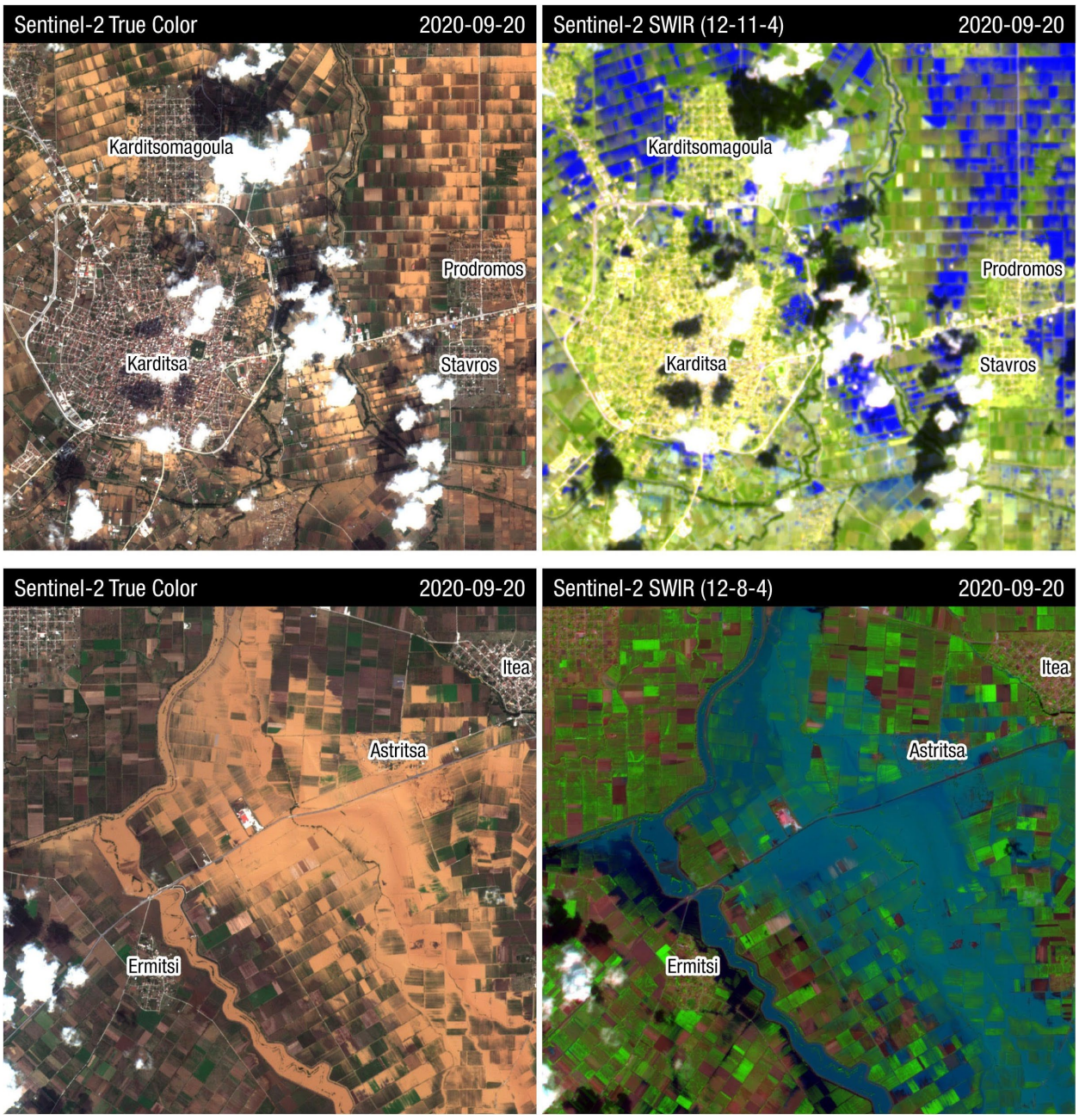

Figure 4.34. Flooded areas from Enipeas and Sofaditis rivers. Top: Karditsa area. Bottom; Itea area (Sofaditis river). Sentinel-2 image (True color and Short-wave infrared composite) on September 20, 2020.

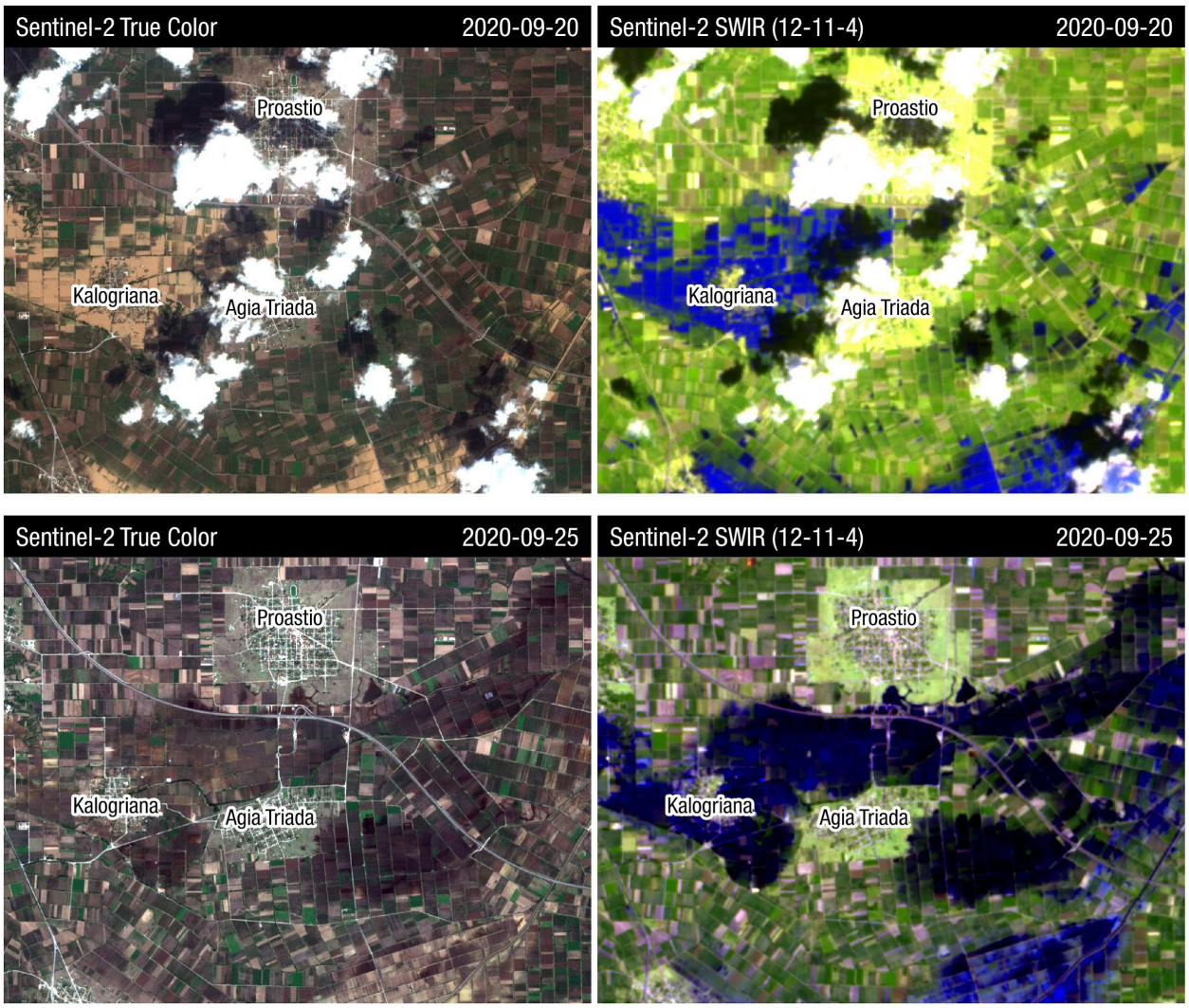

Figure 4.35. Flooded areas in Kalogriana/Agia Triada, Karditsa. Top: Sentinel-2 image (True color and Short-wave infrared composite) on September 20, 2020. Bottom; Sentinel-2 image (True color and Short-wave infrared composite) on September 25, 2020. Accumulation of water east of Kalogriana occurred in the days following the flood event.

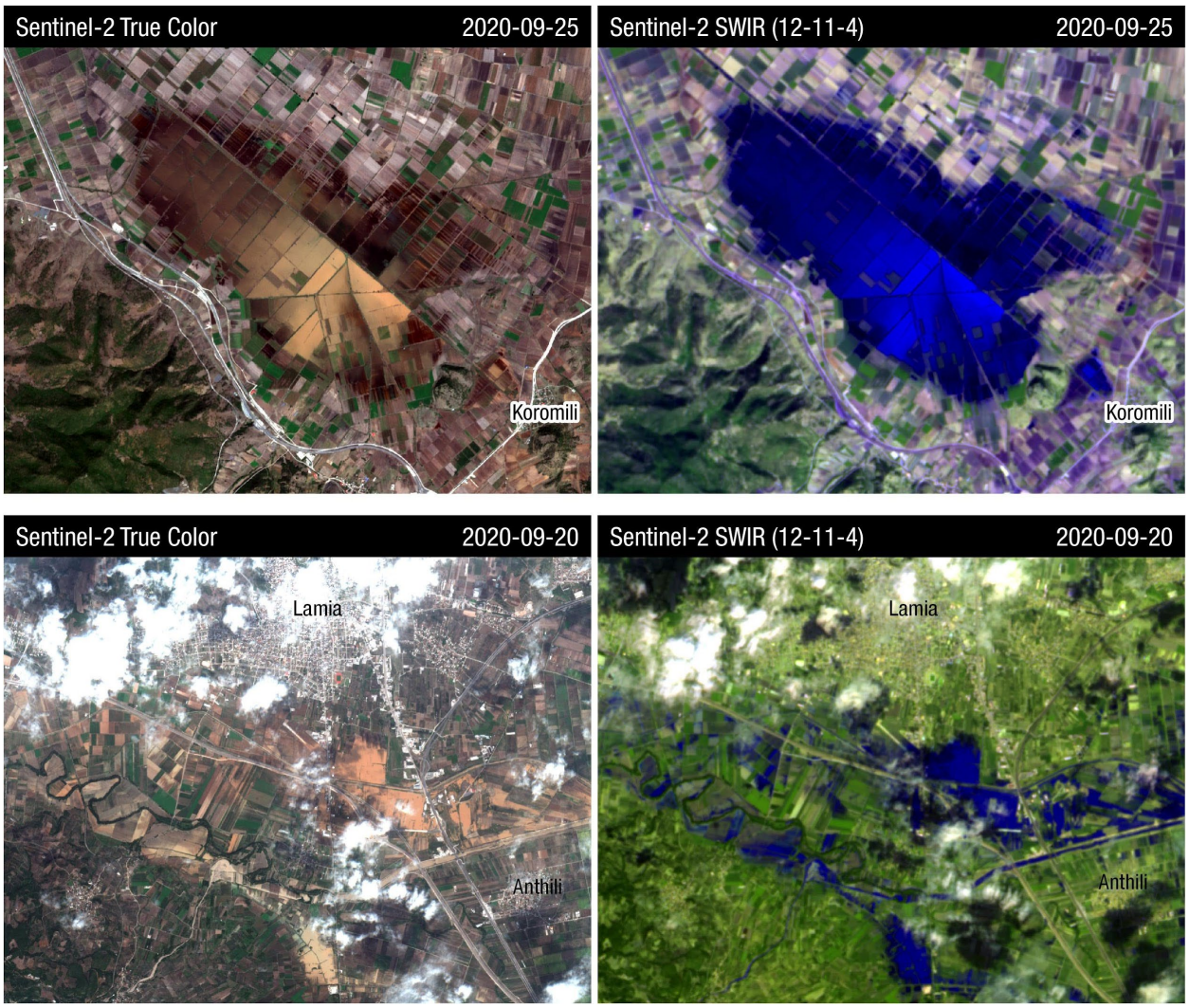

Figure 4.36. Top: Sentinel-2 image (True colour and Short-wave infrared composite) of Xiniada valley (Fthiotida) on September 25, 2020. Bottom; Sentinel-2 image (True colour and Short-wave infrared composite) of Spercheios valley and Lamia on September 20, 2020.

5. Transportation Systems

5.1. Bridges

5.1.1. Cephalonia Island

Bridges in Cephalonia island performed generally adequately during Medicane Ianos. Nonetheless, a critical, simple-supported, multi-span, reinforced concrete bridge founded on steep topography and connecting the village of Agkonas with Myrtos beach and Erissos peninsula (point 4 in Figure 4.11), collapsed, impacting the transportation network of the island (Figure 5.1). The structure, better known to the islanders as the "Chimoniko" bridge, was characterized by a width of ~9 m and a length of ~30 m, and was simply supported on two piers with a height of approximately 10 m (east pier) and 13 m (west pier), respectively. The span length was ~10 m, and the piers were founded on shallow footings on a limestone formation.

During the post-event reconnaissance, on 10/01/2020, detailed UAV-enabled mapping was conducted to better understand the failure mechanism. Orthophotos and DSM were produced (Figures 5.2 and 5.3), based on which an initial assessment can be made. A visualization of the 3D model of the failed "Chimoniko" bridge can be seen here: https://skfb.ly/6WyYT. The prevalent failure mode appears to be the scour of the west pier foundation from extensive gully flooding and debris. Such mechanism is consistent with the translational downstream movement of the foundation body, the pier, and the deck beams (Figure 5.2). Moreover, the failure mode is also supported by the observation that the older (built in 1943), masonry, single-span bridge just upstream of the collapsed structure, did not show any signs of damage. Contrary to the "Chimoniko" bridge, the older bridge was supported on masonry abutments on both sides of the gully. It can be presumed that the new bridge had a significantly reduced flow capacity, due to the presence of the piers. Particularly the west pier was comparatively more vulnerable since it was located more centrally within the flood/debris flow path. (Figure 5.3).

5.1.2. Lamia Region

In Lamia/Pthiotida and the surrounding areas, no significant damages were reported on bridge infrastructure following Medicane Ianos. Accordingly, the reconnaissance deployments in the area (ElxisGroup on 9/25/2020 and NTUA - Saroglou team on 10/01/2020), did not record any extensive damage. The single finding consists of the widespread scour of the foundation embankment of the railway bridge just north of Stirfaka village (point 4 in Figure 4.15). Figure 5.4a shows the eroded scar of the foundation embankment of the west piers, while Figure 5.4b illustrates the exposed foundation (pile cap) of one of the piers. Debris were present on site, the size of which often exceeded 30 cm (Figure 5.4d). It is worthwhile to note that the east abutment of the bridge appeared to be unaffected (Figure 5.4c).

Figure 5.1. Collapsed multi-span RC bridge on E.O. Argostoliou-Fiskardou (38.319506°N, 20.508197°E): a-d) roadside photos, e) UAV-enabled 3D texture mesh - perspective view (view 3D model at: https://skfb.ly/6WyYT)

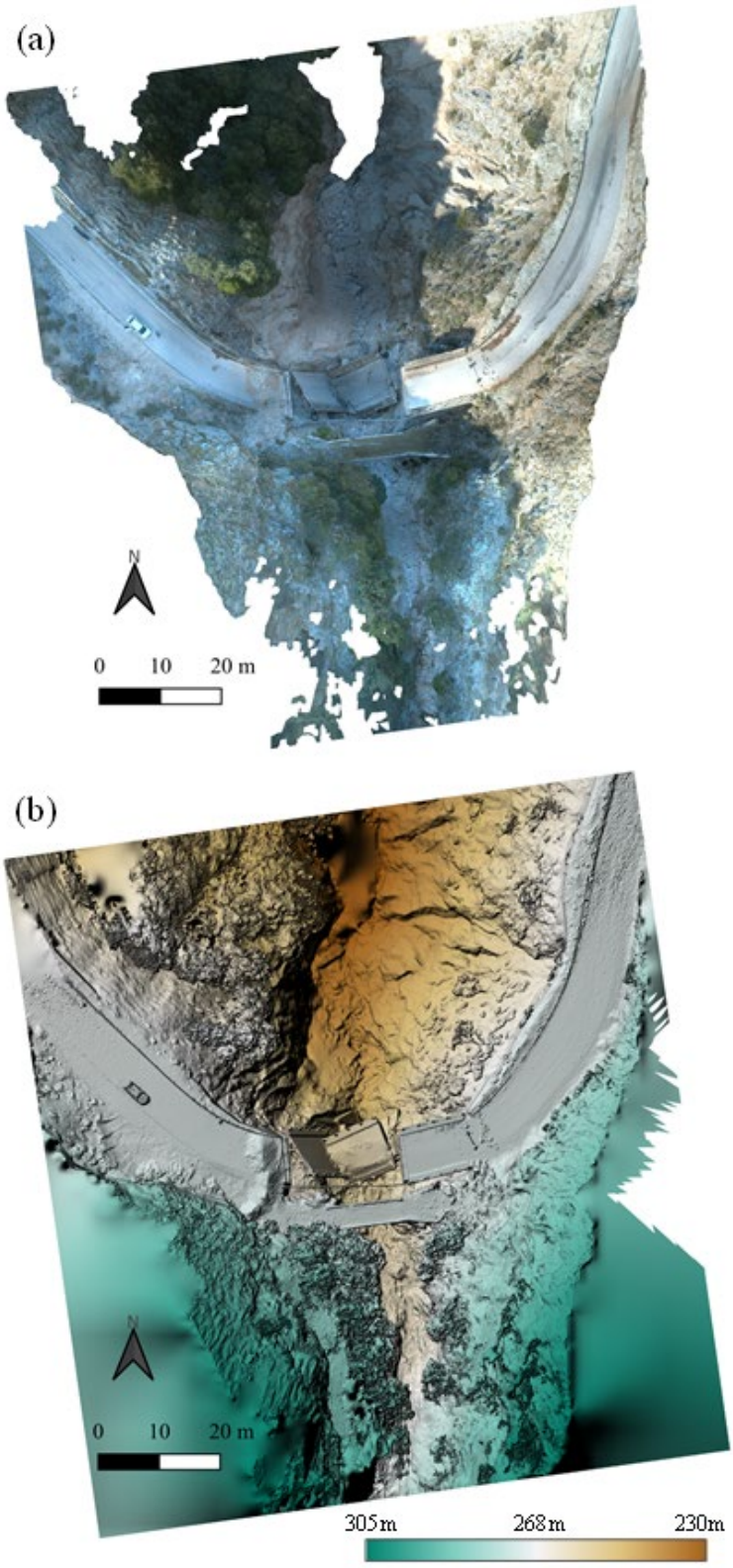

Figure 5.2. UAV-enabled mapping of collapsed bridge on E.O. Argostoliou-Fiskardou (38.319506°N, 20.508197°E): a) top-view Orthophoto, and b) top-view DSM (view 3D model at: https://skfb.ly/6WyYT)

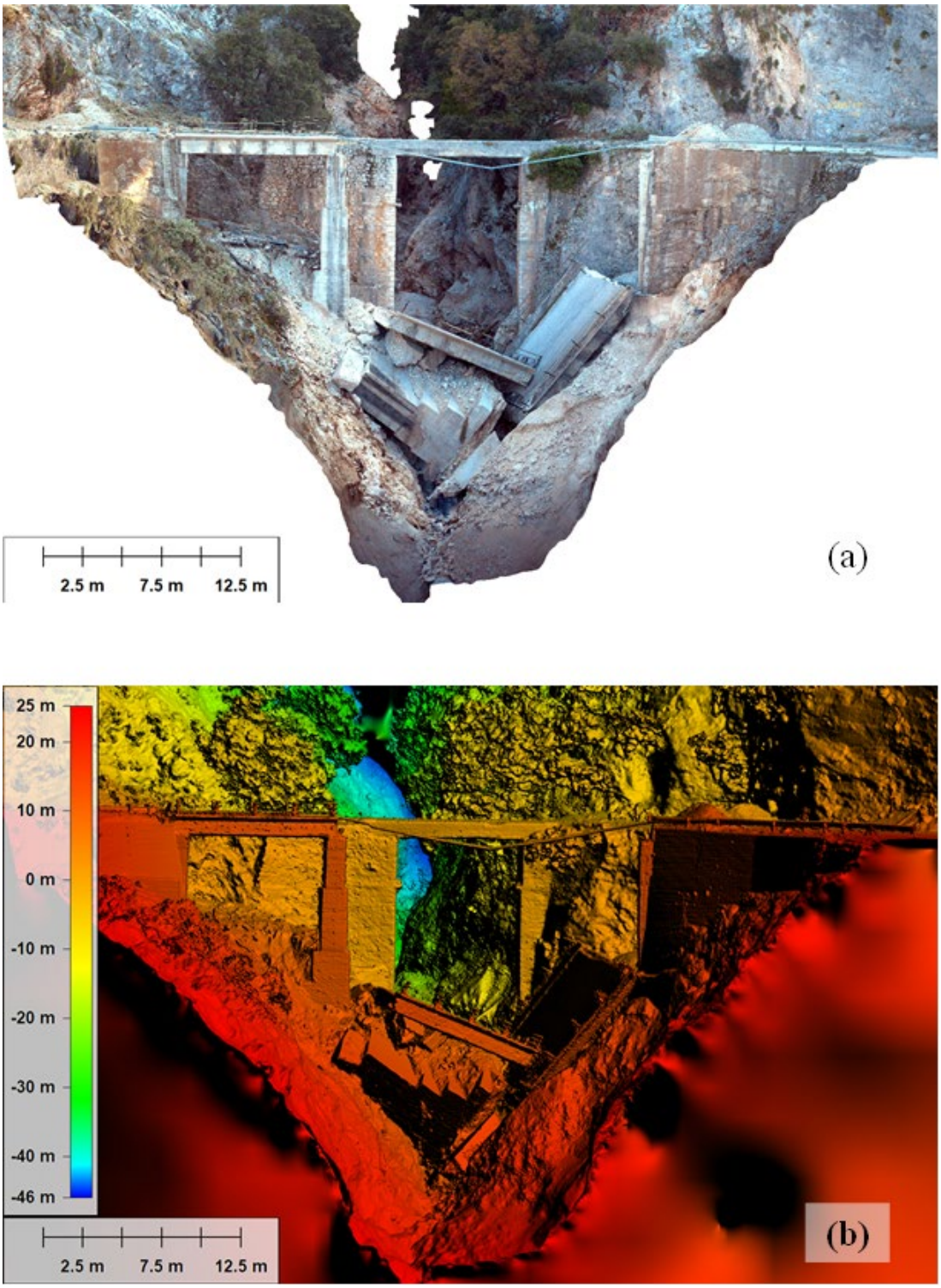

Figure 5.3. UAV-enabled mapping of collapsed bridge on E.O. Argostoliou-Fiskardou (38.319506°N, 20.508197°E): a) front-view Orthophoto, and b) front-view DSM (view 3D model at: https://skfb.ly/6WyYT)

Figure 5.4. Railway bridge foundation scour (38.9609999722°N, 22.3005999722°E): a) eroded scar of bridge foundation embankment, b) exposed pier foundation, c) view of bridge and eroded embankment, and d) indicative size of debris on site

5.1.3. Karditsa Region

A significant number of bridges were damaged in the mountainous region west of Karditsa, in the perimeter of the Plastiras Lake, and north of it, especially in Mouzaki, causing major traffic disruptions. Figure 5.5 shows a map of a total of 14 bridges inspected during a two-day trip from 2 – 3 October 2020. The color-coded pins indicate the level of structural damage suggesting an evidently milder impact on the bridges of the lowland in comparison to the mountainous areas.

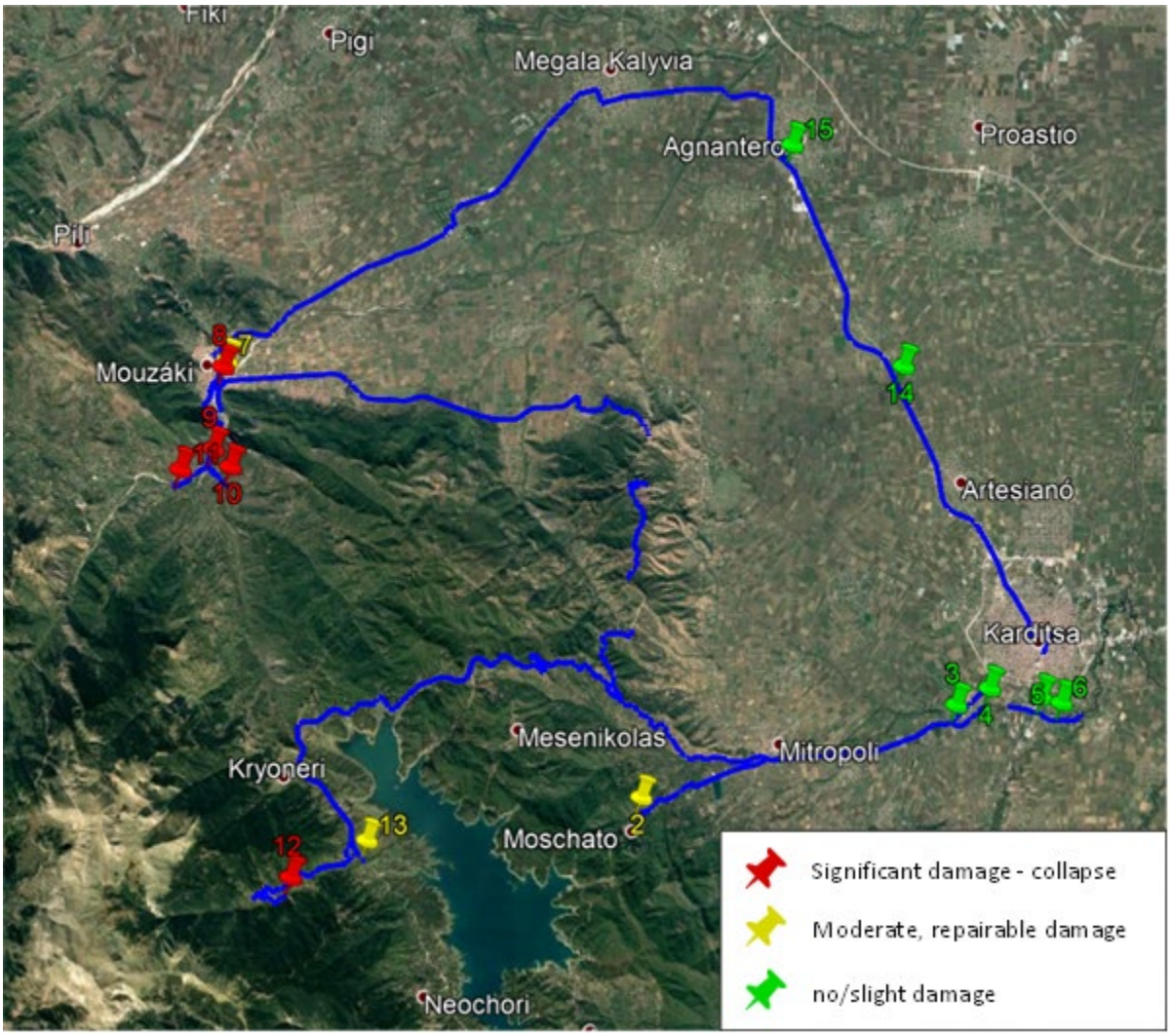

Figure 5.5. Map of bridge inspections carried out during 2 – 3 October 2020 in the area around Karditsa: the route (in blue) and the bridge locations color-coded to indicate the level of damage.

Table 5.1. Summary of observed bridge damage: red color indicates complete failure/collapse; yellow indicates significant/ repairable damage; green indicates slight/ negligible damage.

Bridge no	Latitude (° N)	Longitude (° E)	Structural Damage	Backfill Erosion	Foundation Scour	Overflow	Debris
1	39.17251203	22.09174728	—	Y	—	—	—
2	39.32248333	21.79625000	Y	Y	—	Y	Y
3	39.34458922	21.89418983	—	—	—	Y	—
4	39.348575	21.90459167	—	—	—	Y	Y
5	39.34652222	21.92067222	—	—	—	Y	Y
6	39.34506944	21.92634722	—	—	—	Y	Y
7	39.42734167	21.66727500	—	Y	likely	—	Y
8	39.42580411	21.66623306	Y	Y	Y	—	—
9	39.40610833	21.66315000	Y	Y	—	—	—
10	39.401844	21.66842078	Y	Y	—	—	—
11	39.40117261	21.65286825	Y	Y	Y	likely	Y
12	39.30350843	21.68657321	Y	Y	—	likely	Y
13	39.30956336	21.71081606	Y	Y	Y	likely	Y
14	39.09779247	21.87822363	—	—	—	Y	—
15	39.47911111	21.84343611	—	—	—	Y	—

Bridges in the lowland areas of Karditsa

Four bridges that cross the Gavria Rema (Creek), a levee-confined watercourse that forms the southern border of Karditsa, were inspected on October 2, 2020. These are bridges No. 3, 4, 5, and 6 in Table 5.1.

Bridge No. 3 (Figure 5.6) is in fact a pair of two bridges: an old, obsolete, bridge, and a new one, located a few meters upstream. Interestingly, although the upstream-most structure is generally expected to experience greater distress, the younger structure seemed unaffected by the event while the old bridge showed evidence of overtopping of flow and debris (Figure 5.6b and 5.6c). It is reasonable to assume that the new bridge was saved thanks to its wider opening. By contrast, the presence of a middle-pier, in addition to a somewhat narrower total width, critically reduced the flow capacity (hydraulic section) of the old bridge.

Bridges No. 4 (Figure 5.7), 5 (Figure 5.8), and 6 (Figure 5.9) demonstrated similar response, despite their essentially different structures and their varying ages (as well as maintenance states). All three showed evidence of overflowing and debris built-up, yet without any sign of structural damage or foundation/abutment distress. This was particularly surprising in the case of Bridge No. 6, which is evidently a very old and poorly maintained structure (Figure 5.9b). Although the water level did not allow inspection of its foundation for scour assessment, it would be reasonable to assume that there is no scour otherwise, the structure would have probably collapsed.

Accordingly, bridges of the northern lowlands of Karditsa, specifically No. 14 (Figure 5.10a) and No 15 (Figure 5.10b) were found structurally unscathed during inspections carried out on October 3, 2020, albeit with evident signs of been overtopped. According to the testimonies of local people, the surrounding fields were flooded (Figure 5.10c and 5.10d) with water height reaching a maximum of 1.5 m (at the parking lot of the Jumbo© store - location 39.475303°N; 21.845064°E).

It can be deduced that, unlike the bridges of the mountainous regions (discussed in the following), the bridges of the lowlands were generally saved by the erosive forces that would induce foundation and/or abutment scour, leading to structural damage, thanks to the following two parameters:

(1) Topography:

Soil erodibility is dependent on flow velocity. Erosion starts when a critical flow velocity magnitude (V_c) is exceeded. As flow velocity decreases proportionally with reducing ground inclination, the lowlands have an advantage against erosion/scour effects merely owing to their flat morphology.

(2) Soil Cohesion:

High plasticity clays, the dominant soil type in the lowlands (Figure 5.11), are much less erodible than the cohesionless sediments found in Mouzaki's riverbanks (Govindasamy 2009; Briaud 2008).

Figure 5.6. Photos of Bridge No. 3: a pair of RC bridges crossing the Gavria Rema along the Karditsa – Kastania provincial road (39.344589222°N; 21.894189833°E): (a) evidence of overflow over the older bridge, which is located a few meters downstream of the younger structure; (b) level of water height; (c) debris remains at the deck; and (d) side view of the structure showing no structural damage.

Figure 5.7. Photos of Bridge No. 4 of the Gavria Rema (39.348575°N; 21.904591667°E) showing significant debris build-up, but no other damage.

Figure 5.8. Photos of Bridge No. 5 (39.346522222°N; 21.920672222°E): (a) debris has been moved to the side; (b) debris built up in front of the neighboring overpass of the irrigation trench.

Figure 5.9. Photos of Bridge No.6 (39.344589222°N; 21.894189833°E): (a) debris has been moved to the side; (b) no evidence of flood induced damage despite the bridge being old and poorly maintained with exposed reinforcement.

Figure 5.10. Photos of (a) Bridge No.14 (39.097792474°N; 21.878223628°E) and (b) Bridge No. 15 (39.47911111° N; 21.84343611° E) which suffered negligible damage despite being reportedly flooded, with water heights in the (c) – (d) nearby fields exceeding 1.5 m (according to communication with local people).

Figure 5.11. Examples of the lowland's cohesive soil.

Bridges in the severely impacted mountainous region

- Single-span RC bridges

Three different single-span RC bridges were found damaged in the mountainous region south of Mouzaki on October 3, 2020. Irrespective of their structural details and exact location, they all demonstrate a similar damage pattern, characterized by excessive erosion of the abutment backfill leading to the partial or total collapse of the retaining structure. It may be deduced that the length of the three bridges was too short to accommodate the amount of water flowing during the peak of the flood. Horizontal contraction of the channel due to the presence of the abutment walls unavoidably caused a local increase of water velocities to such extent that the surrounding backfill soil was partially or fully washed away.

-Bridge No. 9 (39.406108333°N; 21.663150000°E) is shown in Figure 5.12:

Its abutments consist of unreinforced concrete gravity walls supported on shallow foundation slabs. According to testimonies, the foundation of the left wall was affected by scouring prior to the event. On September 18, 2020, flooding caused a complete wash-away of the backfill material and excessive scouring of its foundation, leaving the abutment walls unsupported. The latter collapsed (Figure 5.12b) as a result of material capacity failure, causing collapse of the overlying roadway segment and, therefore, a large gap in the road (Figure 5.12c). To investigate further the failure mechanism, on 13 October 2020, UAV-enabled mapping was performed. A visualization of the 3D model of the bridge can be seen here: https://skfb.ly/6VXHW.

-Bridge No. 10 (39.401844000°N; 21.668420778°E) - Figure 5.13:

Located in a secondary gully of the Pamisos river, on the way from Mouzaki to Ellinokastro this box structure suffered significant damage due to erosion of abutment backfills on both banks (Figure 5.13a and 5.13b). Flooding in this location was such that the neighboring fields were found covered in mud, two weeks after the flood.

-Bridge No. 13 (39.309563356° N; 21.710816055° E) - Figure 5.14:

This bridge consists of a RC beam supported on (possibly) older masonry walls that function as abutments. Its southern abutment was partially washed away, leaving a significant part of the deck unsupported (Figure 5.14b) while backfill erosion led to the formation of a 4 m wide gap in the roadway.

Figure 5.12. Photos of the collapsed Bridge No. 9 crossing Pamisos river about 2 km north of Mouzaki (39.406108333°N; 21.663150000°E): (a) side view indicating abutment backfill erosion and the location of the collapsed roadway segment; (b) closer view of failed abutment wall; and (c) the roadway gap.

Figure 5.13. Bridge No. 10 crossing a secondary gully on the way from Mouzaki to Ellinokastro (39.401844000° N; 21.668420778° E): (a) western abutment; (b) eastern abutment; and (c) – (d) photos of surrounding fields indicating widespread flooding.

Figure 5.14. Photos of Bridge No. 13 located east of the Plastiras lake (39.309563356°N; 21.710816055°E): (a) side view indicating debris built-up and (b) significant abutment scouring and (c) backfill erosion that leads to the partial collapse of the roadway.

- Multi-span RC bridges

Failure of multi-span bridges was due to a combination of abutment scour, backfill erosion and pier scour. A total of three case studies were identified within a radius of 3 km from the center of Mouzaki:

- Bridge No. 7 (Figure 5.15) is critical for the town's transportation infrastructure, being part of the provincial road that connects it to Karditsa. According to local news coverage (Figure 5.16), the bridge was subjected to substantial damage, leading to a temporary closure due to the collapse of a roadway segment behind its N-W (left side) abutment. Yet, this damage was already restored on October 2, 2020, when the inspection team found the bridge open to traffic (Figure 5.15a). Nevertheless, inspection of the riverbank revealed significant scour of the piled foundation that supports the abutment. An average height of 1.9 m of the foundation piles was exposed (Figure 5.15b). One of the four piles that we could observe (at the downstream corner) was evidently corroded. Yet, this was probably the result of insufficient concrete cover during installation of the piles. A local engineer, who had inspected the bridge in August 2020, informed us that he had not observed any scour at the time. As such, it can be assumed that the 1.9 m deep scour hole (5.15b) was entirely the result of Ianos Medicane.

  Our observations confirm the meander effect discussed in the following. The SE (right in Figure 5.15a) abutment of the bridge showed no erosion at all, nor any other damage (Figure 5.15c). This abutment was, according to the testimony of a local engineer, identical to the opposite, NW, one until August 2020. Their strikingly different response to this event can be attributed to the meander effect discussed in the following.

  This abutment is located in the convex side of the meander, where water velocities are reduced in comparison to the concave side. The meander Moreover, remains of debris stuck at the top of the pier column (Figure 5.15) confirm that the maximum water height reached the level of the deck, in agreement with media reports (Figure 5.16a).

- Bridge No 8 (Figure 5.17 - 5.18) is an older structure, located at a distance of 200 m only from No. 7, upstream. It was, in recent years, used as a pedestrian bridge. In fact, the relatively short length of this structure causes a recognizable contraction point along the Pamissos channel (Figure 19a), which likely caused increased flow velocities downstream and, thereby, the excessive erosion of the riverbank (note that we observed significantly limited riverbank erosion upstream of Bridge No.8).

  The structure consists of girder beams supported by 4 RC piers and the abutments (Figure 5.17a). Similar to the previously discussed case, the damage is concentrated on the left (N-W) side of the bridge, manifested by the evident settlement of pier 2 and the associated rotation of the deck. Remarkably, this pier showed no evident rotation, as is usually the

case with scoured piers (Figure 5.17b). There was also no observable scour hole around its foundation (the latter is probably a shallow footing). This could be due to the modifications in the riverbank caused by post-event construction works, or could suggest that scouring took place deeper, beneath the foundation. Nevertheless, we observed substantial scour at the foundations of Pier 1 (Figure 5.17d) and the left abutment (Figure 5.17c).

The damage of Bridge 8 (Figure 5.18) is quite severe, probably irreparable, and the structure remains inaccessible. Figure 5.19 elucidates the mechanics behind the observed asymmetry between left and right river banks, in terms of erosion and general damage. In fact, such asymmetry is typically the case in meandering rivers, as flow around such channel bends leads to increased velocity and erosion of the outer, concave bank (meander effect).

- Bridge No. 11 (Figure 5.21) crosses Pamissos at a horizontal distance of 3.2 km from Mouzaki, upstream. The bridge collapsed completely as a result of pier scour and abutment erosion. Based on the deformation of the deck, it is reasonable to deduce that there were two additional piers (i.e. a total of 3 piers) at the locations indicated in Figure 5.21a, which likely suffered significant rotation due to scour, similar to the abutment (Figure 5.21c). Yet, we could not locate these piers when we visited on October 3, 2020. Likewise, we could not locate the middle span of the deck, which is evident in footage that appeared in the local media the day after the event (see screenshot in Figure 5.22).

  It is important to note that Bridge No. 11 was known to have suffered scour induced deformation prior to this medicane (observed during inspections carried out in August 2020). In August 2020, it was decided to replace it soon with a new bridge, constructed upstream. Construction was ongoing next to Bridge No.11 during our visit on October 3, 2020 (Figure 5.23), which according to workers' testimonies had begun prior to the event.

Figure 5.15. Photos of Bridge No. 7, the road bridge crossing Pamissos river in the center of Mouzaki (39.427341667°N; 21.667275000°E): (a) side view; (b) abutment scour; (c) unaffected, opposite (SE) side; (d) debris stuck within the connection between pier and deck indicating flood water height.

Figure 5.16. Footage of Bridge No. 7, in local news showing: (a) the water height on September 18, 2020 (https://www.youtube.com/watch?v=7TzUZh3YgxY); and (b) – (c) the abutment failure and associated roadway collapse (https://www.youtube.com/watch?v=hLP3NdMF9SI).

Figure 5.17. Photos of the severely damaged pedestrian bridge in Mouzaki, i.e. Bridge No. 8 (39.425804111°N; 21.666233056°E): (a) longitudinal direction indicating the substantial settlement of the left side (Pier 2) and the associated rotation of the deck; (b) closer view of piers 2 and 3; (c) the evidently unaffected right side; (d) scour at P1; and (e) abutment scour and backfill erosion.

Figure 5.18. Photos of Bridge No. 8 taken from the level of the roadway: (a) abutment erosion; (b) settlement induced step; (c) – (d) extension cracks over Pier 3.

Figure 5.19. (a) Drone footage captured on September 19, 2020 (source: https://www.youtube.com/watch?v=3bqDobqMuC0) showing that erosion damage was concentrated on the left (N-W) riverbank while the right (S-E) side remained unaffected; (b) river course geometry that helps explain the scour of the exterior bank of the river..

Figure 5.20. Orthophoto of bridges No. 7 and 8 at the village of Mouzaki (2 October 2020).

Figure 5.21. Photos of Bridge No. 11 (39.401172611°N; 21.652868250°E) which evidently collapsed due to a combination of abutment and pier scour: (a) side view, (b) - (c) bearing capacity failure of the abutment and deck collapse.

Figure 5.22. Footage of Bridge No.11 in the local news on September 19, 2020 (source: https://www.youtube.com/watch?v=hLP3NdMF9SI).

Figure 5.23. New bridge being constructed next to the collapsed bridge No. 11.

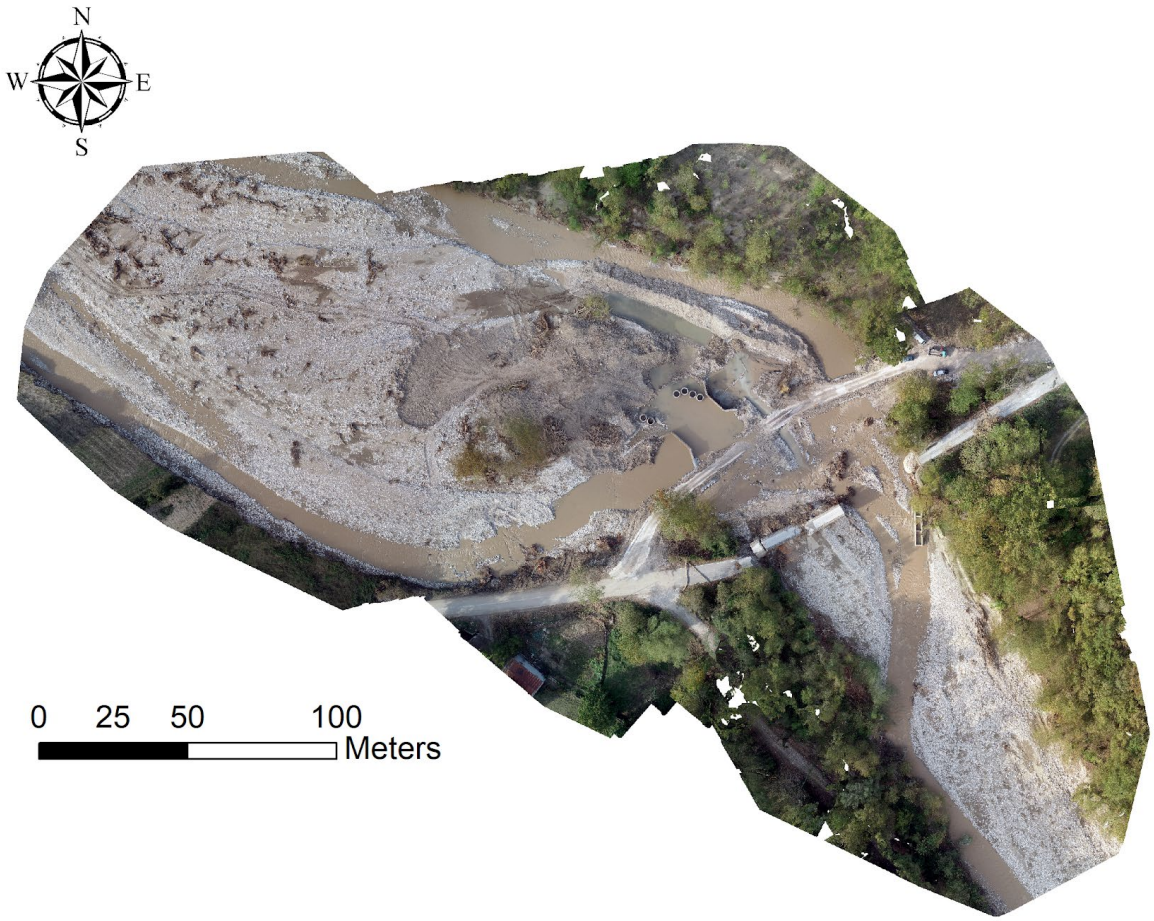

Figure 5.24. Orthophoto of bridge No. 11 near the village of Mouzaki (2 October 2020).

- Old Masonry Bridges

Similar to the previously discussed single-span RC bridges, the response of two old masonry arches found in the area was dominated by abutment erosion (Figures 5.25 and 5.26). Particularly interesting is the case of Bridge No. 2 (Figure 5.25), which is considered a cultural monument with an estimated age of 300 years. Its integrity was certainly undermined by the modern, narrower overpass located at a close distance upstream (Figure 5.25). The latter, presumably, caused contraction of water flow leading to increased flow velocities impacting Bridge No.2.

Figure 5.25. Photos of Bridge No.2, a masonry arch near Moschato (39.32248333°N; 21.79625000°E): (a) – (b) part of it was being reconstructed on 2/10/2020, while (c) there was a significant amount of debris upstream, especially in the (d) modern (RC) overpass.

Figure 5.26. Photos of Bridge No.12, a masonry arch located on the way from Filakti to Pezoula (39.303508426°N; 21.686573208°E): (a) – (b) suffering extended abutment and riverside erosion that lead to (c) collapse of the roadway.

5.2. Road Networks

5.2.1. Cephalonia Island

The road network of Cephalonia was heavily impacted by the passage of Medicane Ianos. Road embankments experienced partial failure in numerous locations across the island, while at a few locations the network was severely compromised (Figure 5.27). These failures were primarily caused by flood/debris-related extensive erosion of embankment material rather than slope instability. This remark is supported by the observation that, typically, the locations of failures coincided with the presence of debris within gullies (Figure 5.27). Often, compromised flood protection/drainage conduits were identified (Figures 5.27b and 5.27e), indicating inadequate capacity of the existing road network flood protection systems against phenomena such as Medicane Ianos.

It is worthwhile to note that the road leading to Myrtos beach, through the village of Divarata, was completely obstructed (Figure 5.27f), due to a combination of embankment erosion, fallen trees, and landslides (see section 6.2). Moreover, along the road connecting the villages Dilinata and Drapano, a different type of failure was identified. An earth slope of quarry-related material depository exhibited a rotational movement that resulted in heaving and cracking of the nearby road (Figure 5.28). Evidence of heaving and cracking was present along a distance of approximately 150 m. The developed cracks, which at places exposed utility lines, reached a width up to ~3 m and a length of 20-30 m (Figure 5.28).

Figure 5.27. Road embankment failures across Cephalonia due to flood/debris related erosion: a,b) 38.325680556°N, 20.551658333°E, c,d) 38.310936111°N, 20.576272222°E, e) 38.326667°N, 20.518333°E, and f) 38.335719444°N, 20.543761111°E

Figure 5.28. Roadside slope failure that led to road heave and cracks along a 150 m stretch (38.201636111°N, 20.502291667°E)

5.2.2. Lamia Region

The road network across the Spercheios river valley and the surrounding areas was impacted by Ianos. In particular, road embankment erosion was recorded in several locations (Figures 5.29, and 5.30), with the road parallel to E.O. Lamia-Karpenisi (38.92455°N, 22.27771944°E) being almost entirely washed away (Figure 5.29c).

Figure 5.29. Road embankment failures in the region of Lamia: a) at Gorgopotamos (38.83451944°N, 22.39527499°E); b) north of Stirfaka (38.96918055°N, 22.29513611°E); c) along the E.O. Lamia Karpenisi (38.92455°N, 22.27771944°E); d) near Paliouri (38.94233611°N, 22.21619722°E)

Figure 5.30. UAV-enabled orthophoto of road failure on E.O. Lamia-Karpenisi (38.94233611°N, 22.21619722°E)

5.2.3. Karditsa Region

In this area, along the road section between Kastania and Rachoula (total length of about 10 km), extensive sliding occurred. The flysch type consists mainly of shales. During the time of the visit the road was covered with slipped material on either side, but remained accessible (see Figure 5.31).

At the location before Rachoula village, the road was completely damaged due to the extensive erosion in the riverbed and the impact of the transported materials on the road (see Figure 5.32). The riverbank erosion was accompanied by a complex rotational-type slope failure in sandstone flysch. The height of the landslide's crown was about 30 m and material travelled at a distance of around 200 m (Figure 5.33).

Figure 5.31. Landslips from side slopes along the Kastania – Rachoula section (39.2314830°N, 21.8016040°E)

Figure 5.32. Damaged road near Rachoula due to impact of transported materials (39.2494490°N, 21.8889110°E)

Figure 5.33. Complex rotational-type slope failure near Rachoula (39.2494490°N, 21.8889110°E)

5.3 Railways

5.3.1. Overview of railway effects in western Thessaly

The railway line crossing central Greece (Figure 5.34) was affected by the flooding and mass wasting instigated by the Medicane Ianos. There was a temporary closure of the line Athens - Thessaloniki, while the line Kalabaka-Paleofarsalos remains closed due to severe damage and is gradually being repaired.

Apart from local rock falls and landslides triggered along the railway line between Domokos and Bralos, the most frequent cause of railway damages was embankment and ballast scouring & breaching (Tsubaki et al. 2012, 2017, Figure 5.35). Damages were reported and identified in mainly three areas; the Paleofarsalos-Stavros area (flooded by Sofaditis and Enipeas rivers), Karditsa-Sofades section of the rail line, and the area flooded by Pamisos river between Megala Kalyvia and Fanari.

Field survey was focused on the area between Magoula and Megala Kalyvia, described in the next section. However, we identified multiple locations of railway ballast scouring in other parts of west Thessaly plain (see examples in Figure 5.36). For the ballast washout identification, we used Sentinel-2 true colour imagery (RGB-432) acquired in September 20 & 25 2020, enhanced using Sub-Pixel Convolutional Neural Network (super-resolution) for improvement of visual interpretation.

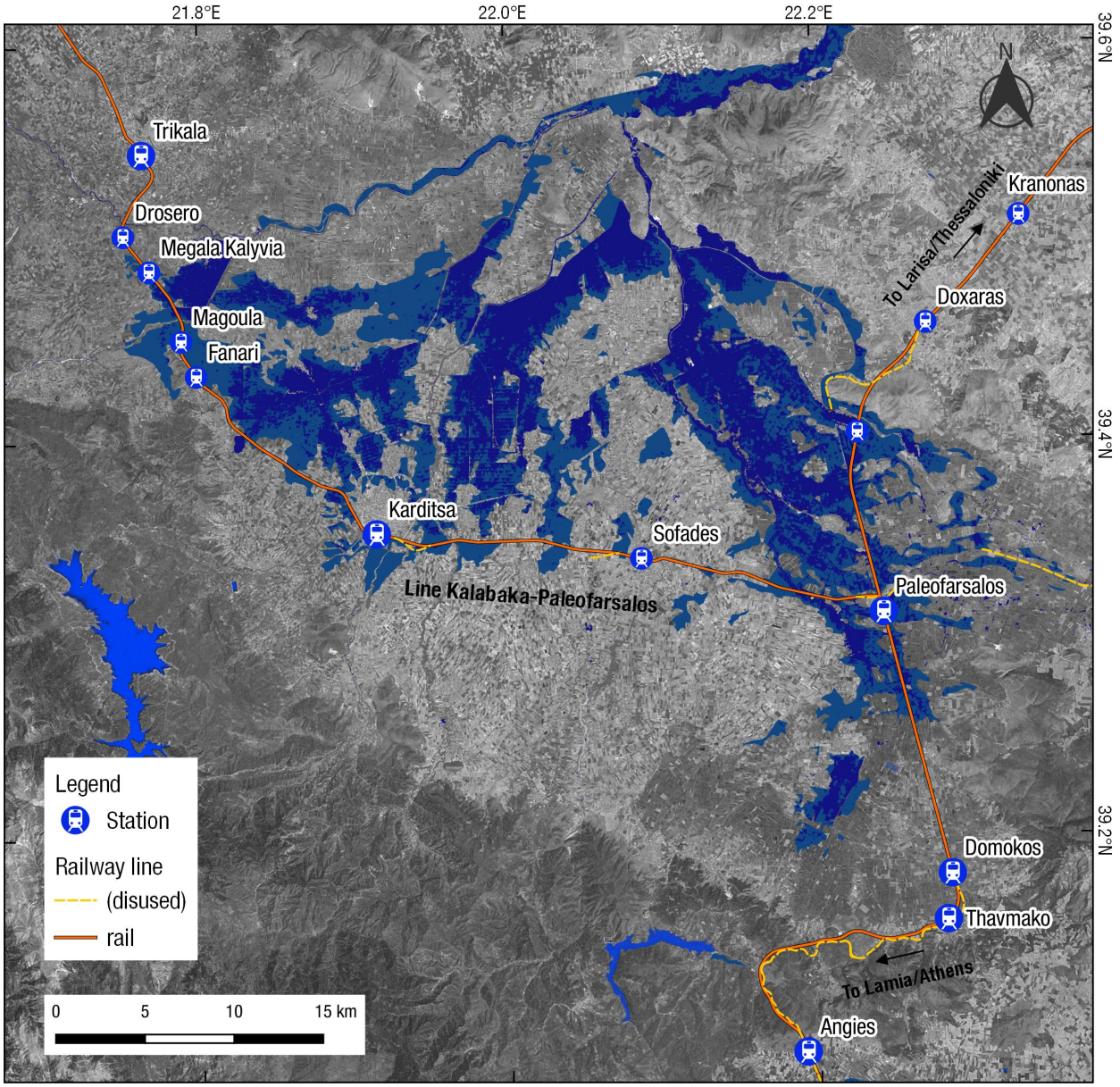

Figure 5.34. Map of the railway network in western Thessaly area, in comparison with flood-affected areas (blue areas) during Medicane Ianos.

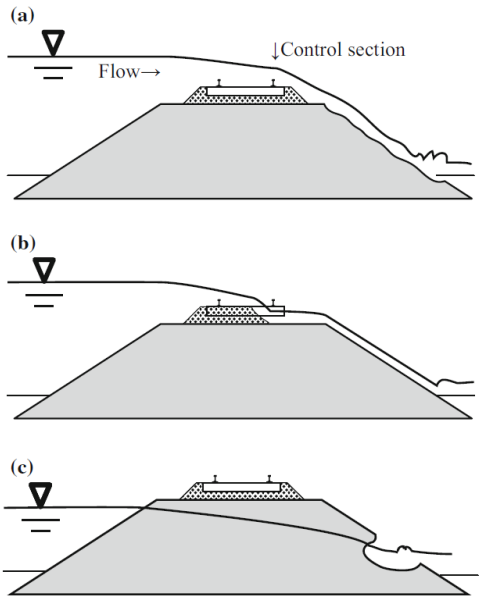

Figure 5.35. Possible types of railway embankment failures during flooding: a) a lee slope breach, b) a ballast layer breach, c) embankment seepage. From Tsubaki et al. (2016, 2017).

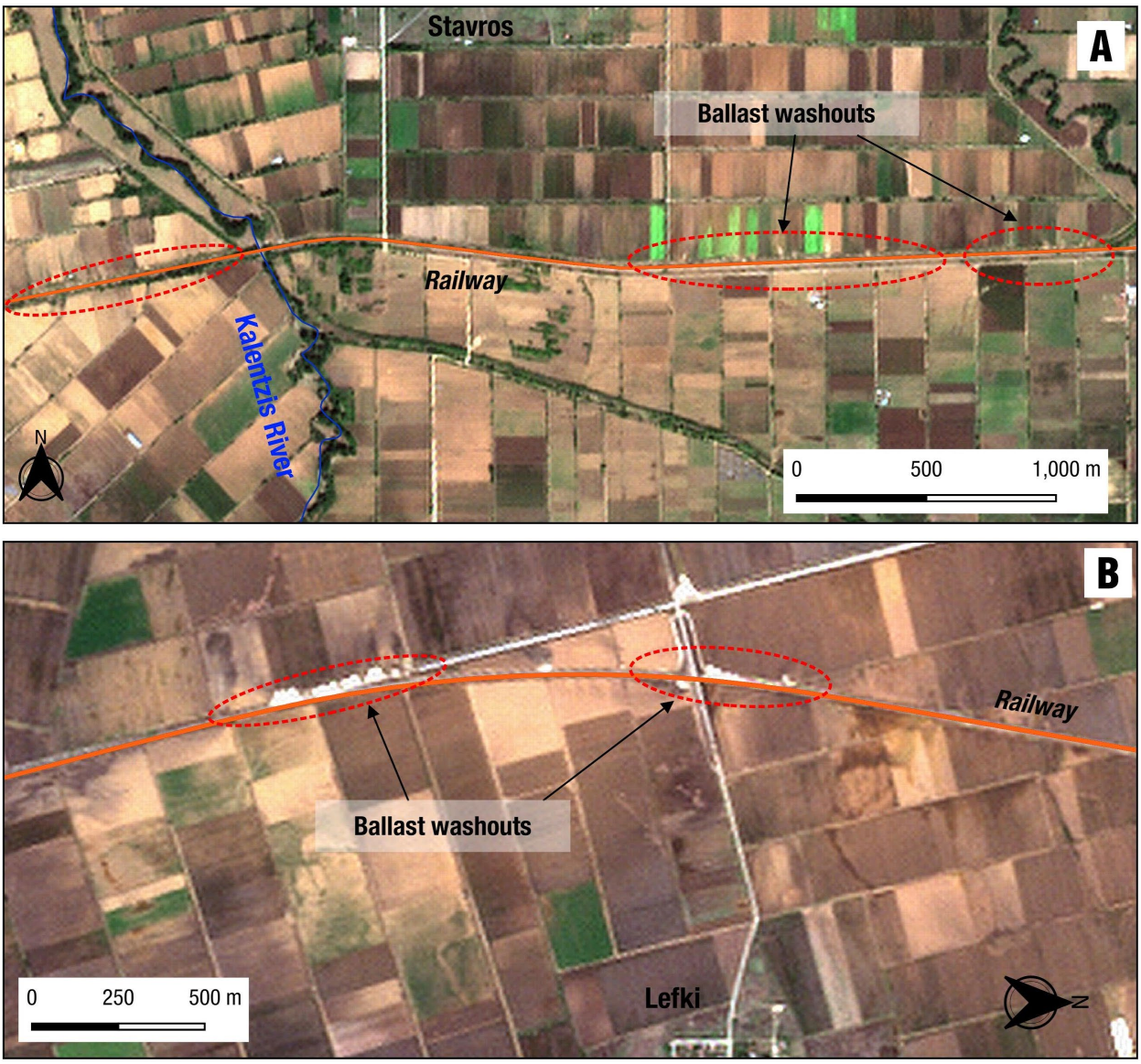

Figure 5.36. Locations of significant washout along the railway line embankment, distinguished by the lateral flow of eroded material (ballast washouts). A) Railway line Kalabaka-Paleofarsalos, east of Karditsa (map center location 39.34951°N, 21.9852°E). B) Railway line Paleofarsalos-Larisa, north of Paleofarsalos (Stavros) (map center location 39.3800°N, 22.2234°E). Sentinel-2 true color imagery (RGB432) acquired in September 25 2020, enhanced using Sub-Pixel Convolutional Neural Network (super-resolution).

5.3.2. Magoula Station Site

Magoula station and the adjacent railway line, is situated near Pamisos river. At this area, Pamisos natural stream bed is being diverted through an artificial canal into Pinios river. The abandoned Pamisos stream bed is survived by a small stream flowing between Magoula and Paleochori villages. Magoula station site was surveyed by UAV, and a photogrammetric point cloud, digital surface model and orthophotomap was extracted (as shown in subsequent figures).

Severe flooding outburst by Pamisos river discharged large amounts of water towards two directions: to the north, flooding the area around Megala Kalyvia, and to the east towards Magoula. Field survey of Magoula train station and rail track showed severe ballast scouring that deformed the rail line along significant parts of the line. The rail track is composed of metal rail lines and cement sleepers, over a ~0.5m thick ballast underbed, over an earth embankment. Flood waters breached and eroded the ballast, deforming the rail line and leaving parts of the rail track hanging. The direction of the flood water flow towards east, is evident by oriented remnant vegetation, and the direction of ballast washout towards the east side of the rail track. Figures 5.37 through 5.47 document in detail the observations made at the Magoula Station Site.

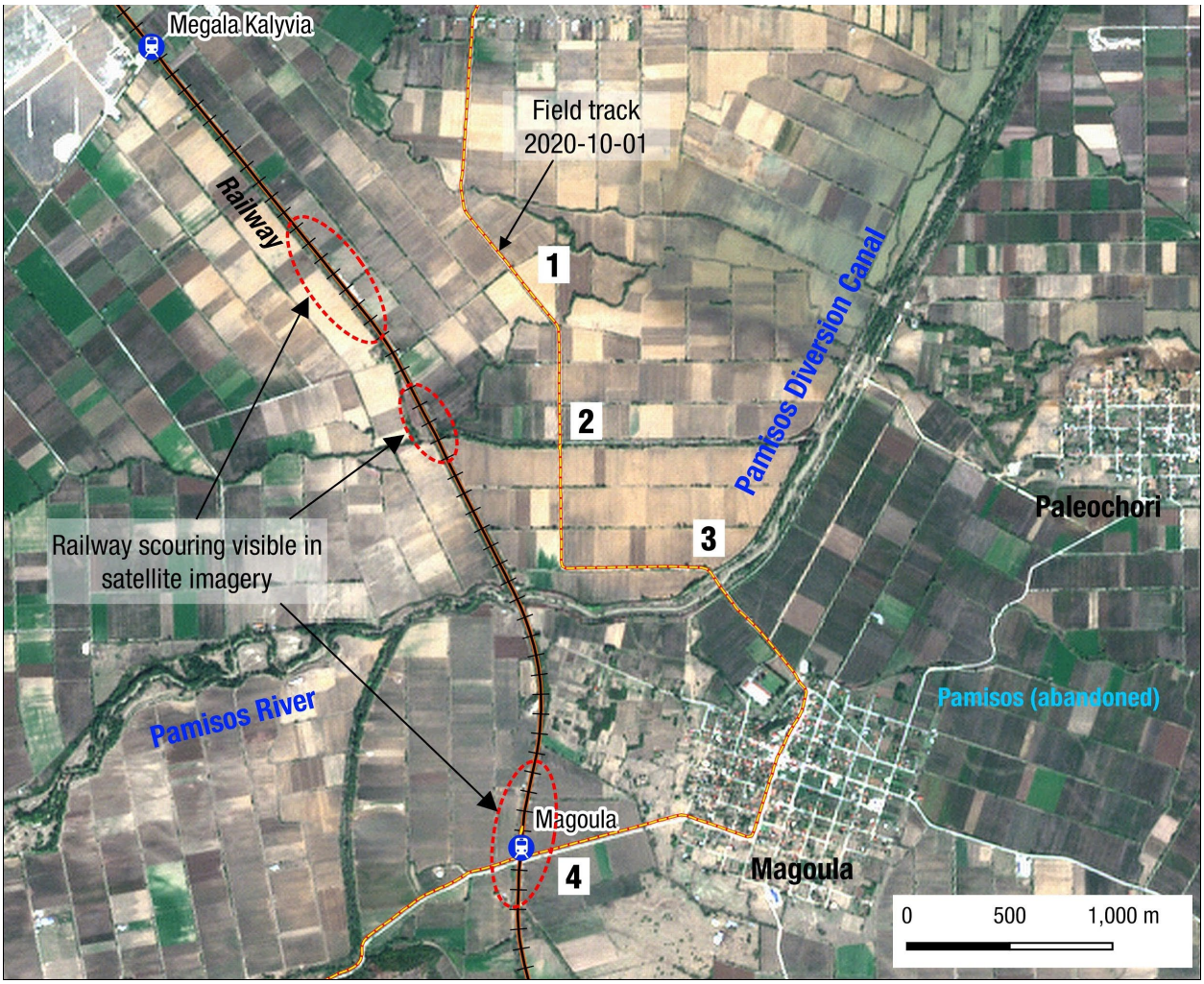

Figure 5.37. Overview of Pamisos river area between Megala Kalyvia, to the north, and Magoula, Karditsa. This area suffered extensive flooding from the overflow of Pamisos river and canal. Whitish/beige areas in the Sentinel-2 image were overrun by flood waters or remain flooded in the date of acquisition (September 25). Locations of significant scouring along the railway line embankment are marked with dotted ellipses, identified by the lateral flow of eroded material (ballast washouts). Numbers 1-4 mark points of interest shown in the next figures. 1 - Flooded fields, 2 - canal bridge, 3 - Pamisos bridge, 4 - Magoula train station. Sentinel-2 true colour imagery (RGB432) acquired on September 25 2020, enhanced using Sub-Pixel Convolutional Neural Network (super-resolution).

Figure 5.38. 1) Flooded areas south of Megala Kalyvia, Trikala (39.4765°N, 21.7887°E). 2) Road bridge over an irrigation canal (39.4694°N, 21.7907°E). Debris and flood deposits over the deck (upstream view) show that the maximum flood level exceeded the bridge height.

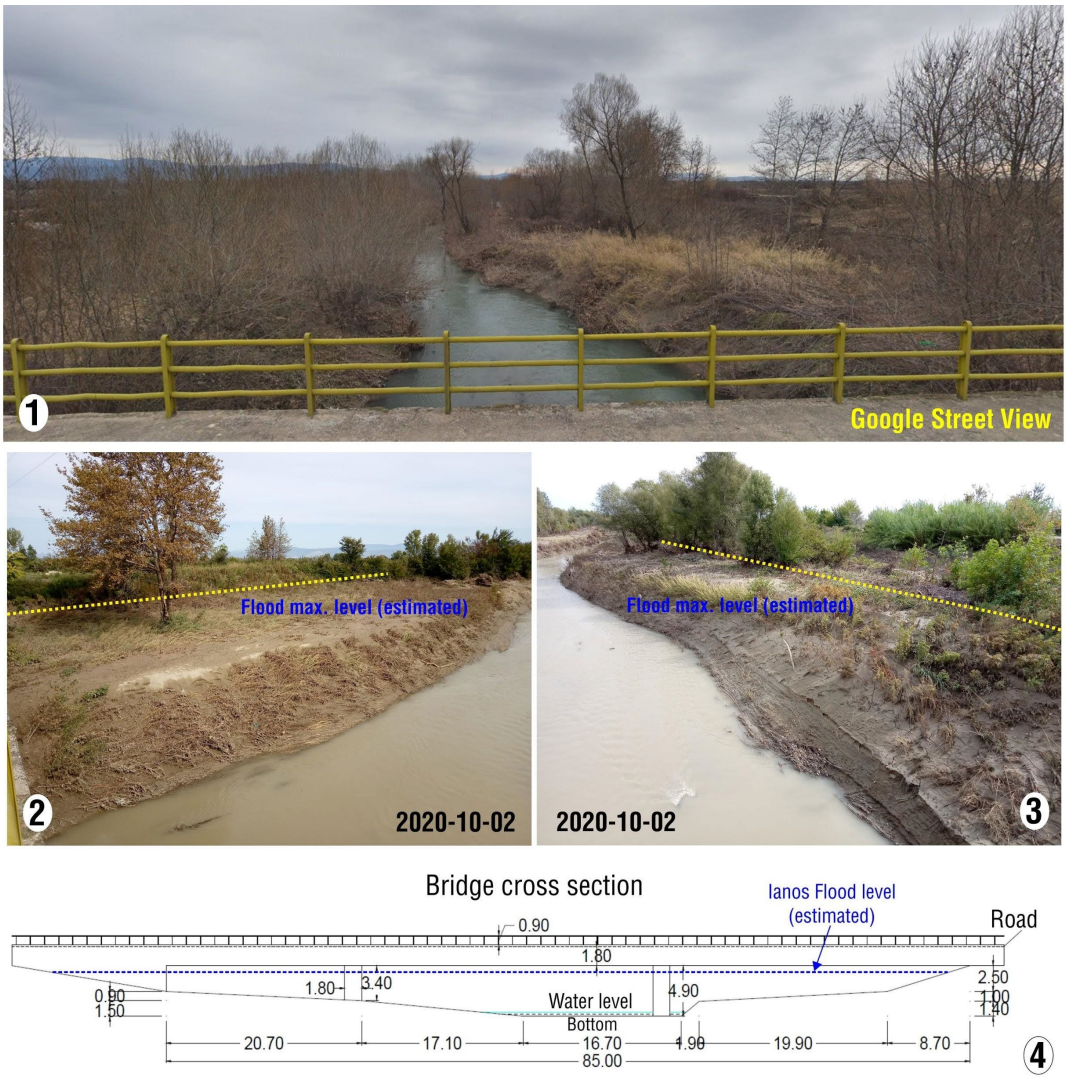

Figure 5.39. Road bridge over Pamisos canal, view to the east - downstream (39.46341°N, 21.79944°E). Field photos (2,3) compared with pre-event Google Street View image (1) and technical cross section. Maximum flood level did not overtop the bridge, but is estimated close to ~4 meters from the bottom.

Figure 5.40. Railway embankment & ballast scouring at Magoula train station (39.45127°N, 21.78824°E).

Figure 5.41. Railway embankment & ballast scouring along Paleofarsalos-Kalabaka line, near Magoula (39.45127°N, 21.78824°E). Comparison of field photo (bottom) with pre-event Google Street View image (top).

Figure 5.42. Railway embankment & ballast scouring along Paleofarsalos-Kalabaka line, Magoula station (39.45127°N, 21.78824°E). Comparison of field photo (bottom) with pre-event Google Street View image (top).

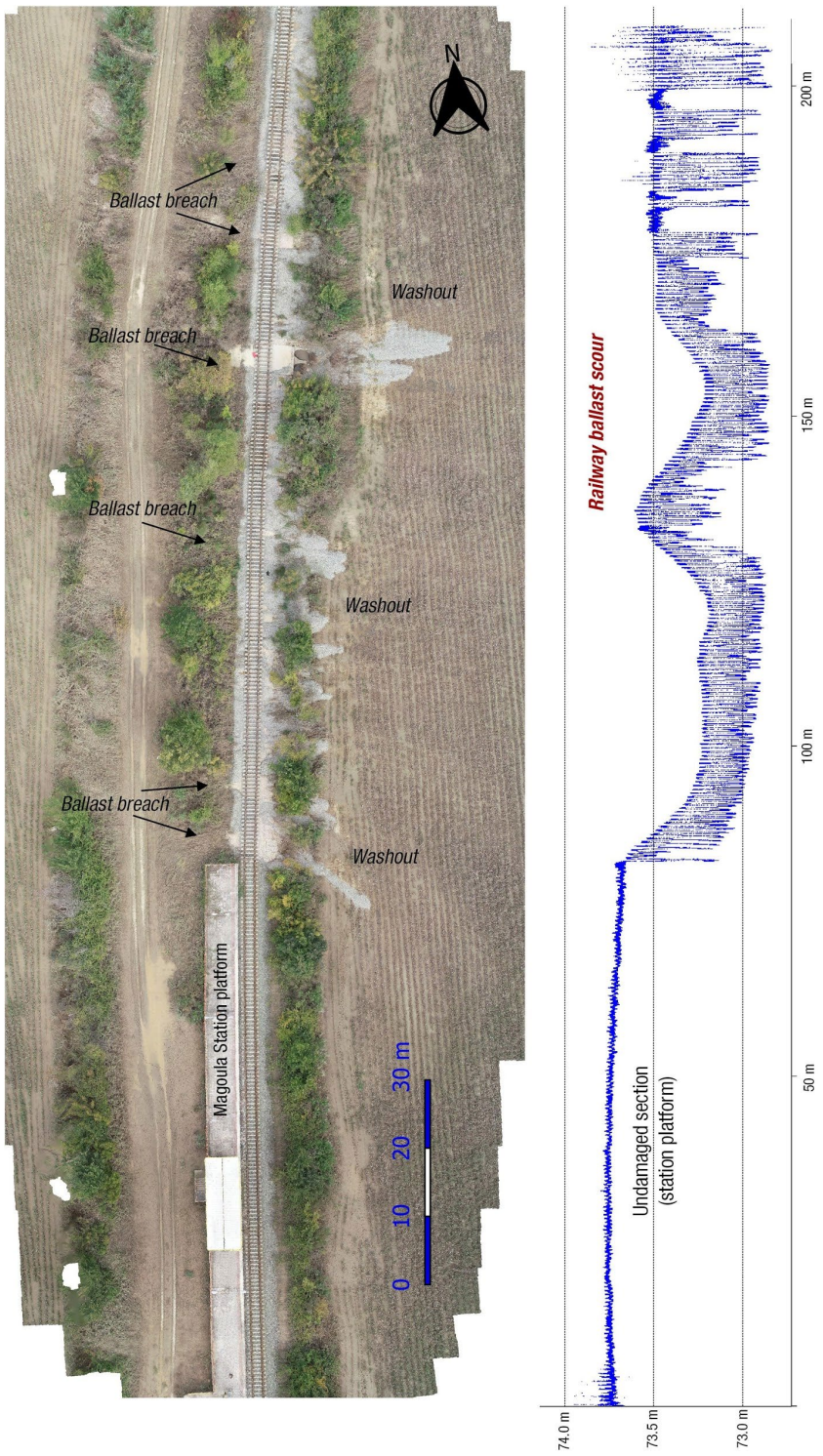

Figure 5.43. Orthophotomap (left) from the UAV survey in Magoula Station site and point cloud profile along the rail track (right) that shows deformation of the rail line due to ballast scouring.

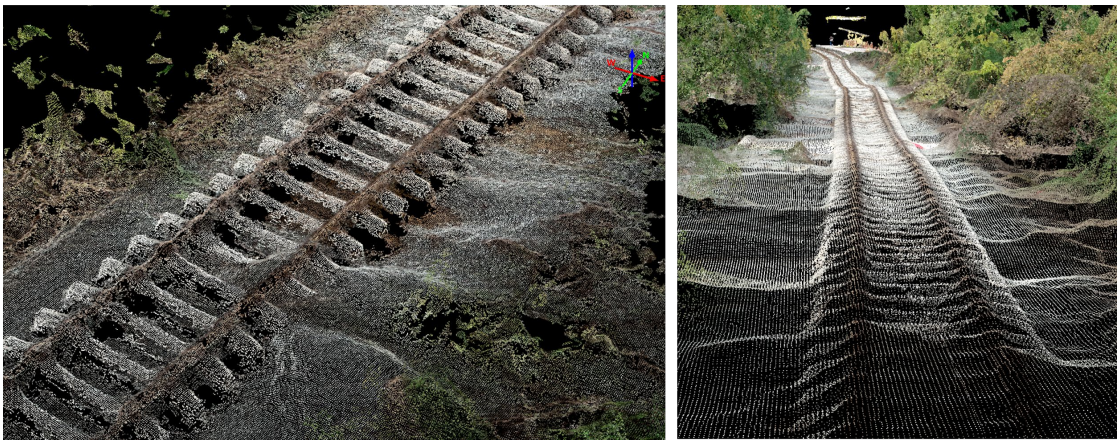

Figure 5.44. 3D Point cloud views of railway ballast breach (left) and rail line deformation (right).

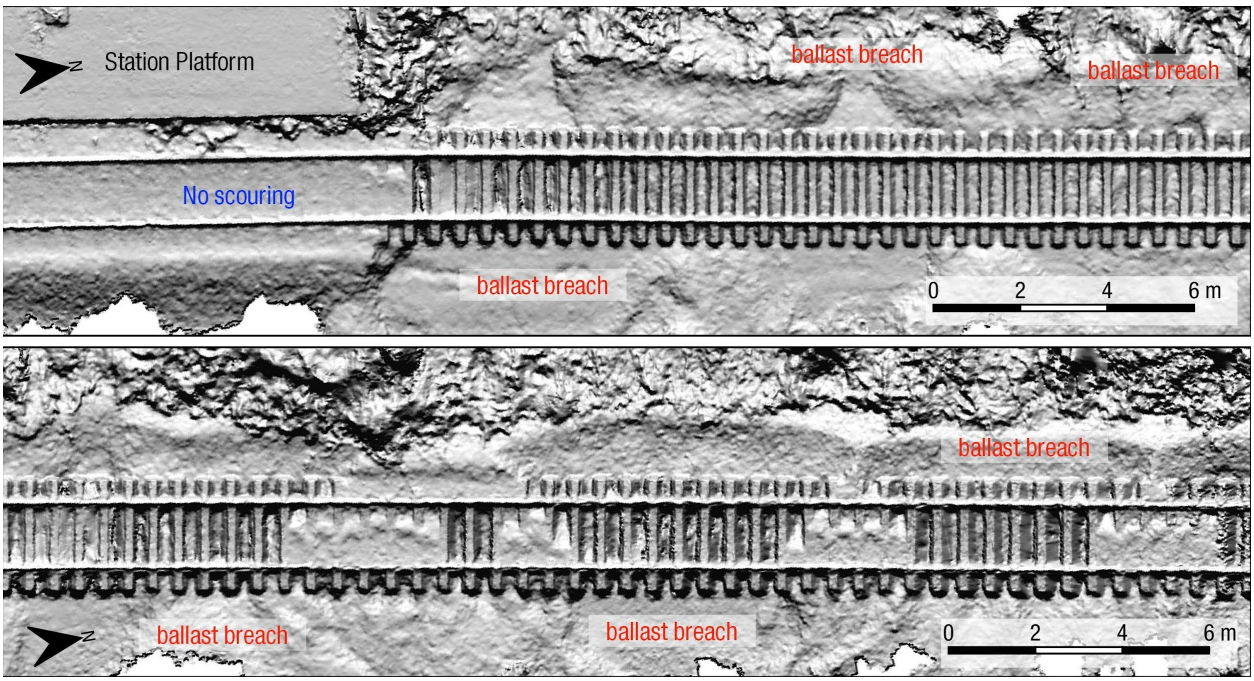

Figure 5.45. Close-ups of digital surface model (from UAV survey) along the rail track bed. Removal of ballast is visible as has created empty space between and below the sleepers. The protection of the track bed from scouring, due to the presence of the (cement) station platform, is visible in the top figure.

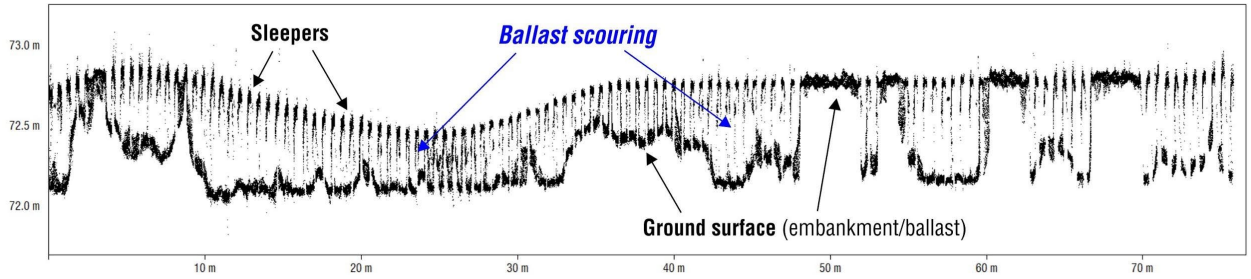

Figure 5.46. Point cloud swath profile, between the rails, along a part of the track near Magoula station. Ballast scouring in various spots is visible, that has left the sleepers and lines hanging.

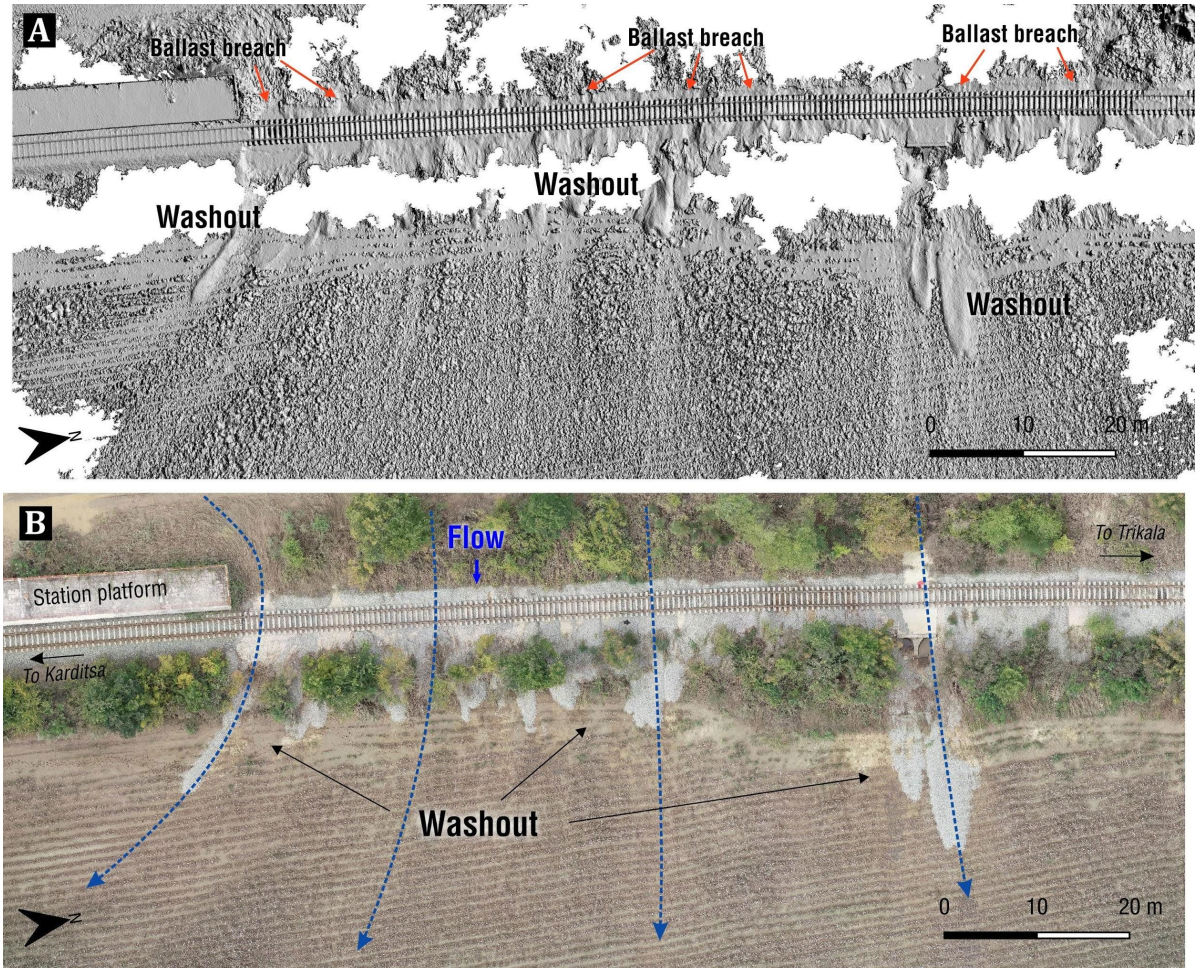

Figure 5.47. Railway ballast scouring effects in Magoula Station site. Flood water flow can be inferred from oriented overrun vegetation and the morphology/distribution of washout ballast in the eastern side of the rail line embankment. Top: digital surface model from UAV survey, bottom: UAV orthophoto.

6. Landslides, Rockfalls and Debris Flows

6.1. Types of landslides

A wide range of landslides were triggered by Medicane Ianos. The slides affected infrastructure, primarily the road network and have led to either partial collapse or complete failure of roadways. In other cases, landslides affected houses and communities, as for example in Assos, Cephalonia, where a debris flow devastated the local community. They can be grouped in the following categories:

1. Landslides involving soils and fractured and weathered rockmasses: These landslides have commonly a rotational component near the crest and are either entirely restricted in soils or involved weathered rock masses.
2. Rockslides, rockfalls and Structurally-controlled failure: These are instabilities associated with a block being dislodged, or slides that engage primarily rocks or structurally-controlled failures, i.e., failures along planes or wedges of a rock.
3. Debris flows: These are fluidized masses of soil and rock that most commonly activated in drainage accumulation areas and travelled significant distances

6.2. Landslides involving Soils and Fractured and Weathered Rockmasses

6.2.1. Cephalonia and Lefkada Islands

A landslide was identified along the steep western slopes of Cephalonia, near the village of Assos (Figure 6.1) and engaged the soils and weathered limestone/dolomite formations. Due to the steep topography the slipped material traveled a long distance. A few rotational landslides were identified along the road leading to Myrtos beach, through the village of Divarata (Figure 6.2). Access to Myrtos beach was impossible due to landslides and debris covering the roadway. Thus, mapping using UAVs revealed several landslips and related features (ex. debris). Figure 6.3 illustrates a comparison between a pre-event (May 24 2016), UAV-enabled, 3D textured mesh of Myrtos beach and its post-event counterpart. A 3D model of the area is visualized here: https://skfb.ly/6WyR6.

In Lefkada, the unfavorable wind conditions did not allow for UAV deployment for mapping purposes and thus imagery was collected primarily from the ground. Landslides along the coast were identified in several instances (Figure 6.4) and especially along the western coastline of Lefkada that had most recently experienced numerous landslides during the 2015 earthquake. These areas were affected by the precipitation with fresh sediment and debris found on the roads and at the beach (Figure 6.5). Previous mapping in the area last year had shown that the landslides remained active and thus, mapping the coastline to quantify that activity is valuable.

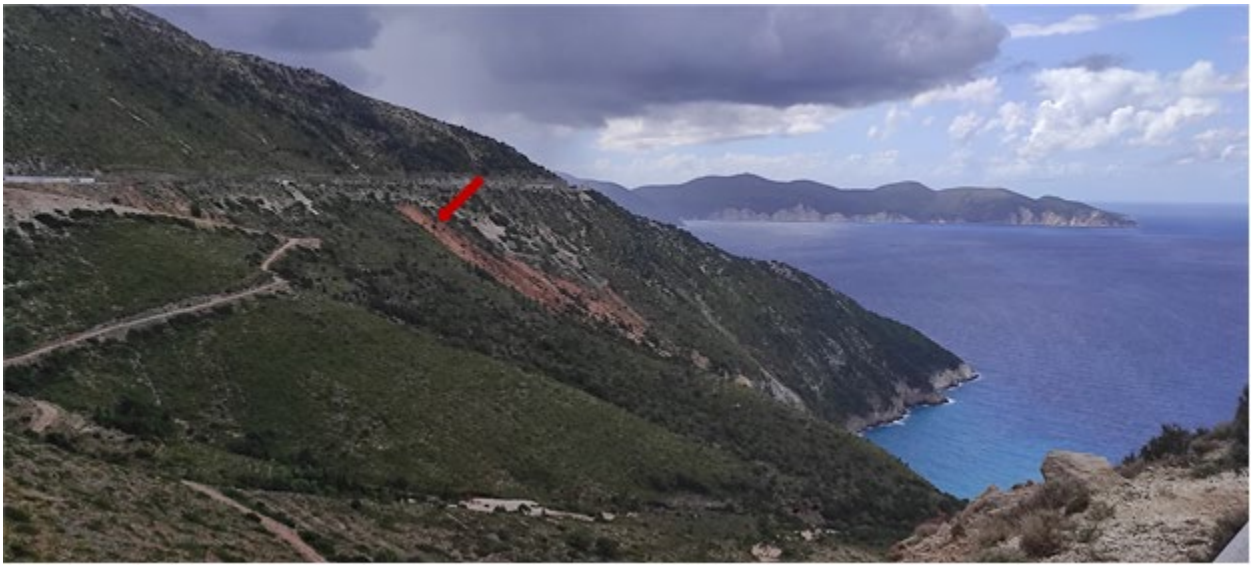

Figure 6.1. Landslide on limestone/dolomite weathered bedrock (38.354888°N, 20.5537649722°E)

Figure 6.2. Rotational slides along the road to Myrtos beach through Divarata village: a) 38.33571944°N, 20.543633°E; b) 38.3365027°N, 20.5427166°E, c) 38.337106°N, 20.541785°E

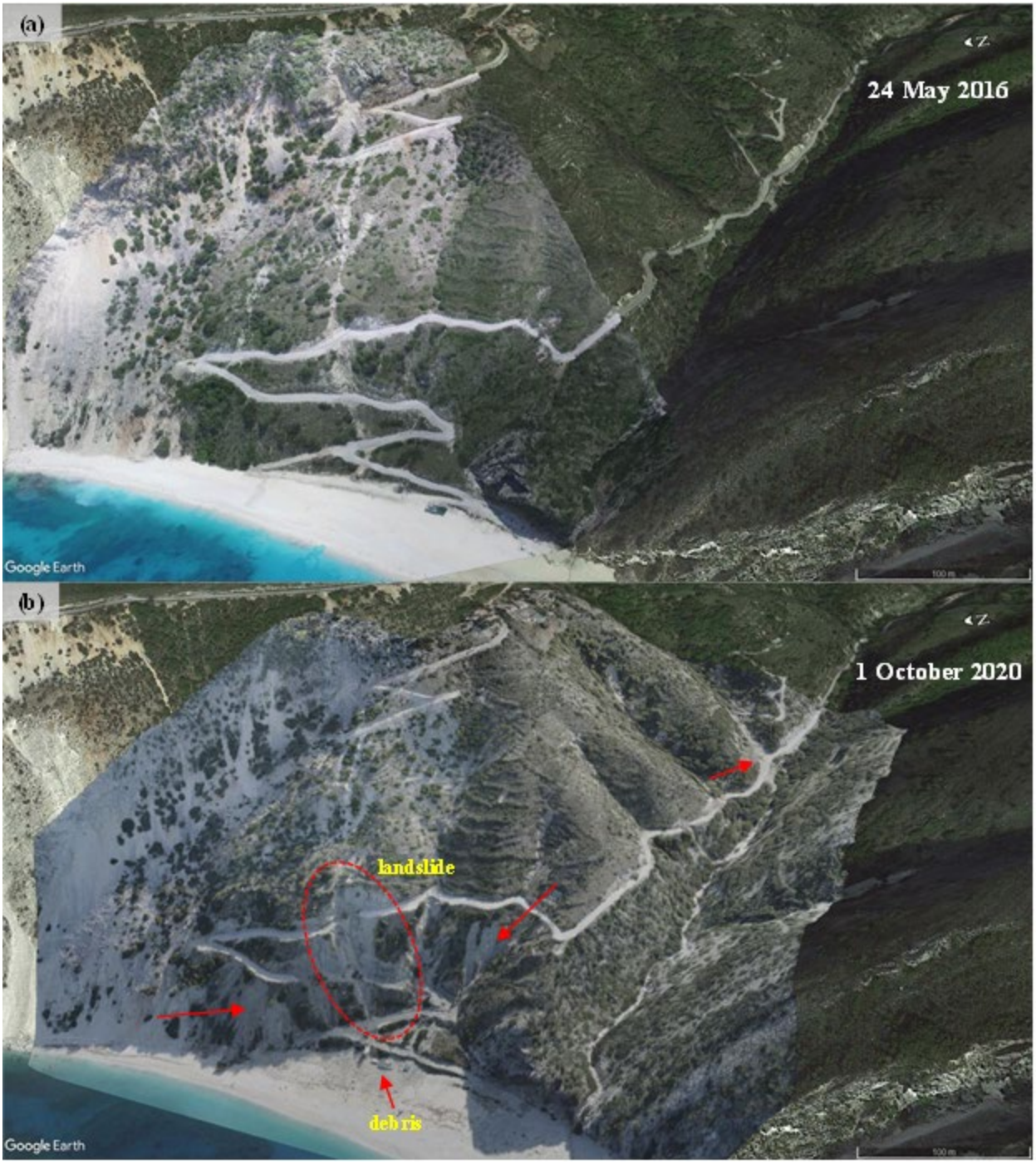

Figure 6.3. UAV-enabled mapping of Myrtos beach: a) Pre-event perspective view, and b) Post-event perspective view (view 3D model at: https://skfb.ly/6WyR6)

Figure 6.4. Evidence of mass movement along the steep western coastline of Lefkada island: a,b) 38.672194°N, 20.5629639°E, c) 38.67467°N, 20.55967°E

Figure 6.5. Evidence of fresh rockslide sediment and debris along the steep western coastline of Lefkada island (38.637676°N, 20.558488°E): a) pre-event photo, b) post-event photo.

6.2.2. Karditsa Region

In the region of Karditsa, complex landslides are mainly formed in the weathered material and produced by shale flysch and mixed type flysch (alternations of shales and sandstones). Their geometry is complex, as their upper and middle part is formed by rotational slumping or translational slides and the lower part is an earth slide or earth flow. They are relatively shallow, i.e., <3-5m, and sometimes partially follow the geometry of stronger underlying beds. The displaced material traveled at distances between 10 to 20 m and accumulated at the toe of the slide. Usually, the debris from this type of landslide has intercepted and completely covered roads, but the roads remained intact.

Figures 6.6 to 6.20 are characteristic examples of rotational slumps mainly formed in shale flysch, in conglomerates (flysch) and in weathered flysch. More specifically, the slope failure which occurred in location 41 (Figure 4.22) was formed in the weathered mantle of sandstone flysch (Figure 6.6). The complex sliding mechanism includes a rotational failure followed by an earth flow that has impacted the roadway. The slump is considered deep-seated with an estimated height and length of 30 and 50 m, respectively. Another example is the complex slope failure in location 50 (Figure 6.7) which consisted of one of the most extensive landslides that was detected during this expedition. Its height and length were calculated at 70 and 150 m, respectively. The landslide is relatively shallow (7-10 m deep) and is formed in two parts: 1) a rotational landslide at the upper part and 2) an earth flow at the lower part. This slope failure occurred in shale flysch. In Figure 6.20, another significant rotational slide in the weathered mantle of sandstone flysch was documented. The landslide resulted in the collapse of the road. The length and depth of the slide were 10 meters.

Moreover, landslides involving soil/earth material are formed in the weathered mantle of the flysch or in the shale dominant flysch. Their characteristic is that the slipped earth material has a long travel distance, up to 150 m. They have affected the road network in some places but in relatively narrow zones. Thus, the problems encountered due to earth flows are not very severe. Examples are presented in Figures 6.21 through 6.23. The maximum thickness of the accumulated debris material at the base of the slope was estimated at 3 meters while the width of the deposit area at 25 meters.

Figure 6.6. Complex slide (slump – earth flow) in mixed type flysch (39.3118220°N, 21.5960140°E)

Figure 6.7. Complex slide (rotational and earth slide) in shale dominant flysch. The slipped material has completely covered the road (39.2116910°N, 21.7942940°E)

Figure 6.8. Complex slide (slump – earth flow) (39.28353°N, 21.68537°E)

Figure 6.9. Rotational slide along the Argithea to Zervo village road (39.351111°N, 21.521389°)

Figure 6.10. Rotational slide that caused road damage next to Argithea village (39.356111°N, 21.535556°E).

Figure 6.11. Rotational slide in Eastern Argithea area (39.364444°N, 21.541111°E)

Figure 6.12. Rotational slide in Eastern Argithea area (39.363889°N, 21.538611°E).

Figure 6.13. Rotational slide on the road to Oxya village (39.366667°N, 21.592222°E)

Figure 6.14. Rotational slide at Argithea to Zervo road (39.351111°N, 21.521389°E).

Figure 6.15. Rotational slide on the road to Oxya village (39.36°N, 21.591944°E)

Figure 6.16. Rotational slide towards Porti village (39.425833°N, 21.665556°E)

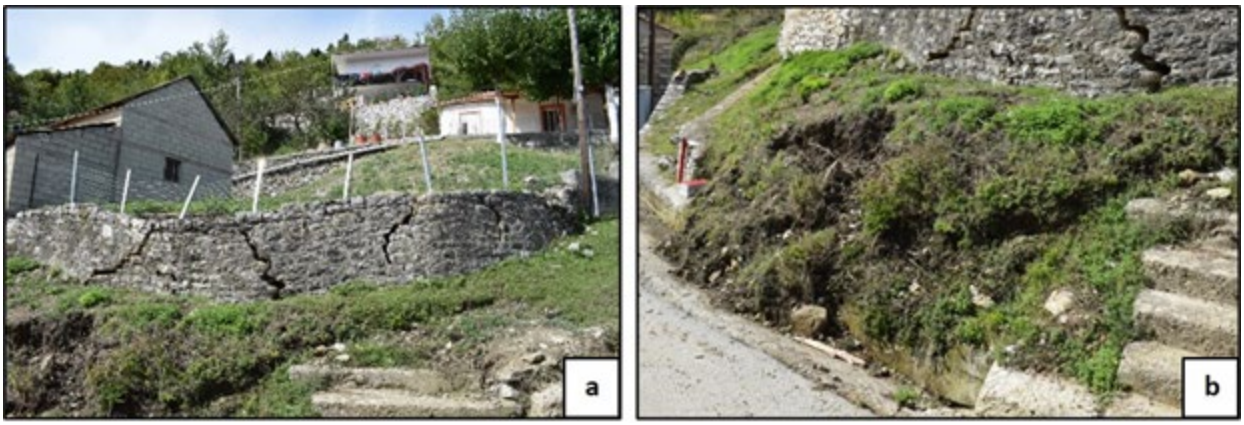

Figure 6.17. Rotational slide on the road to Oxya village that damaged a retaining wall (39.358889°N, 21.596111°E)

Figure 6.18. Rotational slide causing structural damage at the village of Rafina (39.27172°N, 21.69607° E)

Figure 6.19. Rotational slide inducing damage on the road network (39.28596°N, 21.69099° E)

Figure 6.20. Rotational slide in weathered mantle that caused damage to road (39.2174890°N, 21.7949870°E)

Figure 6.21. Earthflow in weathered mantle of shale flysch (39.3115490°N, 21.6142420°E)

Figure 6.22. Accumulated earth material at the road level (39.3115490°N, 21.6142420°E)

Figure 6.23. Accumulated earth material at the road level (39.28709°N, 21.69355°E)

6.3. Rockfalls, Rockslides and Structurally-Controlled Failures

6.3.1. Cephalonia and Lefkada Islands

A single rockfall was encountered along the road network, during the reconnaissance deployment to Cephalonia (Figure 6.24). The limestone rock wedge had a size of approximately 2m×1.5m×1.5m. Another rockfall example from Lefkada is shown in Figure 6.25. Moreover, the western coastline of Lefkada that had most recently experienced numerous landslides during the 2015 earthquake was affected by the precipitation with fresh rockslide sediment and debris found on the roads and at the beach (Figure 6.26).

Figure 6.24. Rockfall in Cephalonia island (38.36995197°N, 20.5684499722°E)

Figure 6.25. Rockfall in Lefkada island (38.616356°N, 20.57904167°E)

6.3.2. Karditsa Region

Rockfalls, rock slides and structurally-controlled failures were not often encountered in the region of Karditsa with the exception of areas where thick-bedded sandstone flysch or limestones exist. Examples of such failures are presented in Figures 6.26 through 6.35. A characteristic example is presented in Figure 6.35, where a planar failure of a massive limestone on thin-bedded limestone occurred. The maximum volume of the limestone blocks observed was 3 to 4 m^3.

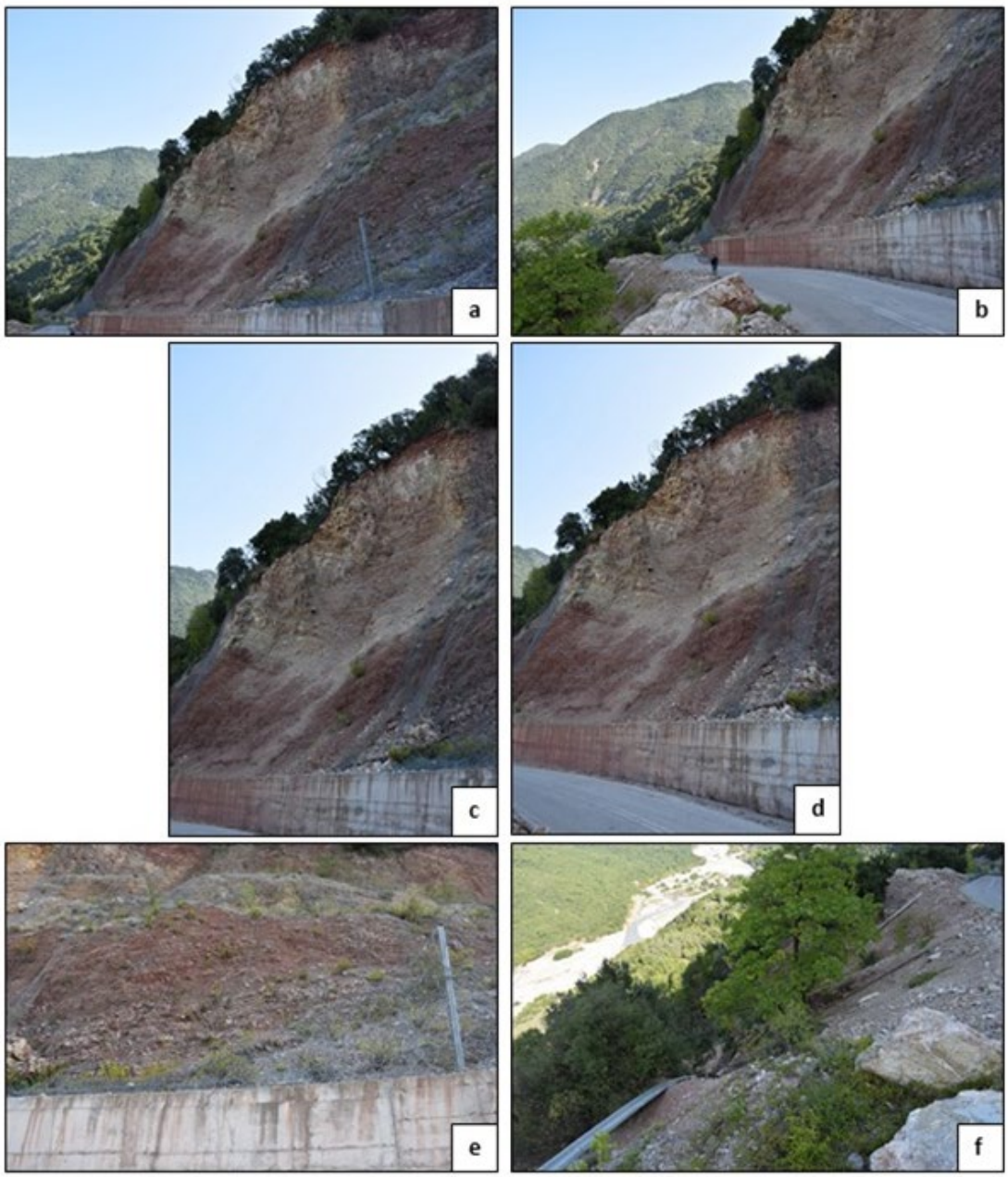

Figure 6.26. Rockfall failure at the area of Karpenisi - Agrafa

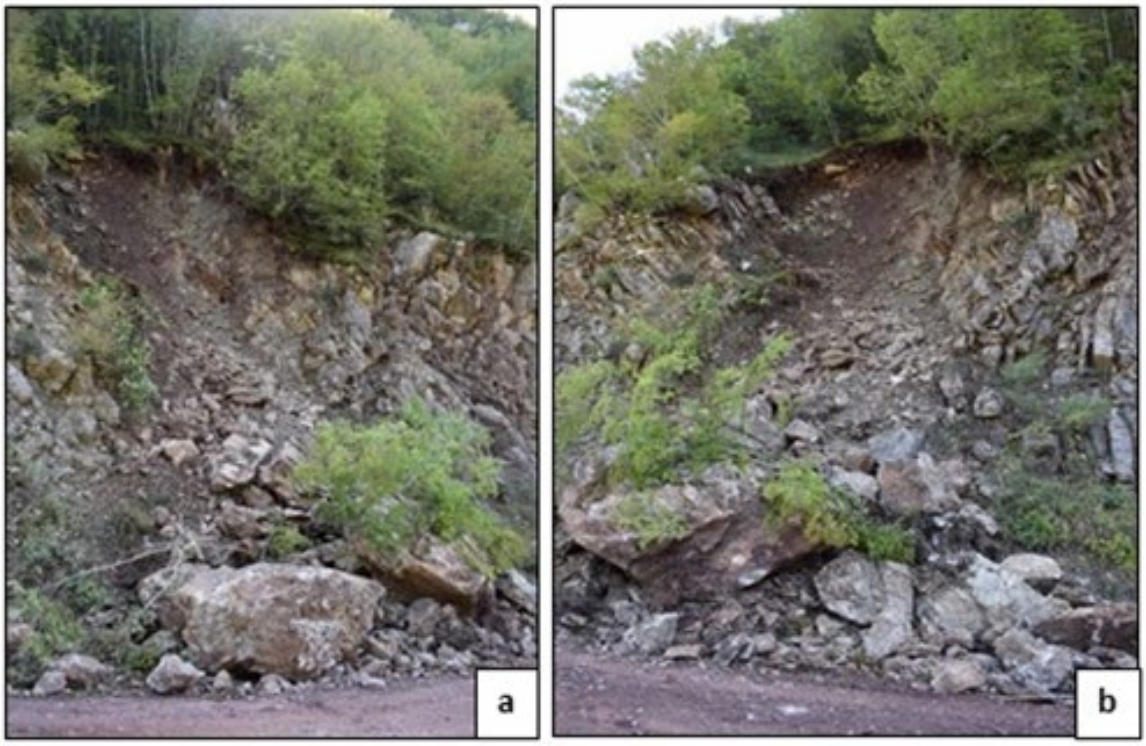

Figure 6.27. Rockslide failure at the area of Karpenisi - Vraggiana

Figure 6.28. Rockslide along the road network of Karpenisi - Vraggiana

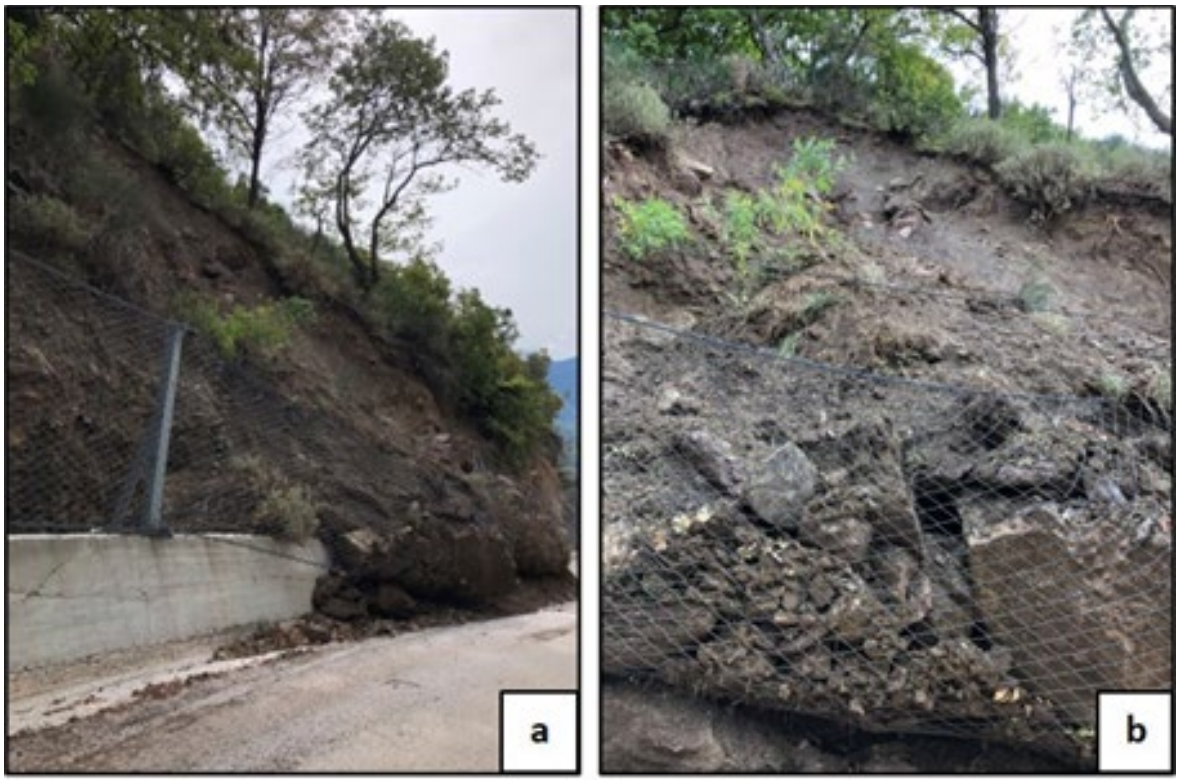

Figure 6.29. Rockslide towards Porti village (39.410556°N, 21.658611°E)

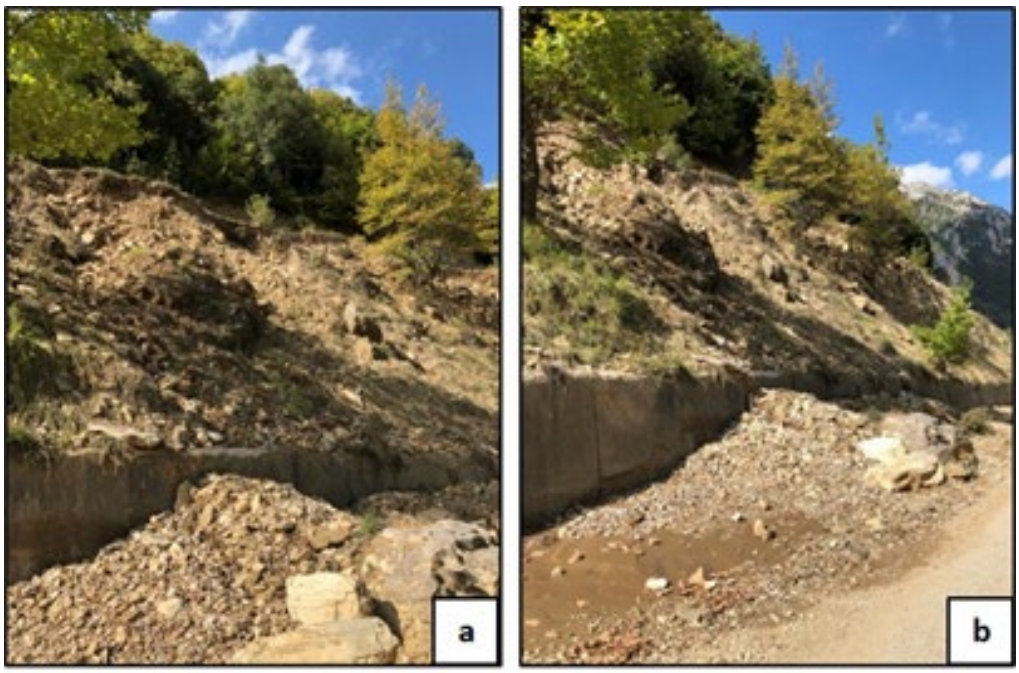

Figure 6.30. Rockslide along the road from Argithea to Zervo village road (39.3425°N, 21.514167°E)

Figure 6.31. Rockslide along the road from Argithea to Zervo village road (39.348333°N, 21.517222°E)

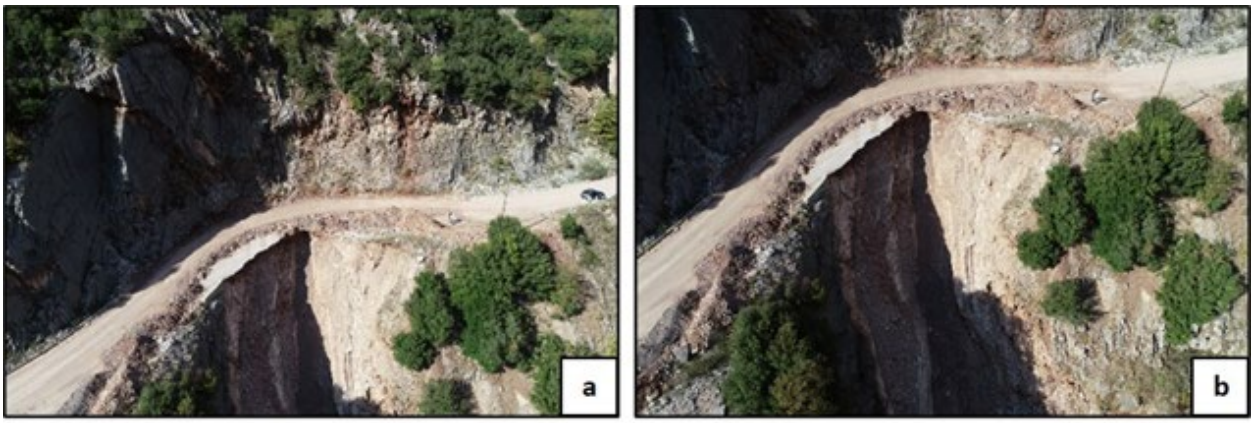

Figure 6.32. Rockslide along the Argithea to Zervo road network (39.354167°N, 21.5175°E).

Figure 6.33. Wedge failure mechanism at the area of Belokomiti. (39.25325°N, 21.72192°E)

Figure 6.34. Planar sliding at the village Pezoula. (39.30406°N, 21.69014°E)

Figure 6.35. Planar sliding and rockfalls in limestone rockmass. Road to Oxia. (39.3895330°N, 21.6145240°E)

6.4. Debris flows

6.4.1. Cephalonia Island

Across Cephalonia island, the reconnaissance team encountered numerous manifestations of debris flows that appeared to be the most common feature of the effect of Medicane Ianos. Debris, collected or still in place, was present along gullies and riverbeds (Figure 6.36), while in a few occasions, it directly affected rural communities resulting in significant infrastructure and property damage. Most notably, Assos village, situated in the north-west of the island (Figure 4.1), was severely impacted by a major debris flow. The debris traveled along a distance of approximately 1.5 km, burying the small rural community under ~1.5 m of earth material (Figures 6.37 and 6.38). No fatalities were reported, possibly due to the fact that the phenomenon occurred during the early morning hours, according to local residents (anecdotal). Boulder size in

Figure 6.36. Debris flow manifestations across Cephalonia island: a) 38.309422222°N, 20.570208333°E, b) 38.309383333°N, 20.570166667°E, c) 38.307786111°N, 20.495036111°E, d) 38.291980556°N, 20.528944444°E, e) 38.306109972°N, 20.534586972°E, f) 38.231639972°N, 20.506282972°E

Figure 6.37. Debris flow within the village of Assos (38.319506°N, 20.508197°E), as of 9/22/2020

Figure 6.38. Debris flow within the village of Assos (38.319506°N, 20.508197°E), as of 9/29/2020

the debris reached up to 40-50 cm. The source of the debris was traced to the hills east of the village (Figures 6.39 and 6.40), where significant surface erosion and ground cracking was observed (Figures 6.39a and 6.39d). At places, eroded zones reached several meters in width. Eroded limestone boulders and residual soil material were present along the entire path of the flow (Figures 6.39b and 6.39e). Moreover, the water utility line serving the Assos village community had failed at several locations due to ground cracking (Figure 6.39c). It is noteworthy that the community's water reservoir tanks are situated within the debris flow path (Figure 6.40), just downstream of the flow source area. UAV-enabled mapping of the entire area (Figures 6.40 and 6.41) indicates the change along the sea-shore due to material deposition. An initial, rough, estimation of the debris flow volume is 20,000m^3. Further analysis of the 3D model of the affected area will lead to a better quantification of the debris flow volume. A visualization of the 3D model of the debris flow in Assos can be seen here: https://skfb.ly/6WyTT.

Figure 6.39. Debris flow manifestations outside of Assos village (view 3D model at: https://skfb.ly/6WyTT): a) severe surface erosion and debris (38.376281°N, 20.548333°E); b) olive tree field covered by debris (38.378158°N, 20.543012°E); c) broken utility lines (38.37639166°N, 20.549125°E); d) extensive ground cracking (38.376112°N, 20.551870°E) and e) indicative debris extent and size (38.376112°N, 20.551870°E)

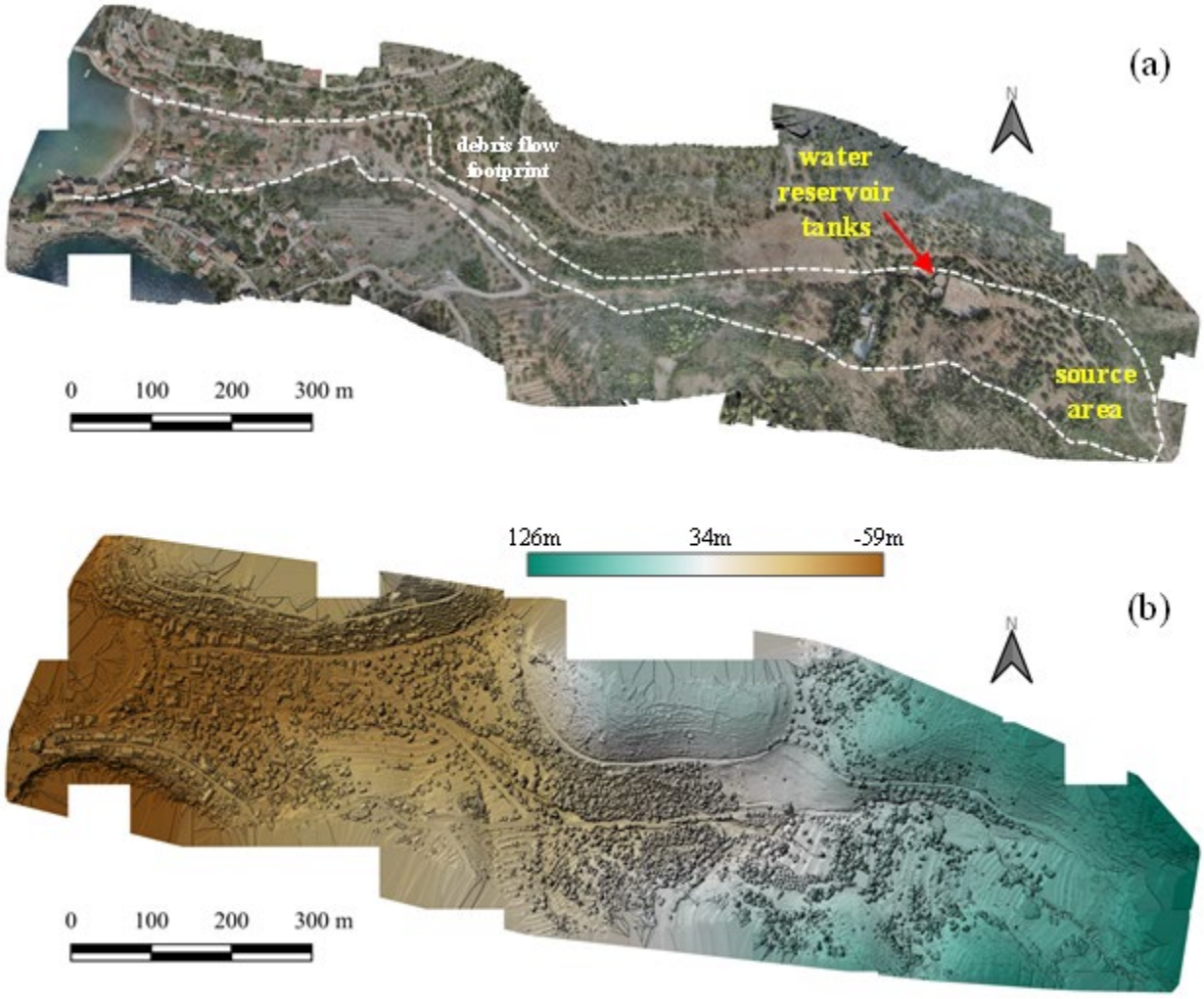

Figure 6.40. UAV-enabled mapping of Assos village and surrounding area (view 3D model at: https://skfb.ly/6WyTT): a) Orthophoto, and b) DSM, as of 09/30/2020.

Similar to Assos, just outside of the village of Fiskardo, which is situated at the north part of Erissos peninsula (Figure 4.1), a debris flow was documented and mapped. The phenomenon was less pronounced than the one encountered in Assos, but still significant, with the flow occurring along a distance of approximately 400 m. Moreover, despite the close proximity of the debris flow manifestation to the village, the community itself was not impacted by debris, but rather was inundated by flood water and mud (Figure 6.42). Significant erosion features were documented near the source of the flow (Figure 6.43). Eroded zones reached, at places, a depth of 2m. Aerial mapping of the flow (Figures 6.44 and 6.45) enables further analysis and can lead to the quantification of the debris flow volume. The debris flow is also visible in Sentinel-2 imagery as shown in the pre-and-post-event images (Figure 6.46). Similarly, Sentinel-2 pre-and-post event images of debris flows near Myrtos beach and the collapsed bridge at Agkonas village are shown in Figure 6.47.

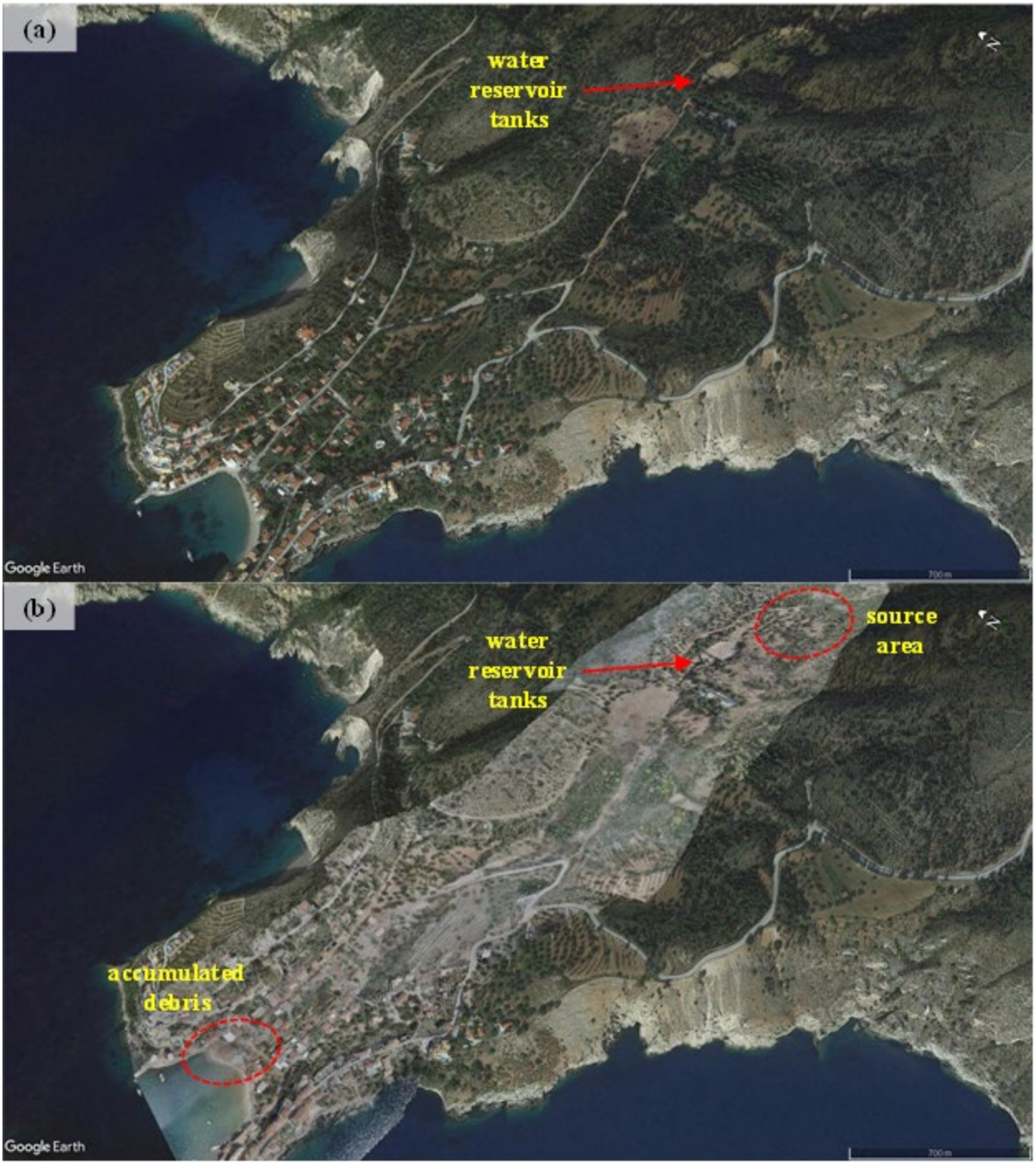

Figure 6.41. UAV-enabled mapping of Assos village and surrounding area (view 3D model at: https://skfb.ly/6WyTT): a) Pre-even perspective view, and b) Post-event perspective view

Figure 6.42. Footage snapshots of flooding within the village of Fiskardo during Medicane Ianos (source: https://www.youtube.com/watch?v=s_NUB3t4F_c)

Figure 6.43. Manifestation of debris flow outside of Fiskardo village: a) 38.459158972°N, 20.573128°E; b) 38.459304°N, 20.57232°E; c,d, and e) 38.459501°N, 20.57179499°E

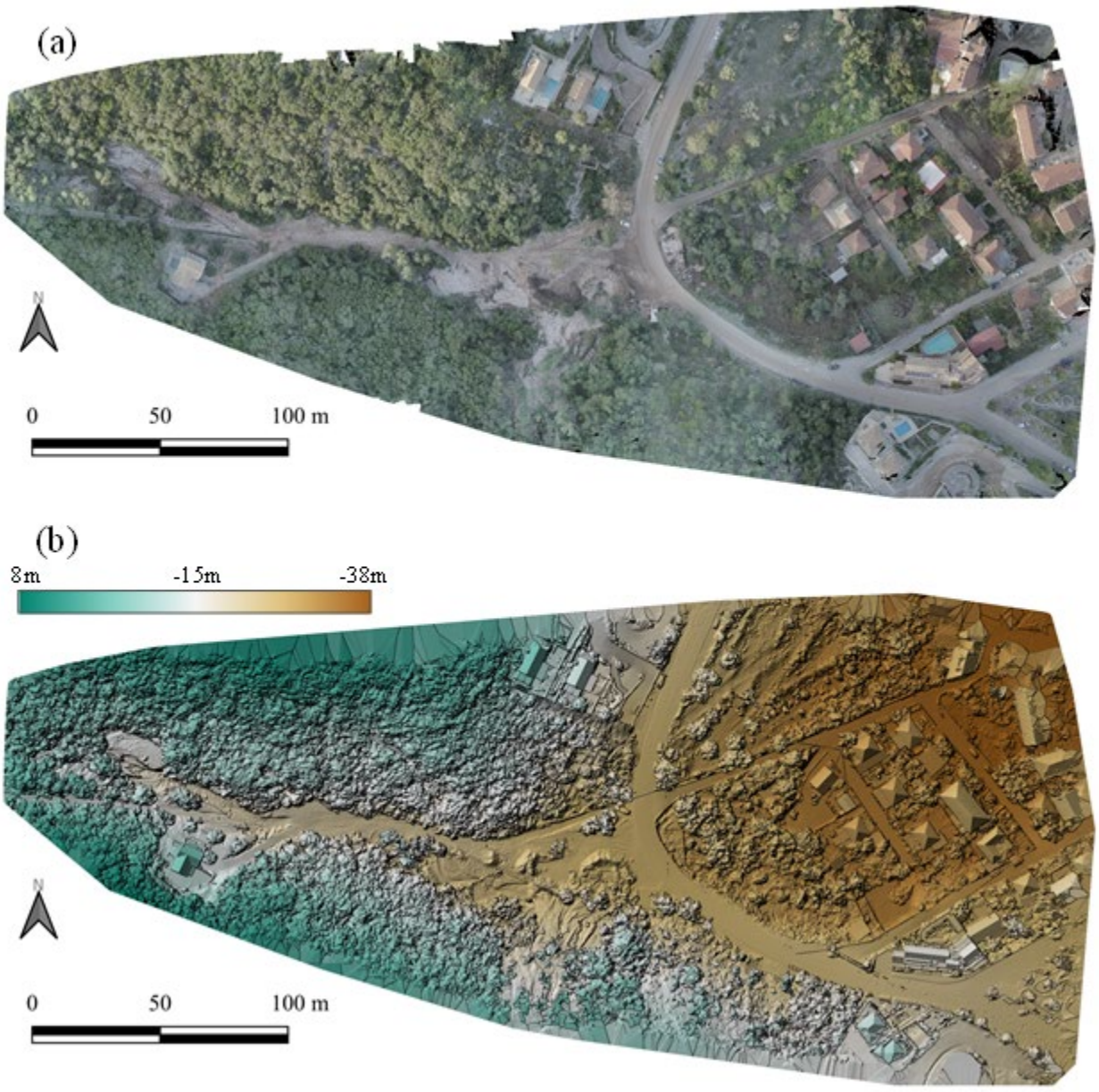

Figure 6.44. UAV-enabled mapping of debris flow outside of Fiskardo village: a) Orthophoto, and b) DSM, as of 09/29/2020

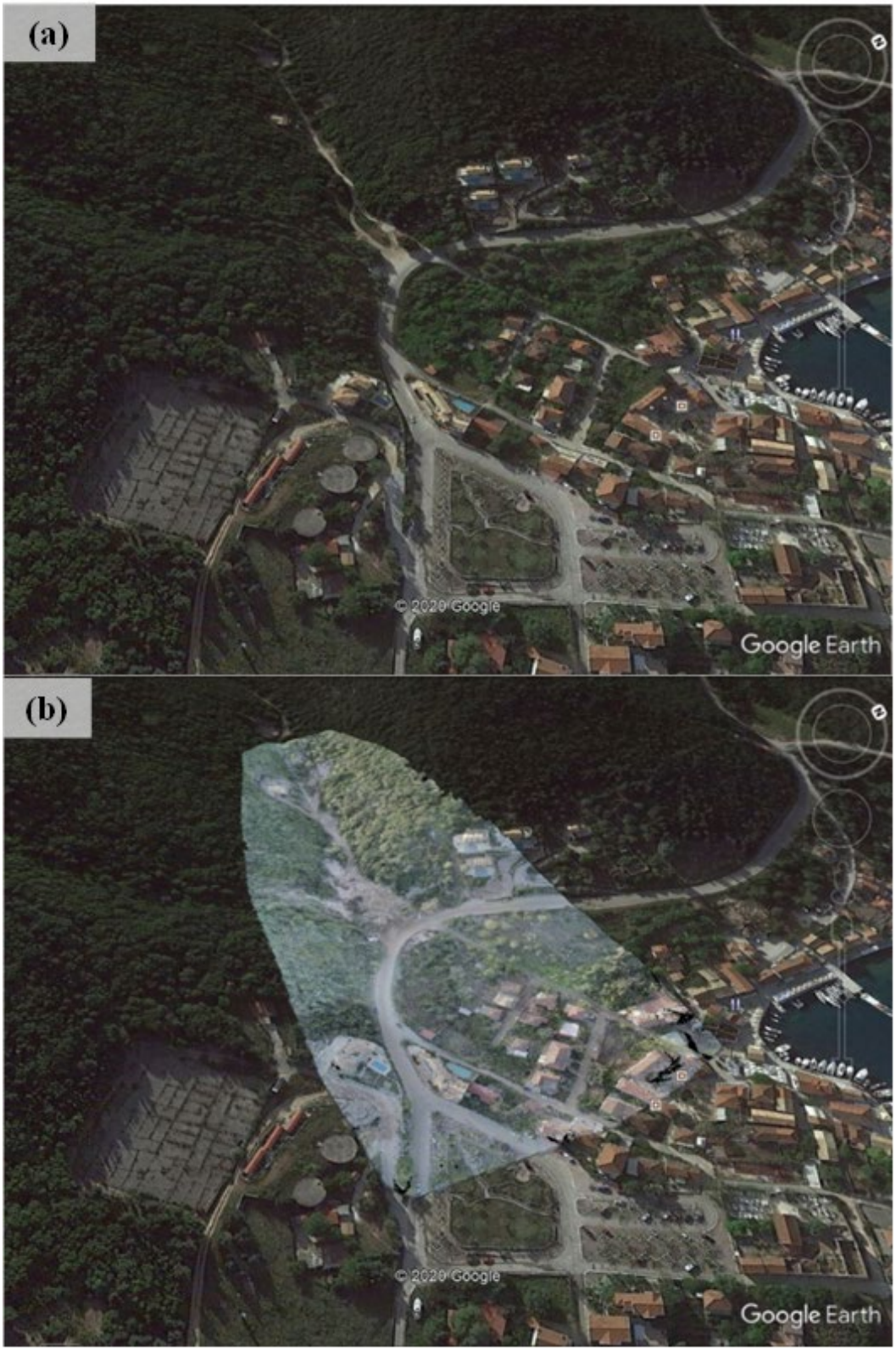

Figure 6.45. UAV-enabled mapping of debris flow outside of Fiskardo village: a) Pre-even perspective view, and b) Post-event perspective view

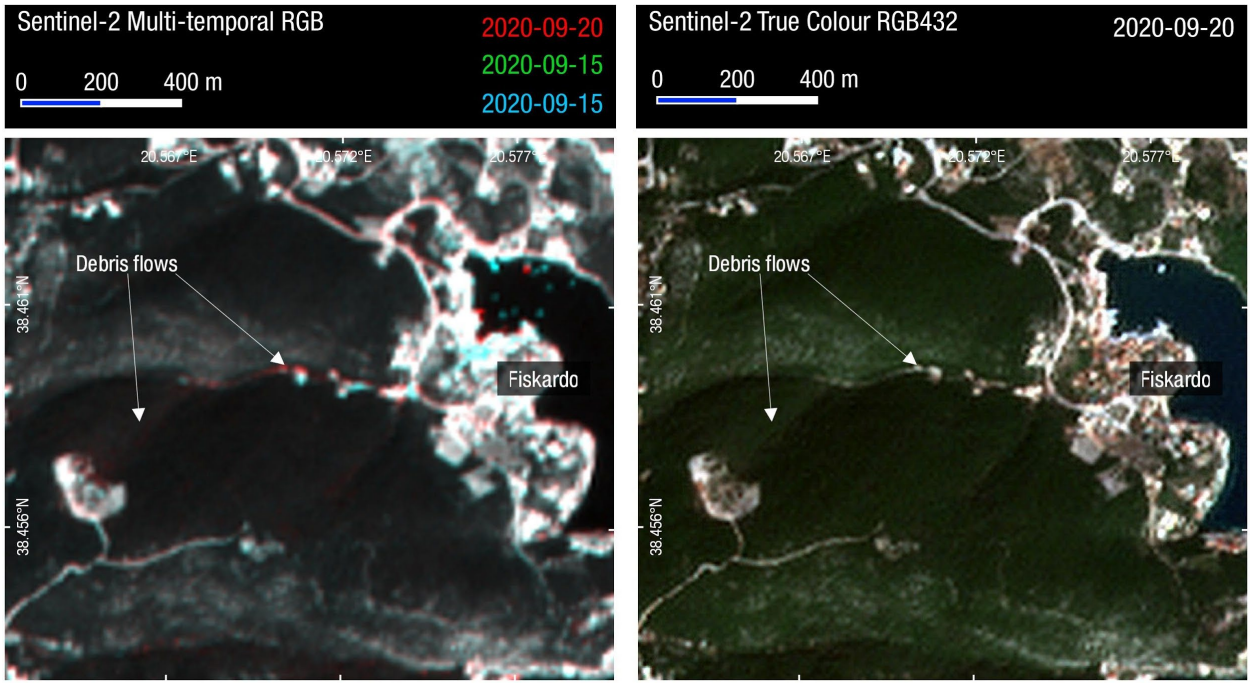

Figure 6.46. Sentinel-2 multi-temporal composite (Band 4) of Fiskardo, Cephalonia. Red colours mark the location of debris flows upstream of Fiskardo.

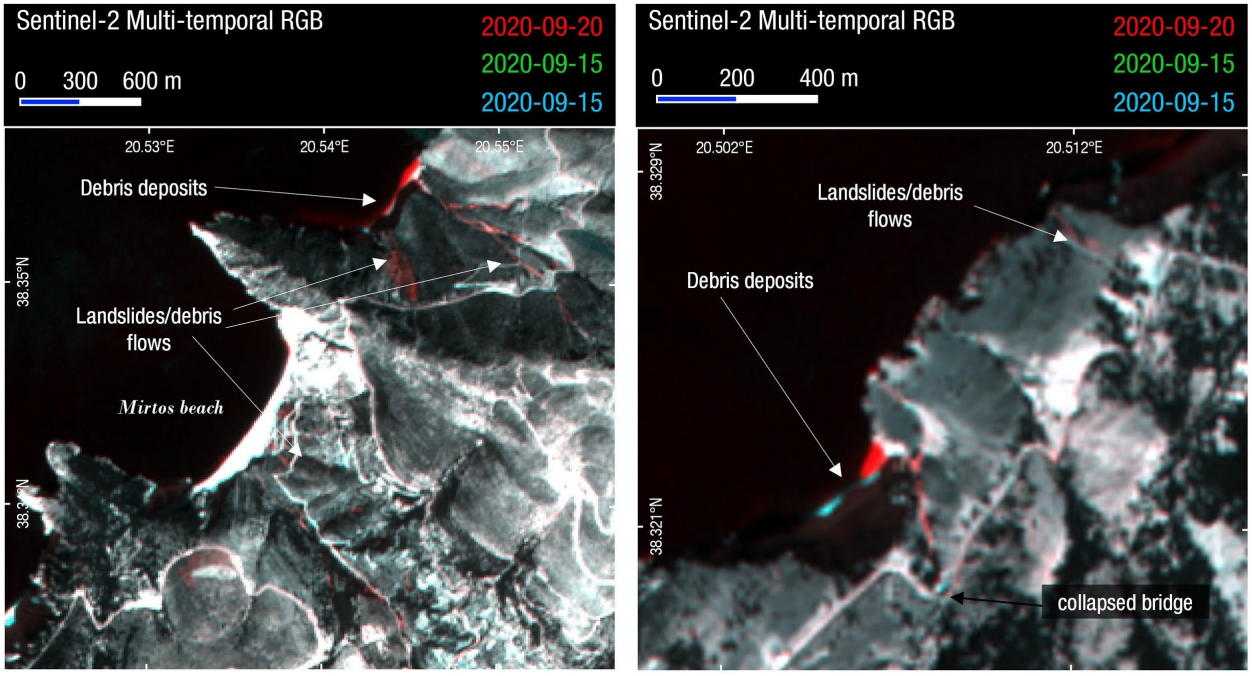

Figure 6.47. Sentinel-2 multi-temporal composite (Band 4) of Cephalonia. Left; Mirtos beach area, right; Site of collapsed bridge on the E.O. Argostoliou-Fiskardou (38.3195°N, 20.5081°E) Red colours mark the location of debris flows, landslides and deposition of debris along the coast.

6.4.2. Lamia Region

Evidence of debris flow was sparsely observed on creek riverbeds and gullies. The phenomenon was not as extensive as in Cephalonia island. When encountered, the average size of the debris reached up to 20-30cm.

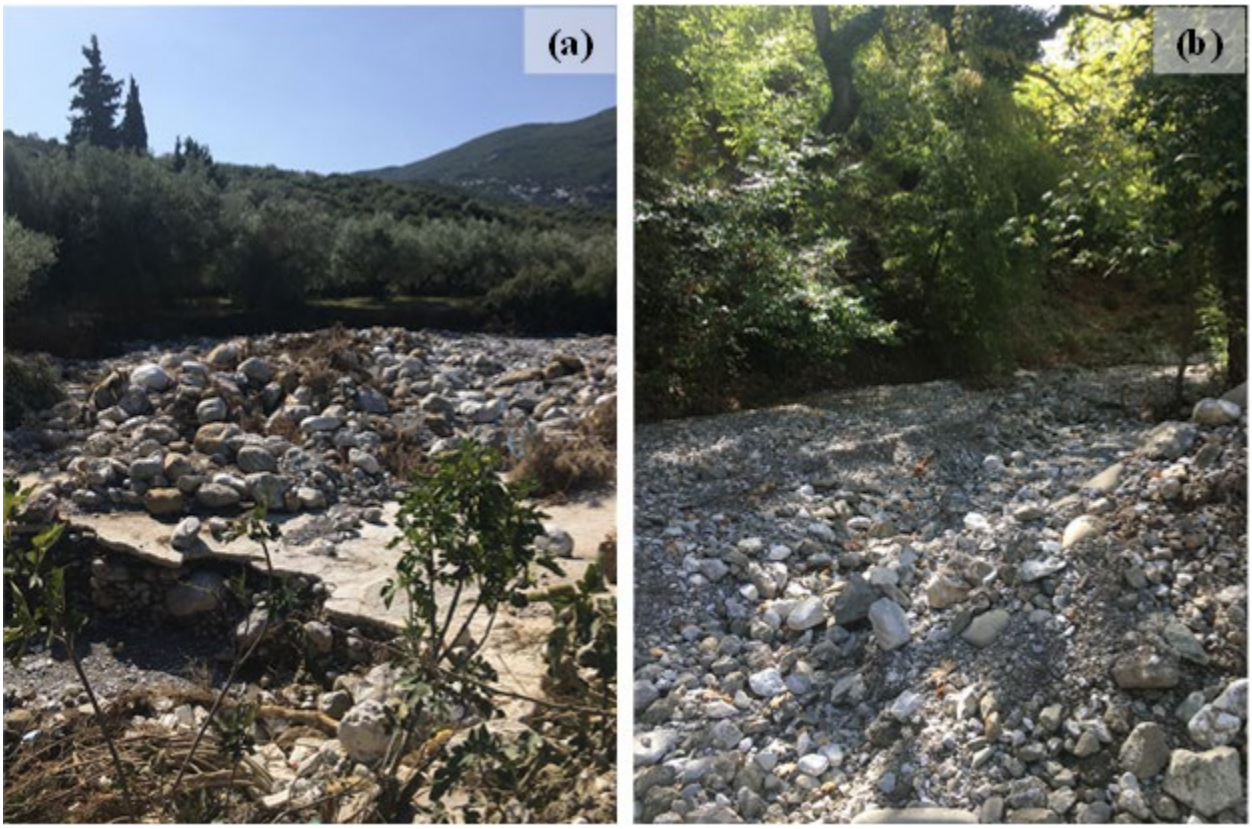

Figure 6.48. Manifestations of debris flow in the south side of Spercheios river valley: a) 38.85976388°N, 22.36969722°E; b) 38.874°N, 22.2538055°E

6.4.3. Karditsa Region

Debris flows were encountered in areas where the upslope area is characterized by fractured limestone, mixed flysch type or the conglomerate flysch.

The phenomena of accumulation of debris or earth materials in the gullies are mainly encountered in the area between Pefkofito – Vlassi – Livadia. Generally, this area has steep morphology and the gullies have transported extensive amounts of debris or earth materials from higher elevations.

An example from Livadia is shown in Figure 6.49. The thickness of the accumulated debris material at the base of the slope was up to 5 meters while the width of the deposit area was about 300 meters. Additional examples are shown in Figure 6.50 to 6.57.

Figure 6.49. Debris flow at Livadia. (39.3036610°N, 21.6068020°E)

Figure 6.50. Debris flow in gully at Pefkofito area. (39.3296110°N, 21.6094720°E)

Figure 6.51. Debris flow intercepting a road at the entrance of village Vraggiana

Figure 6.52. Debris flow along the road network of Karpenisi - Agrafa

Figure 6.53. Complete destruction of Argithea village due to a debris flow. Structural damage on infrastructure has been observed (39.359444°N, 21.538056°E).

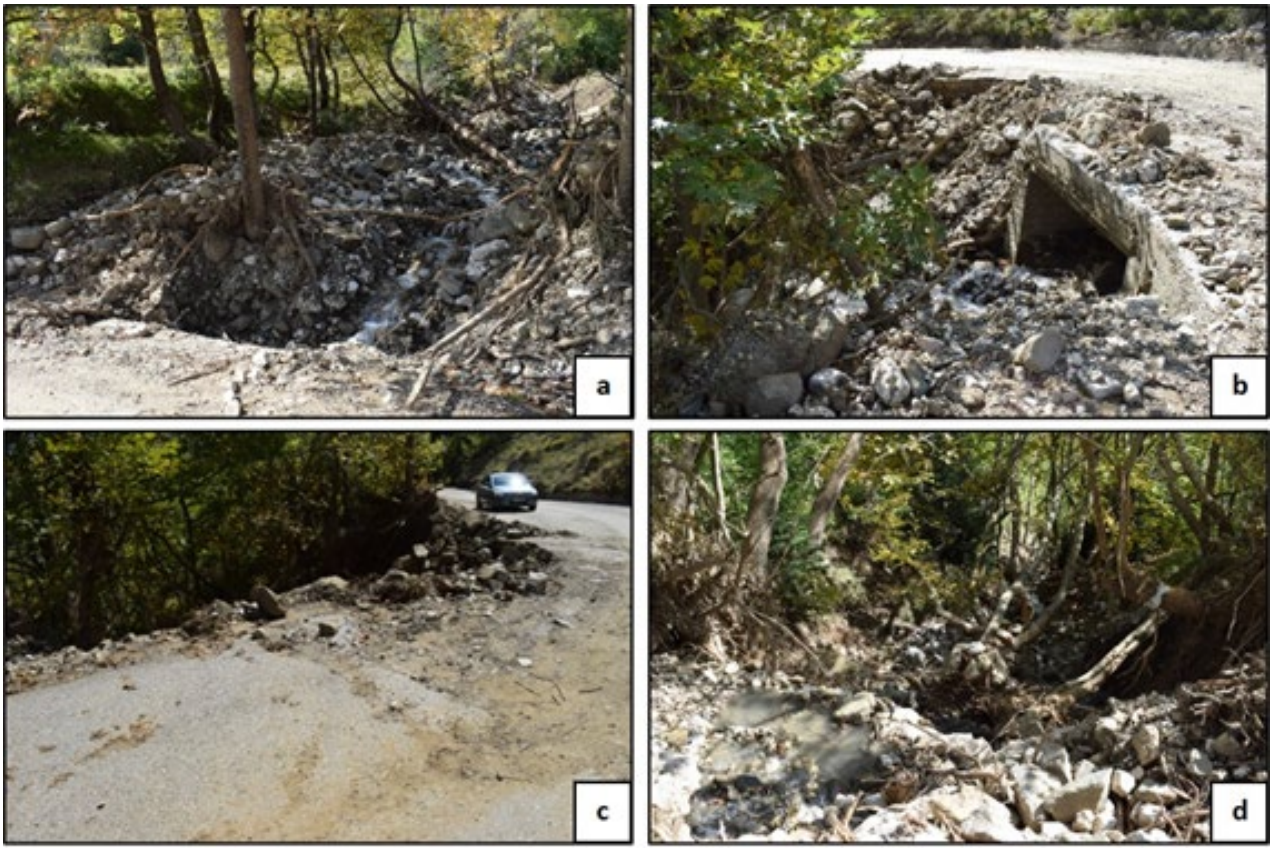

Figure 6.54. Debris flow towards Oxya village (39.366667°N, 21.592222°E).

Figure 6.55. Debris flow at the entrance of village Rafina. (39.27220°N, 21.69772°E).

Figure 6.56. Debris flow that intercepted twice the road leading to Agrafa Ski Center, above Plastira Lake: (1) 39.28118°N, 21.67614°E; (2) 39.28013°N, 21.6750°E.

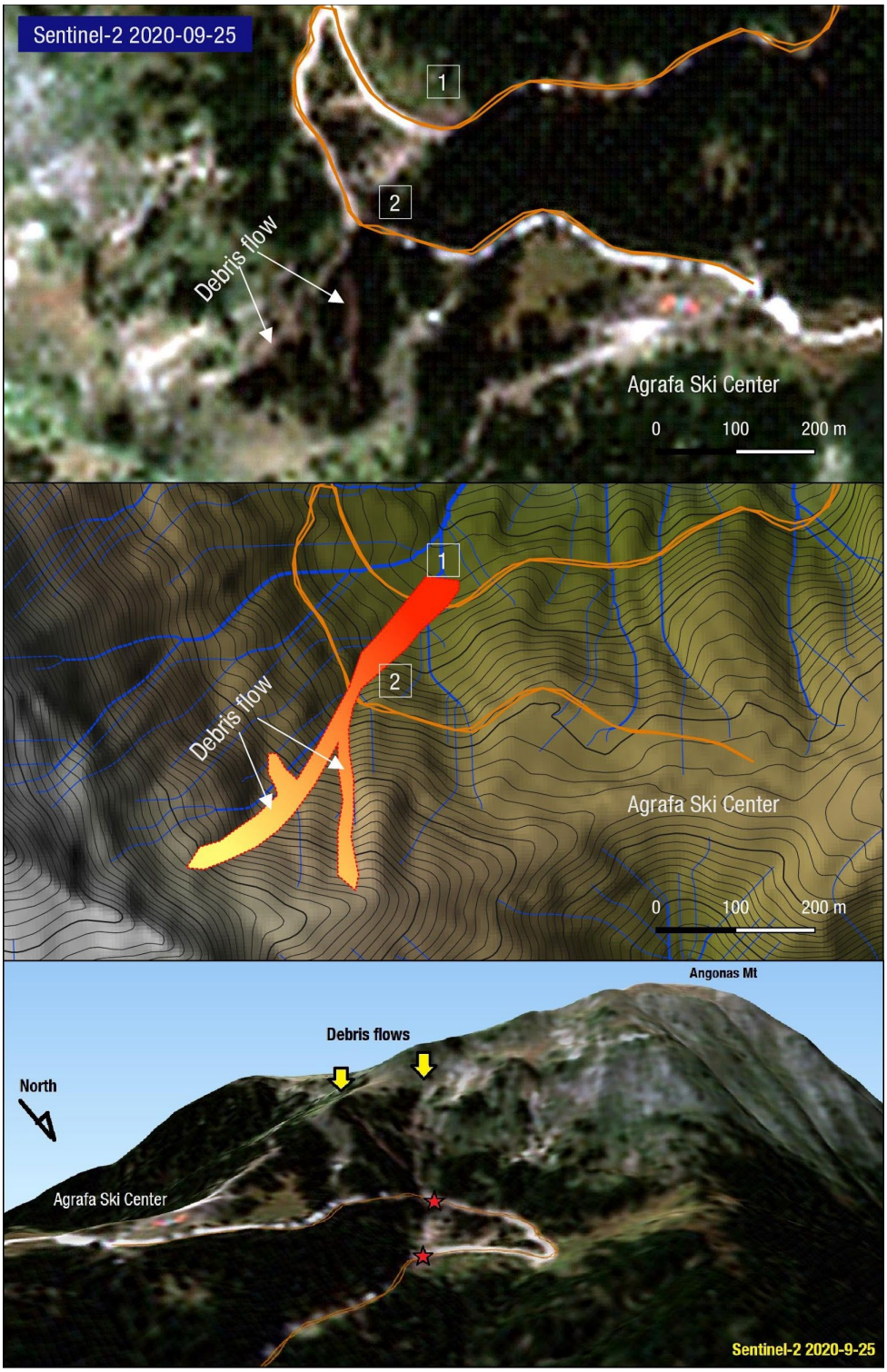

Figure 6.57. Debris flow that intercepted twice the road leading to Agrafa Ski Center, Plastira Lake. Above; Sentinel-2 (super-resolution) satellite imagery acquired on September 25. Middle; Relief map showing the debris flow complex. Contour interval is 5 m. Bottom; 3D view of Sentinel-2 image (September 25). (1) & (2) mark the locations of photos shown in the previous figure.

6.6. Karditsa Landslide Cluster Mapping with Satellite Imagery

While a large number of landslides and rockfalls occurred in the areas hit by Medicane Ianos, those were either isolated or mostly limited to the transportation network. The largest clusters and severe mass wasting phenomena occurred on Cephalonia island and especially on the mountainous area of Karditsa, as described earlier. To investigate and map the distribution of landslides in the Karditsa area, we used post-event acquisitions of optical Sentinel-2 satellite imagery. Copernicus Sentinel-2A/B multispectral imagery has a ground resolution of 10-20m and covers wide swaths, thus enabling the rapid imaging of the affected area.

We used multiple Sentinel-2 acquisition, dated September 20, 25 and 30 2020, as large parts were not visible due to cloud cover. Images before the event, dated September 5, 10 and 15 2020, were used as reference in order to visually identify landslides (Figure 6.58). Size of landslides mapped was limited to the satellite imagery resolution (10m), so smaller slides or rock falls were not included. Due to the small size of the majority of the landslides identified (most having a size of 2-4 pixels in Sentinel-2 imagery) few polygon landslide features were included. Landslide digitizing was focused on placing a point on the center of the landslide feature or at the starting point for linear distributions (long avalanches or earthflows).

For assistance in the manual picking of landslides, we used additional analysis products, such as change analysis rasters (normalized difference or MAD) and multitemporal single band RGB images (Figure 6.59). As the number of landslides is expected to be rather conservative due to the limits of Sentinel-2 imagery (resolution of 10 m), we plan to prepare a more detailed inventory using very high resolution imagery (3 meters or less).

This preliminary inventory (Figure 6.58) includes more than 1400 landslides, that are limited in a narrow mountainous area of Karditsa and part of Evritania regions. The largest concentration of landslides is around Amarantos settlement, south-east of Plastira lake, with more than 10 landslides per square kilometer.

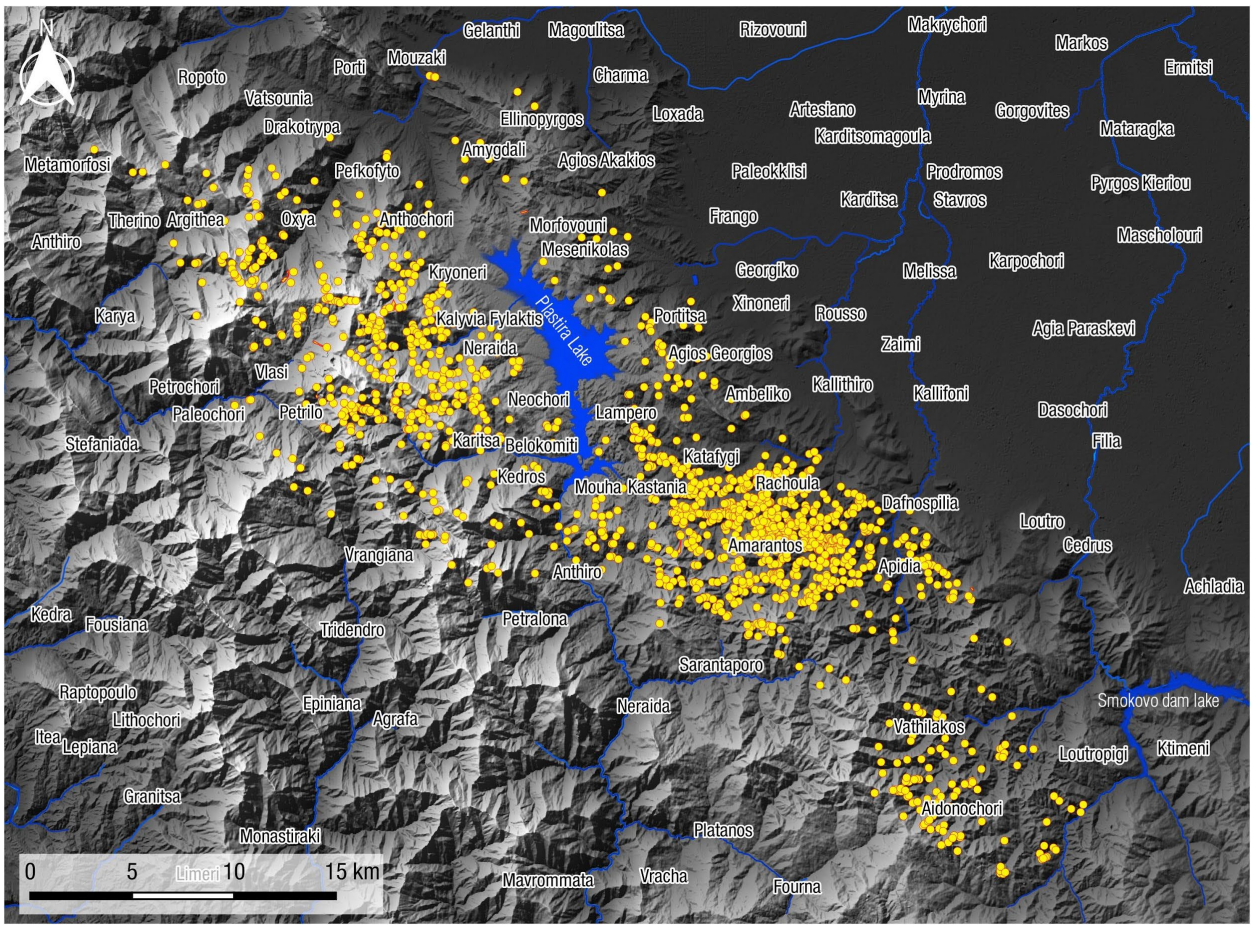

Figure 6.58. Overview of landslides mapped in Agrafa, Karditsa area, using Sentinel-2 optical imagery.

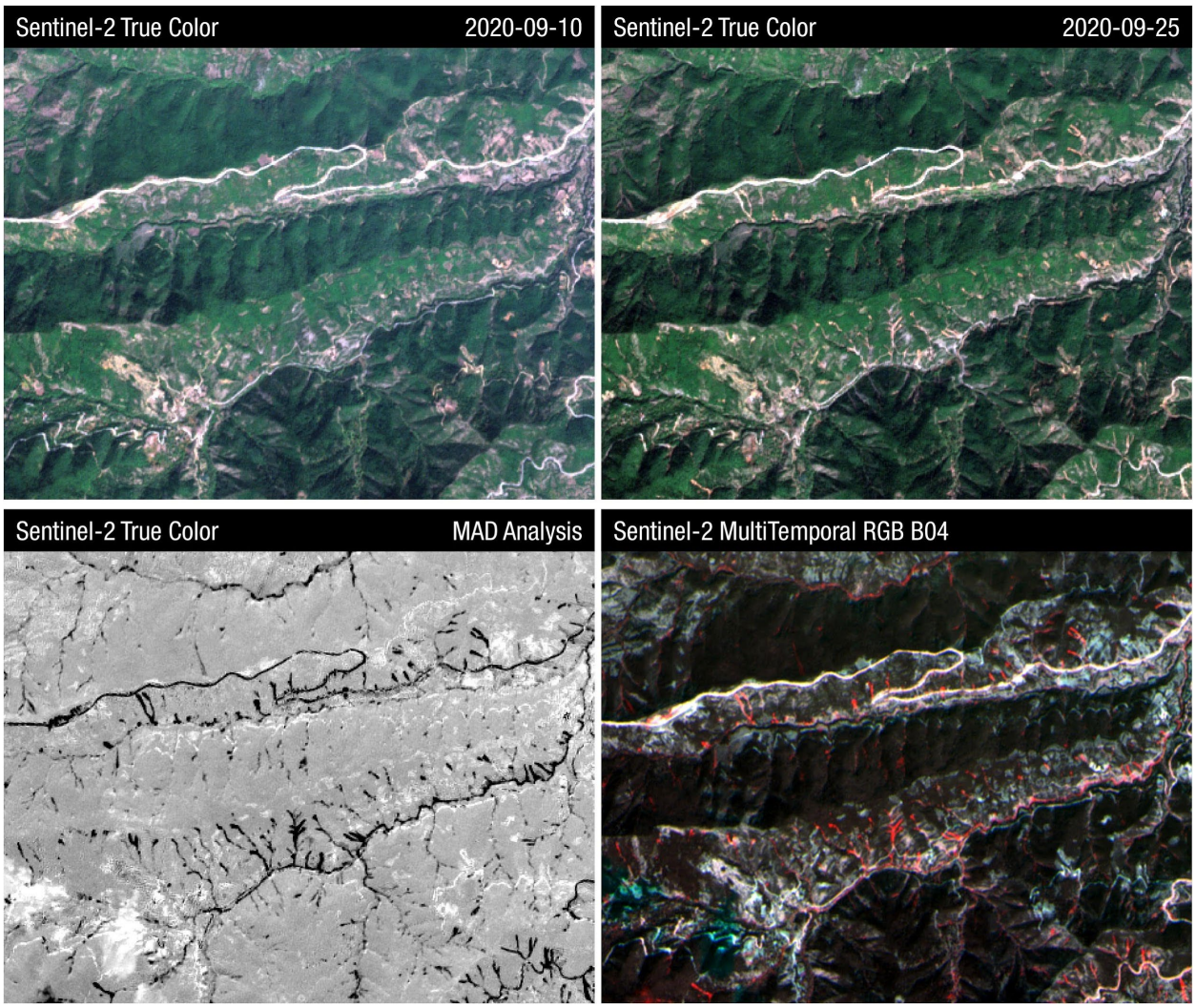

Figure 6.59. Example of Sentinel-2 optical imagery (top) and processing for assisting visual identification of landslides, used in mapping the preliminary landslide inventory.

7. Surface, Riverbank and Embankment Erosion and Scour

7.1. Cephalonia and Lefkada Islands

The reconnaissance team found that surface and riverbank erosion and scour was extensive in Cephalonia. The most notable cases were the surface erosion documented outside of the villages of Fiskardo and Assos (Figure 7.1 and 7.2, respectively). In both areas, residual soil and conglomerates were washed away exposing the bedrock formation (Figures 7.1 and 7.2c). The depth of the erosion reached, at places, up to 2 m (Figure 7.1). The eroded material contributed significantly to the debris/earth flows that impacted the nearby communities.

Figure 7.1. Surface erosion outside of Fiskardo village (38.459501°N, 20.57179499°E)

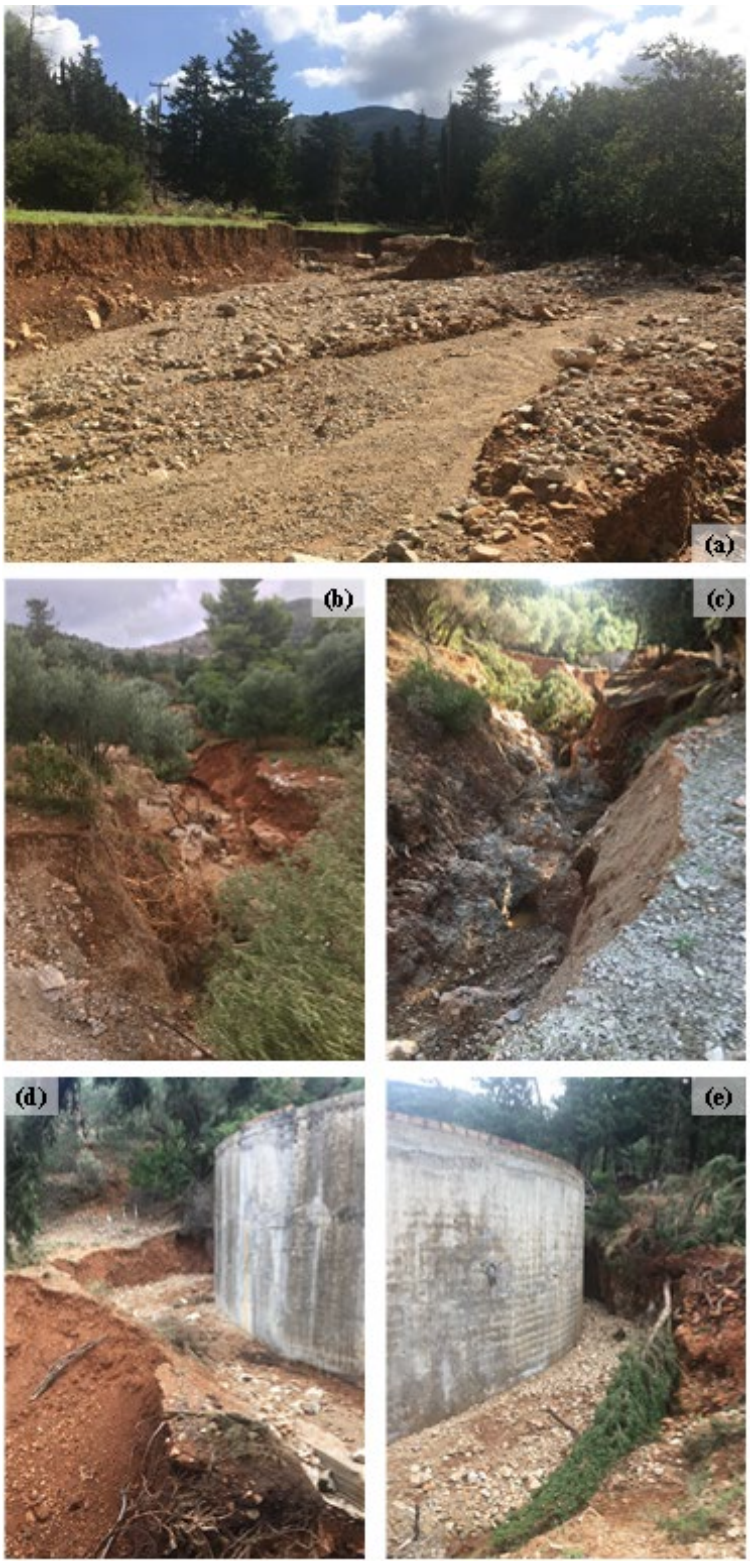

Figure 7.2. Surface erosion outside of Assos village, Cephalonia: a) 38.377188°N, 20.5445722°E; b) 38.3753611°N, 20.5463055°E; c) 38.374833°N, 20.5452722°E, d,e) 38.37619722°N, 20.5511166°E

On the island of Lefkada, extensive flooding within the lowlands of Vassiliki valley was reported. Based on photographs taken by eyewitnesses during the flood, the water level within parts of the town of Vassiliki seems to have risen by roughly 0.5 m (Figure 7.3).

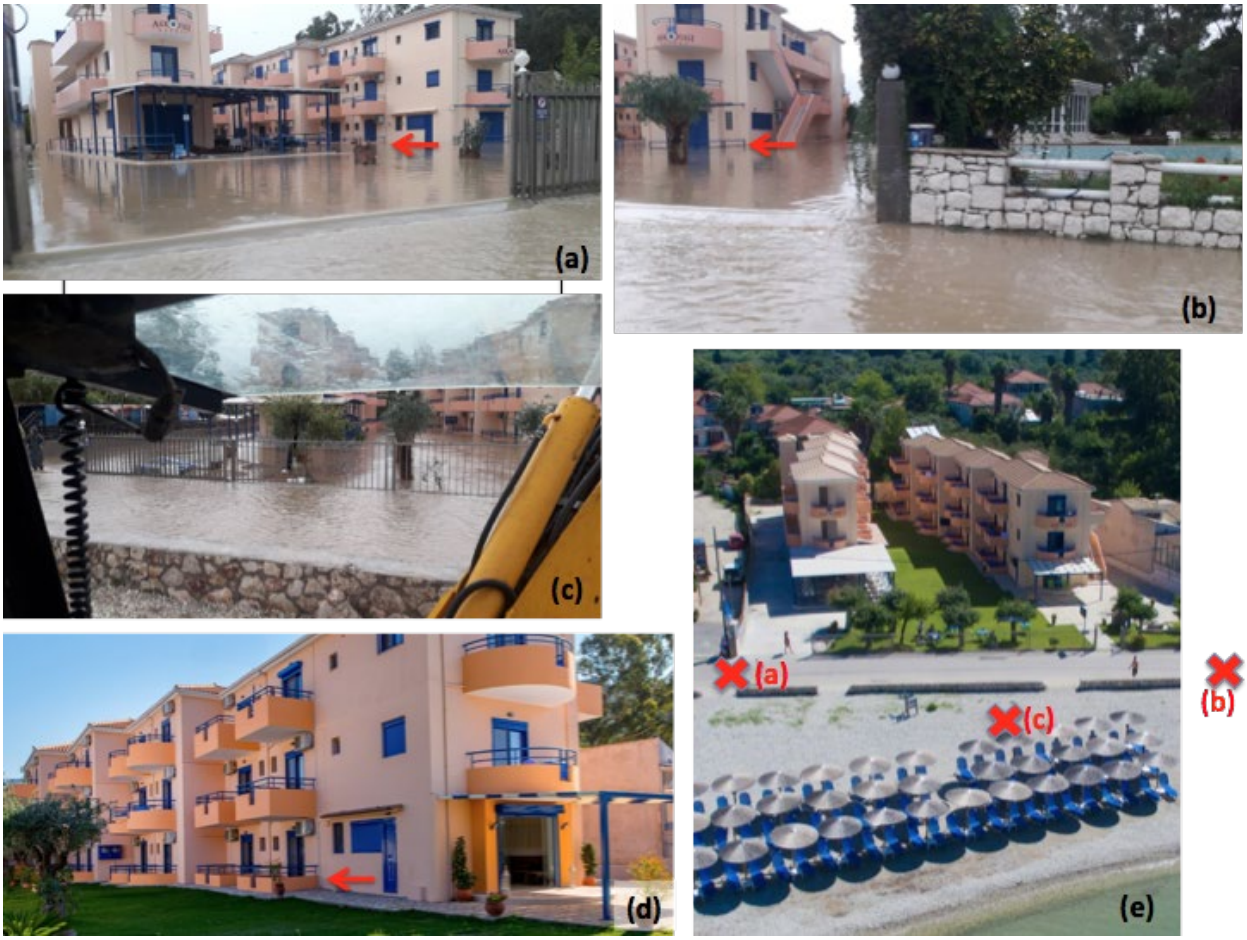

Figure 7.3. a,b,c) Flooding along the seaside at Vasiliki village, Lefkada, as photographed by an eye witness on the day vs. d,e) reference photos from GoogleMaps, indicating the view points for photos in a,b,c. Horizontal arrows indicate water level with respect to balcony railings (38.628758°N, 20.606678°E).

Evidence of erosion was found only in a few locations, namely in the vicinity of the river that empties into the seaside village of Vassiliki (Figure 7.4). Gabions and soil material comprising a small flood-protection levee were washed away (Figure 7.4a), road scour was observed along the river bank (Figure 7.4b), while riverbank erosion was documented (Figure 7.4c). In Figure 7.5, the evidence shows that the river overflowed (a), breaking fences and small walls (c), and depositing debris/earth material in the rural road as well as in orchards (b). Finally, near the mouth of the river, locals claim that the shoreline receded due to the deposition of debris. Figure 7.6 shows a panoramic photo taken from a standpoint which, according to GoogleEarth, used to lie in shallow water; hence, the shore used to be at the edge of what now looks like a lagoon.

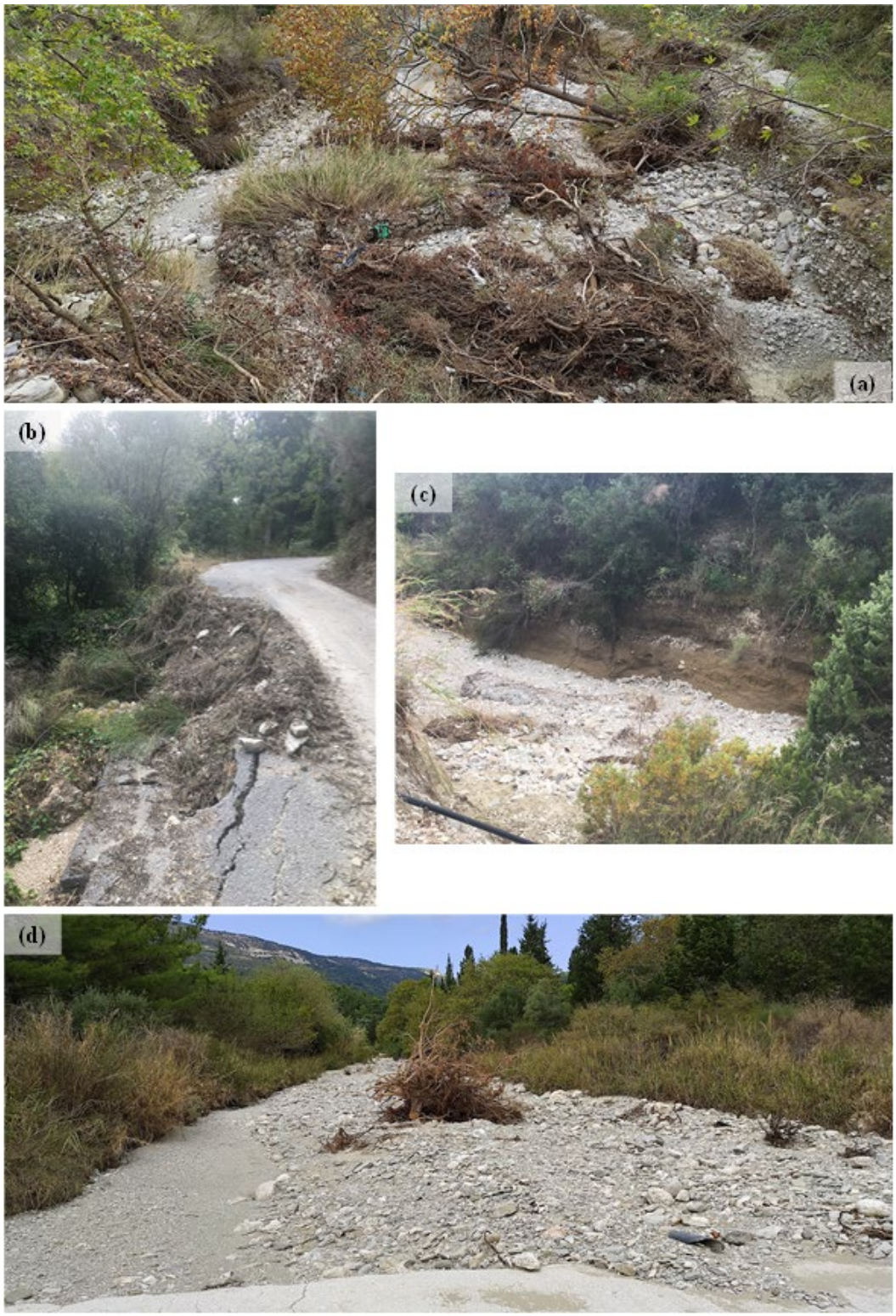

Figure 7.4. Typical features observed in Lefkada island: a) eroded material from flood protection levee (38.665858972°N, 20.620208°E); b) road embankment damage (38.67684167°N, 20.6093056°E); c) riverbank erosion (38.6646278°N, 20.623711°E); d) debris on riverbed (38.665858972°N, 20.620208°E).

Figure 7.5. Location of severe flooding (1 m from ground level) outside of Vasiliki village, Lefkada (38.637388°N, 20.617512°E).

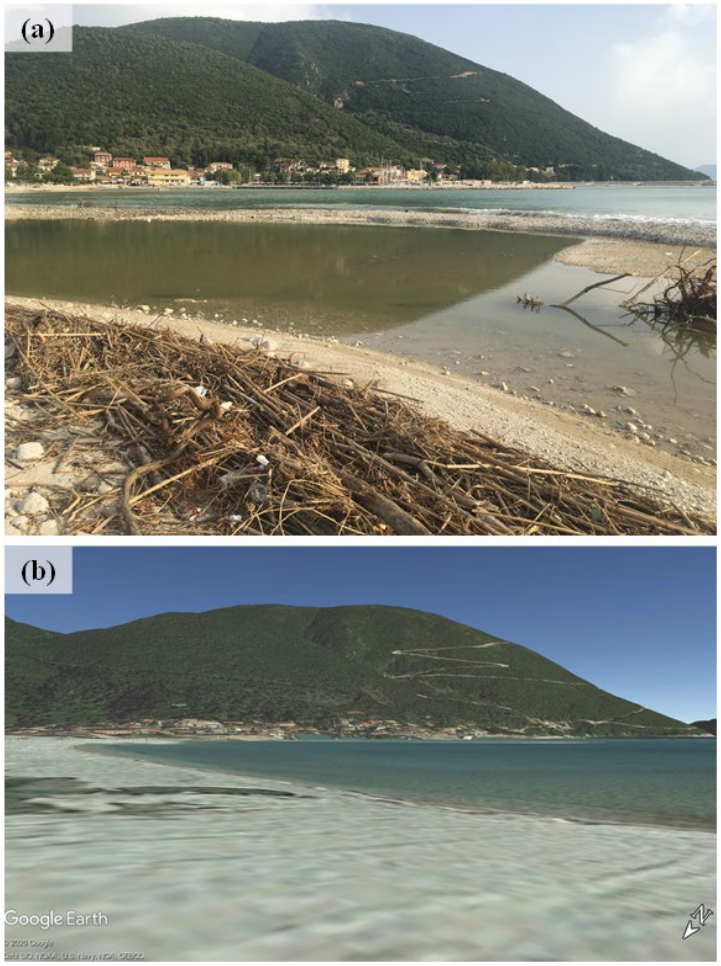

Figure 7.6. a) Photo from Vasiliki beach (38.629816°N, 20.603735°E), showing that the shoreline has receded due to debris deposited by the river. (b) Location the photo was taken from appears to be in shallow water according to Google Earth street view, corroborating this.

7.2. Lamia Region

Even more pronounced than in Cephalonia, riverbank erosion was observed along the Spercheios river valley (Figure 7.7). Extensive erosion or even collapse of the riverbank resulted in road failures (Figures 7.7a, 7.7c, and 7.7e), and to the partial compromise of the Wastewater Treatment facility of the town of Lianokladi (Figure 7.7d). Moreover, evidence of erosional features was observed on several embankments of the, partly under construction, highway E65 (Figure 7.8). These features were also identified via the analyses of pre- and post-event satellite imagery (Figures 7.9 and 7.10). At the time of the visit (25 September 2020) remediation measures were already underway and the deployment teams did not have access to the construction sites. Therefore, a more detailed documentation was not feasible. Nonetheless, on 30 October 2020, UAV-enabled mapping of the embankments and bridge on Highway E65, at km+56 outside of the town of Anavra (Figure 7.11), was performed. A visualization of the 3D model of the are can be seen here: https://skfb.ly/6W7AK.

Figure 7.7. Riverbank erosion in Spercheios river valley: a and b) 38.94233611°N, 22.21619722°E; c) 38.83451944°N, 22.39527499°E; d) 38.90973611°N, 22.28436944°E; e) 38.92455°N, 22.27771944°E; f) 38.946288833°N, 22.270412388°E.

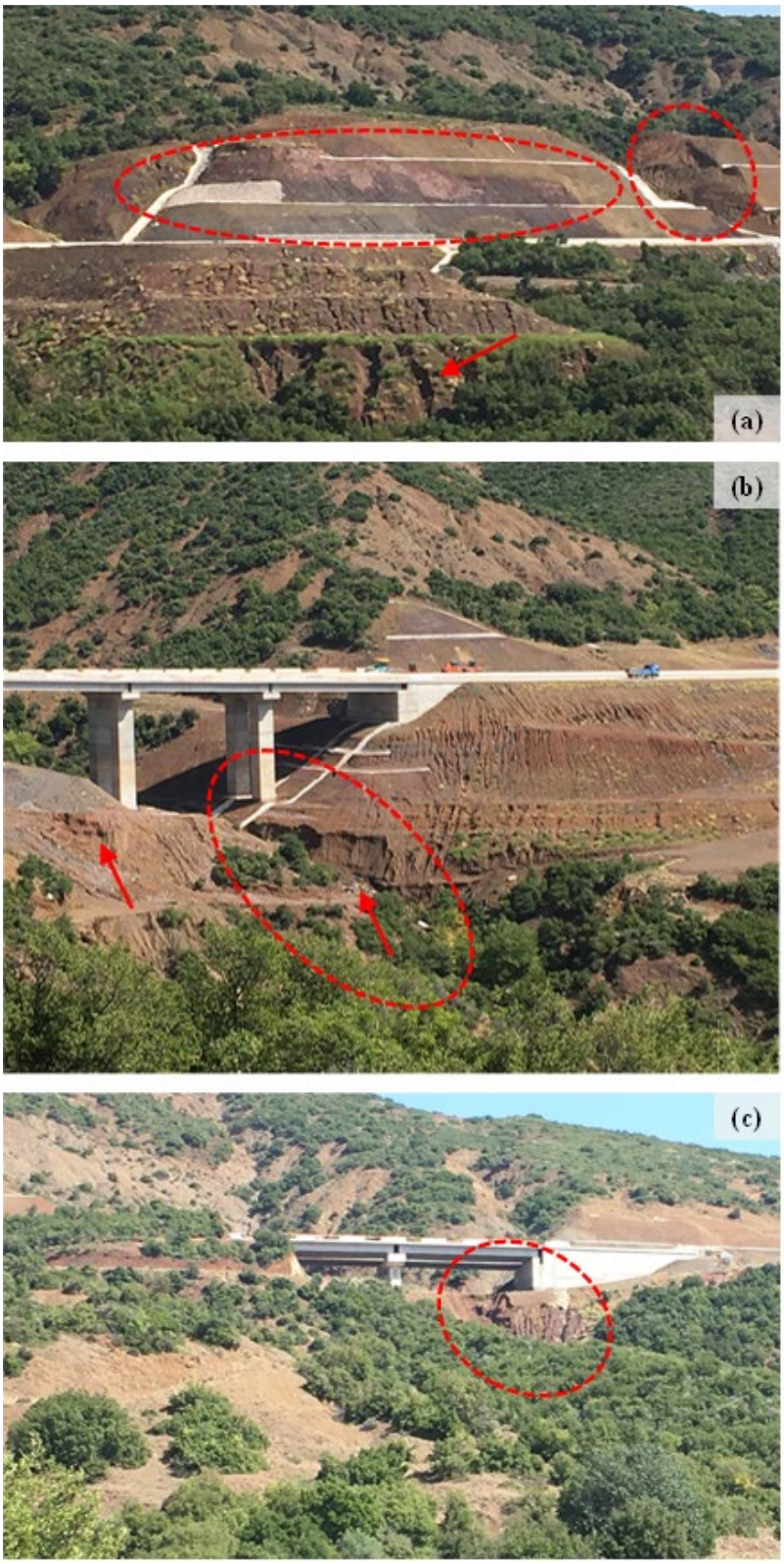

Figure 7.8. Evidence of erosion on embankments and slopes along the construction site of highway E65, north of Stirfaka village. Photos taken from: a) 38.97244167°N, 22.29606945°E; b) 38.97348055°N, 22.2946056°E; c) 38.96774722°N, 22.2956834°E, facing eastwards.

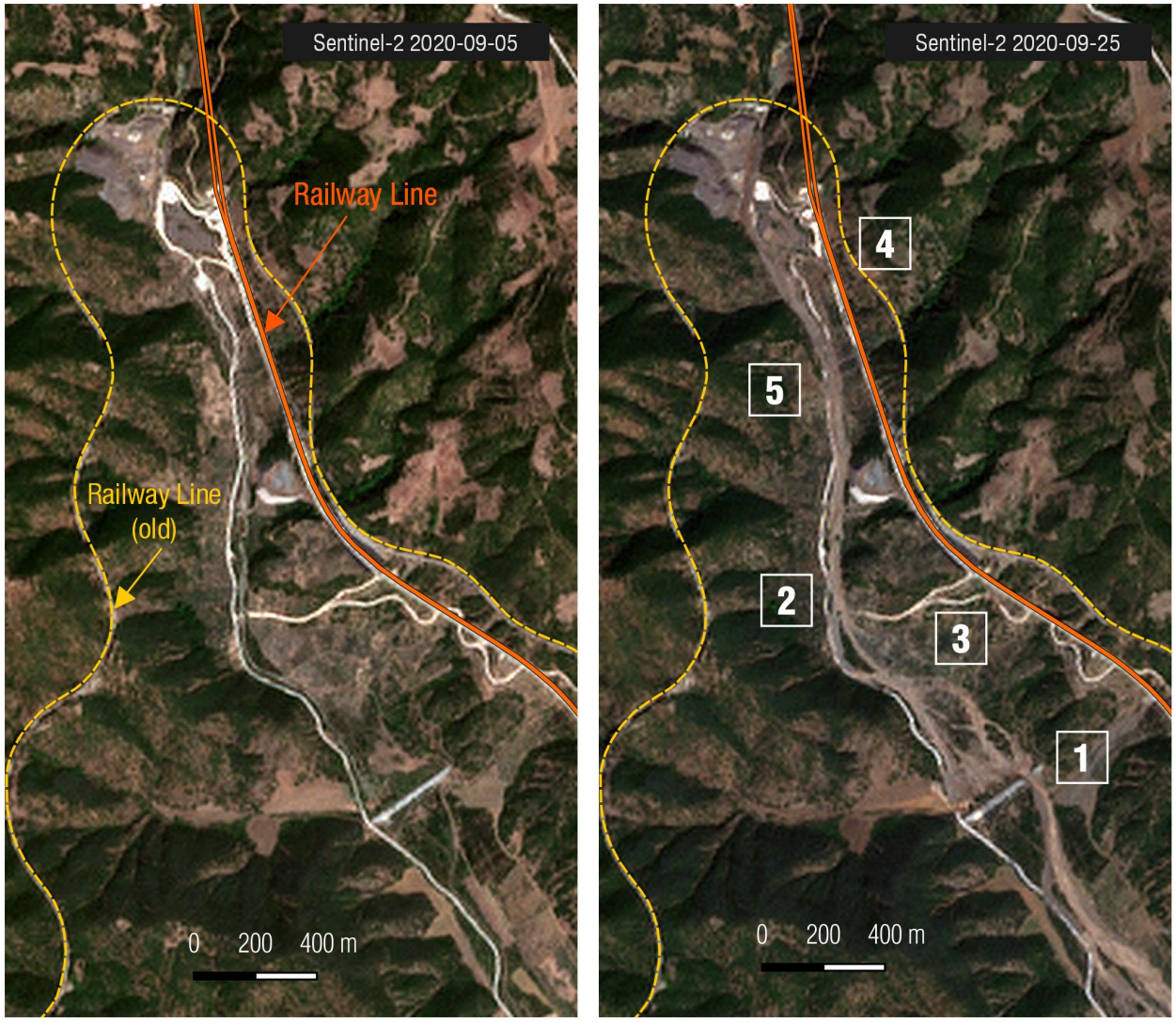

Figure 7.9. Flooding and debris effects on the streams northwest of Stirfaka, Lamia. Left: Sentinel-2 (super-resolution) image of September 5 2020. Right: Sentinel-2 (super-resolution) image of September 25 2020. Deposition of debris & flood sediments downstream along the torrent. Significant damages downstream that include breach of a flood-protection dam [1] (Location 38.9598°N, 22.27405°E), landslides along the old and new railway line (3,4) and service road damage (2,5).

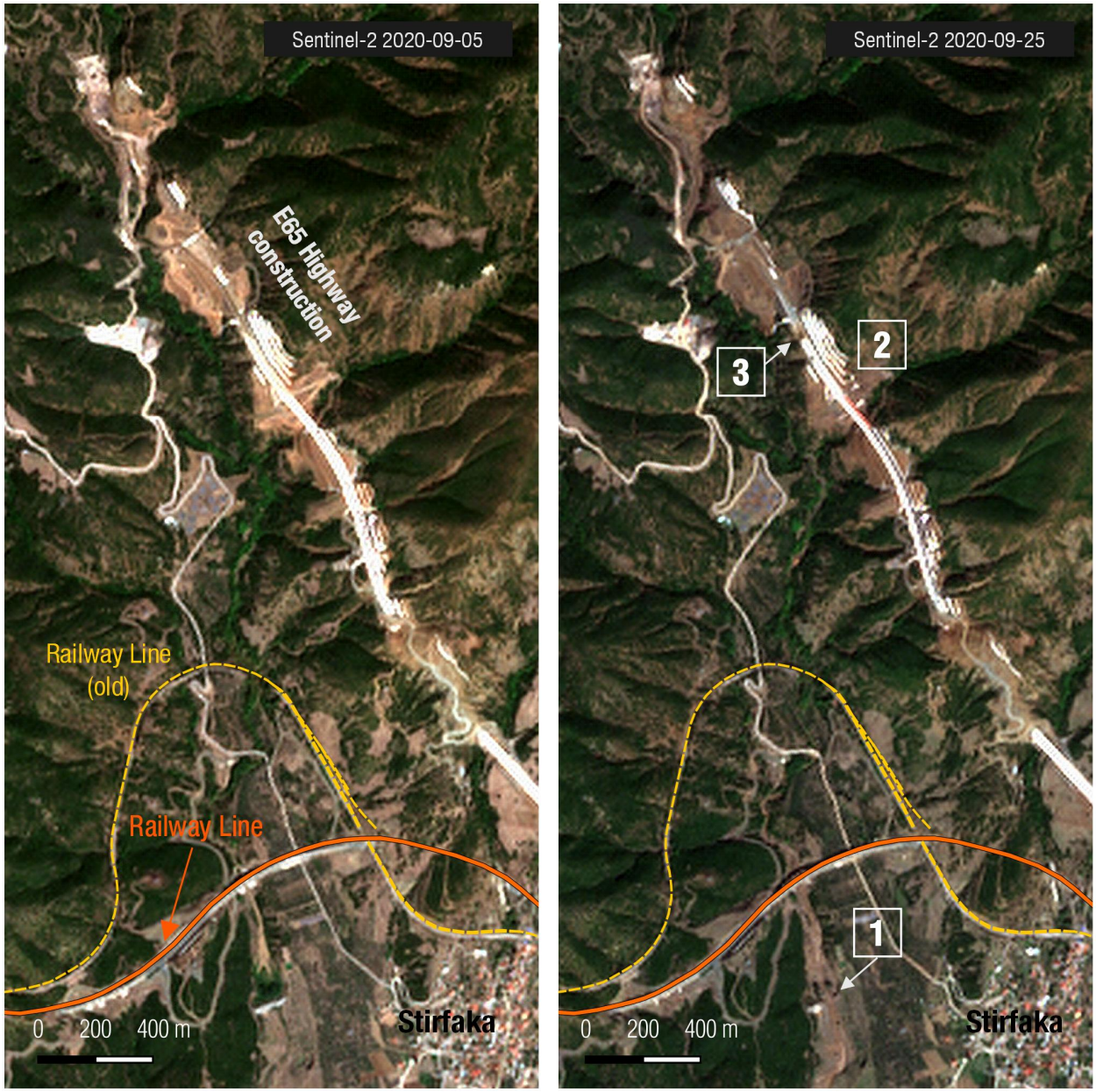

Figure 7.10. Flooding and debris effects on the streams and along the E65 highway construction site northwest of Stirfaka, Lamia. Left: Sentinel-2 (super-resolution) image of September 5 2020. Right: Sentinel-2 (super-resolution) image of September 25 2020. Deposition of debris & flood sediments downstream along the torrent. Significant damages downstream that include breach of a small flood-protection dam [1] (Location 38.9562°N, 22.29896°E), and landslides/failures along the E65 construction site (2,3).

Figure 7.11. Bridge embankment erosion on Highway E65, km+56 outside the town of Anavra (39.172474°N, 22.091382°E) (view 3D model at: https://skfb.ly/6W7AK).

7.3. Karditsa Region

Extensive riverbank erosion leading to embankment failures were also observed in the region of Karditsa, heavily affecting the road network in various places. These erosion failures were more pronounced in mixed flysch type and particularly in shale dominated flysch. Example of pronounced riverbank erosion is the damage in the village of Mouzaki, shown in Figure 7.12c, that caused the collapse of the local Mouzaki Health Center and, as discussed in Section 5.1.3, resulted in damage to the nearby bridges (Figures 7.12 and 7.13). Figure 7.14 provides a comparison of the Pamisos riverbed area near the village of Mouzaki before and after the flood event. Notably, the riverbed increased by over 100% (estimation based on Google Earth photos of the riverbed before the flood, and after, with pinned locations at the verge of collapsed embankments), leading to extensive erosion or even collapse of riverbank, road collapses, and the spectacular collapse of the Mouzaki Health Center.

Figure 7.12. Mouzaki road failure (a-d) and remedial measures (e-f) on river embankments (39.427222°N, 21.666667°E).

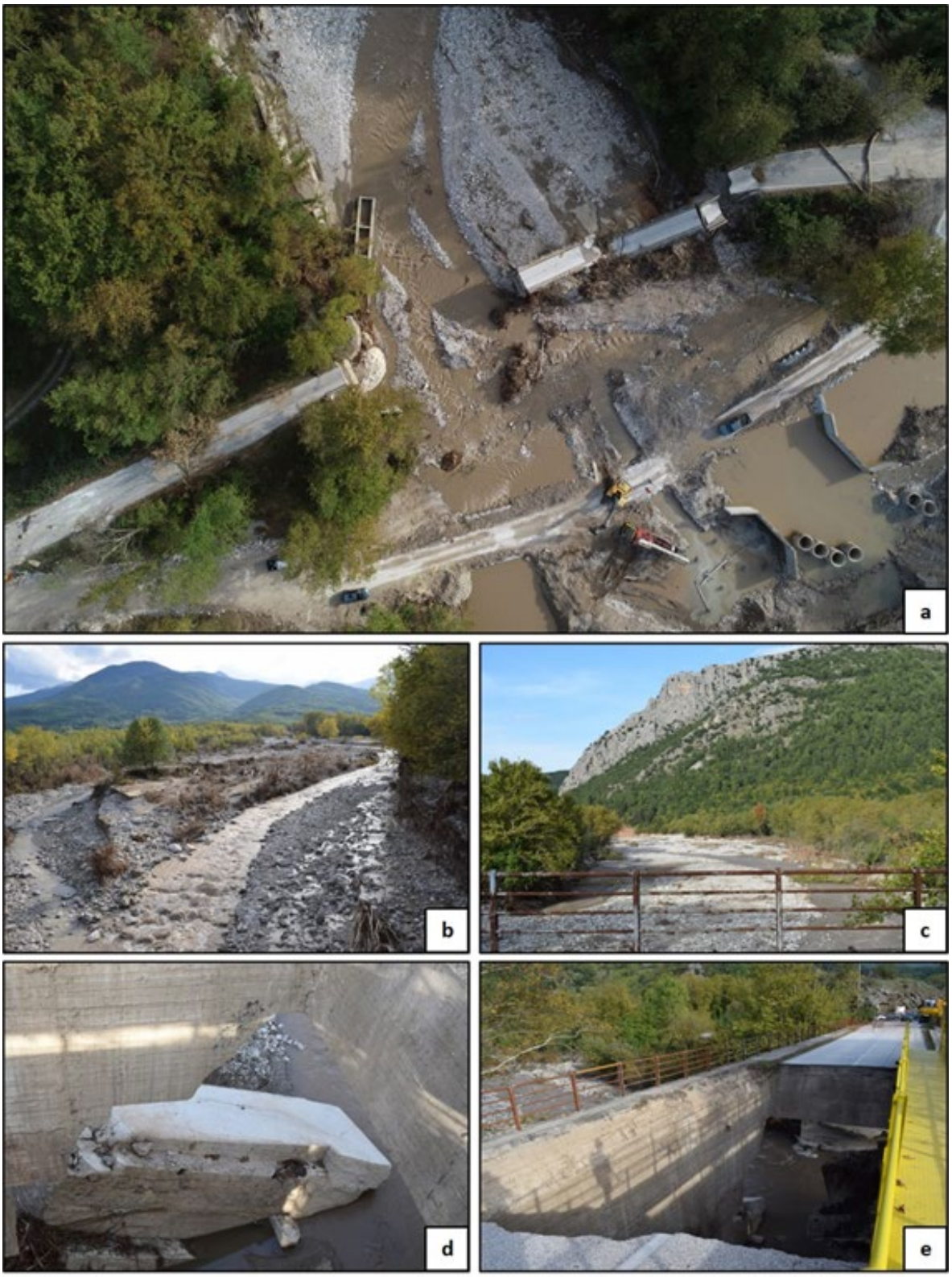

Figure 7.13. Debris flow caused damage to the bridges of a) Karaiskakis (39.401667 N, 21.653333 E), and b-e) Mpalanos (39.406111°N, 21.662778°E).

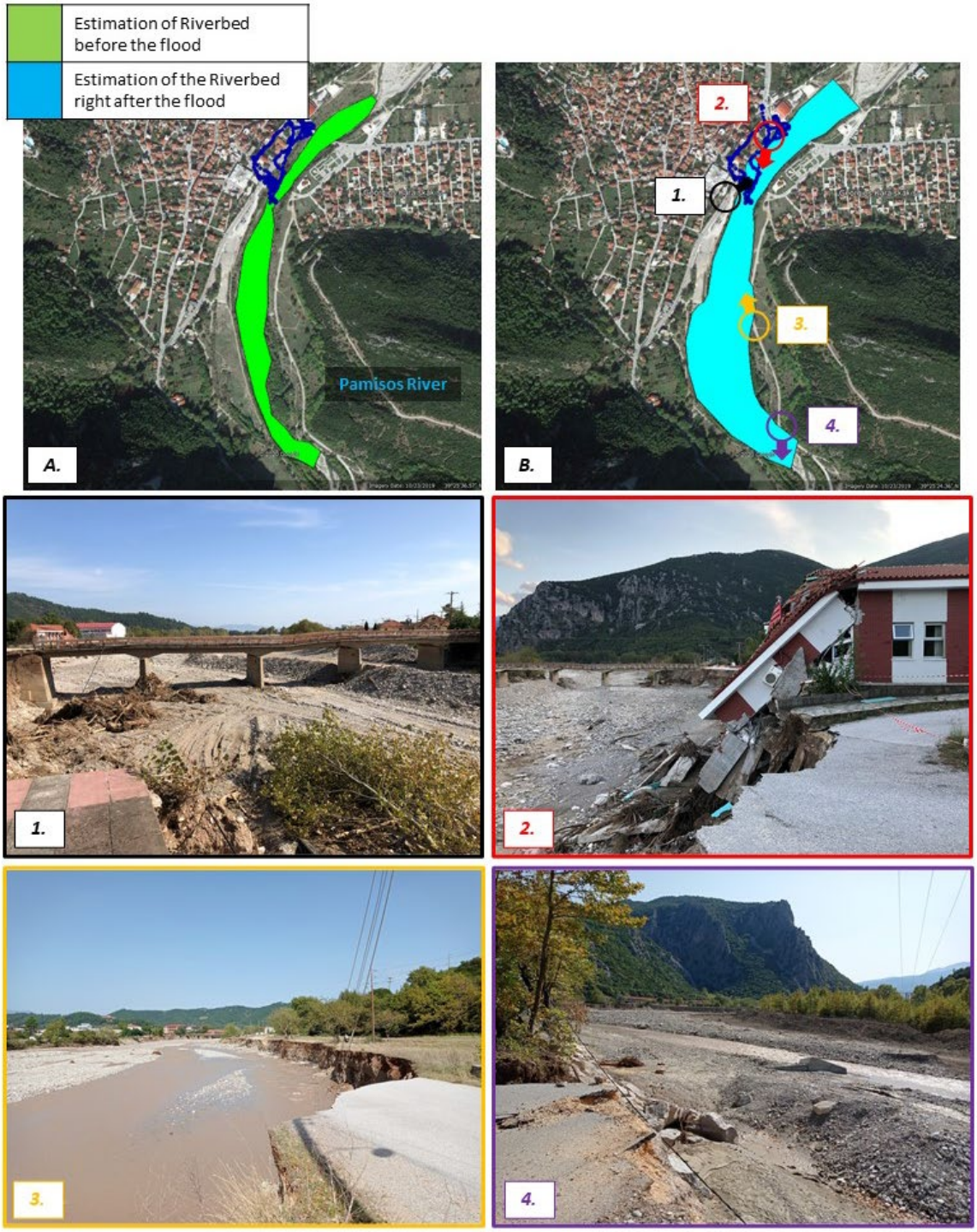

Figure 7.14. A) Pre-flood; and B) Post-flood riverbed area of the Pamisos river, estimated from the collapsed river embankments. The riverbed area increased by ~ 120%. 1) embankment collapse – part of the riverside road collapsed in the river; 2) the spectacular collapse of the Mouzaki Health Center, due to the erosion and collapse of the founding embankment; 3,4) extensive embankment and road collapse upstream of Mouzaki.

Moreover, erosion and flooding of the Karitsiotis River damaged and blocked the road crossing south of Belokomiti village, Plastira Lake, as shown in Figures 7.15 through 7.18. While the bridge itself did not collapse, road embankments on both sides were partially or completely washed out. The intersection of the roads west of the bridge was the most damaged part, blocking road traffic towards Elatos - Karvassaras and Mouha - Kastania. During the field investigation (October 1, 2020), repair works were underway in order to modify the river bed and restore the road embankments.

Riverbank erosion also caused several slope failures across the region as shown in Figures 7.19 through 7.26. The flooding of the river caused slope undercutting that resulted in road failures. Example of road embankment failures in weathered mantle of mixed flysch are shown in Figures 7.25 and 7.26. In Figure 7.25, the height and the width of the slope were estimated at 15 and 30 meters respectively, while in Figure 7.26, the surface erosion was extensive reaching a depth of 8-10 meters. A retaining wall that supported the road failed while nearby slopes were intensely eroded.

Figure 7.15. Riverbank erosion – slope failure that blocked the road. Karitsiotis river bridge, south of Belokomiti, Plastira Lake. (39.25381°N, 21.71591°E).

Figure 7.16. Comparison of previous state (Google Street View image) and post-Ianos damaged river pass at Karitsiotis river bridge, south of Belokomiti, Plastira Lake. (39.25381°N, 21.71591°E).

Figure 7.17. View towards south-west from the remaining Karitsiotis river bridge, south of Belokomiti, Plastira Lake. Comparison with Street View image. (39.2538°N, 21.7161°E).

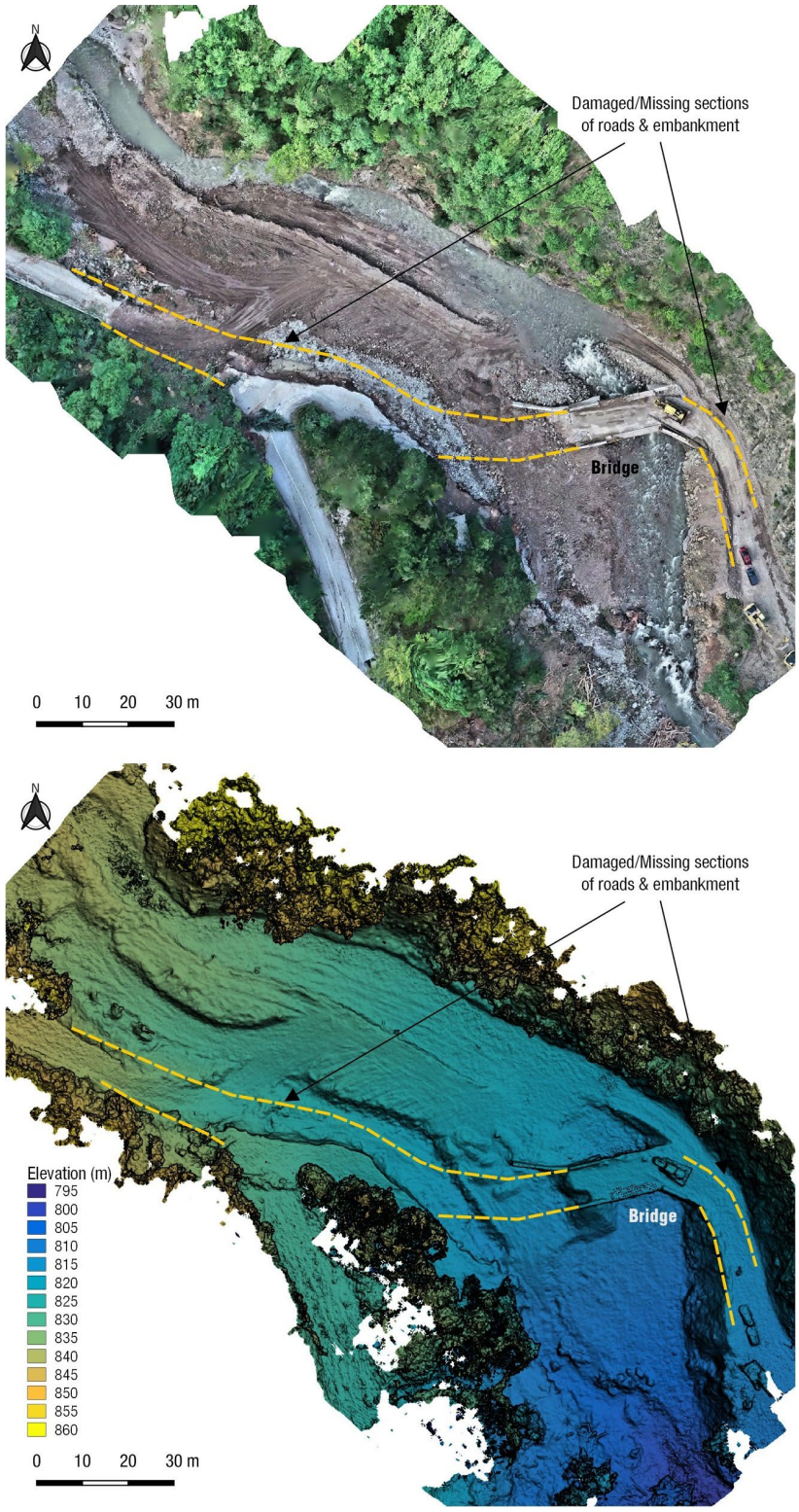

Figure 7.18. UAV survey of Karitsiotis river bridge site, south of Belokomiti, Plastira Lake. (39.25381°N, 21.71591°E). Top: orthophoto. Bottom: DSM shaded relief extracted from point-cloud.

Figure 7.19. Riverbank erosion – slope failure that damaged the road at the village Pezoula. (39.30351°N, 21.6876°E)

Figure 7.20. Riverbank erosion – slope failure that damaged partially the road. (39.26247°N, 21.71319°E)

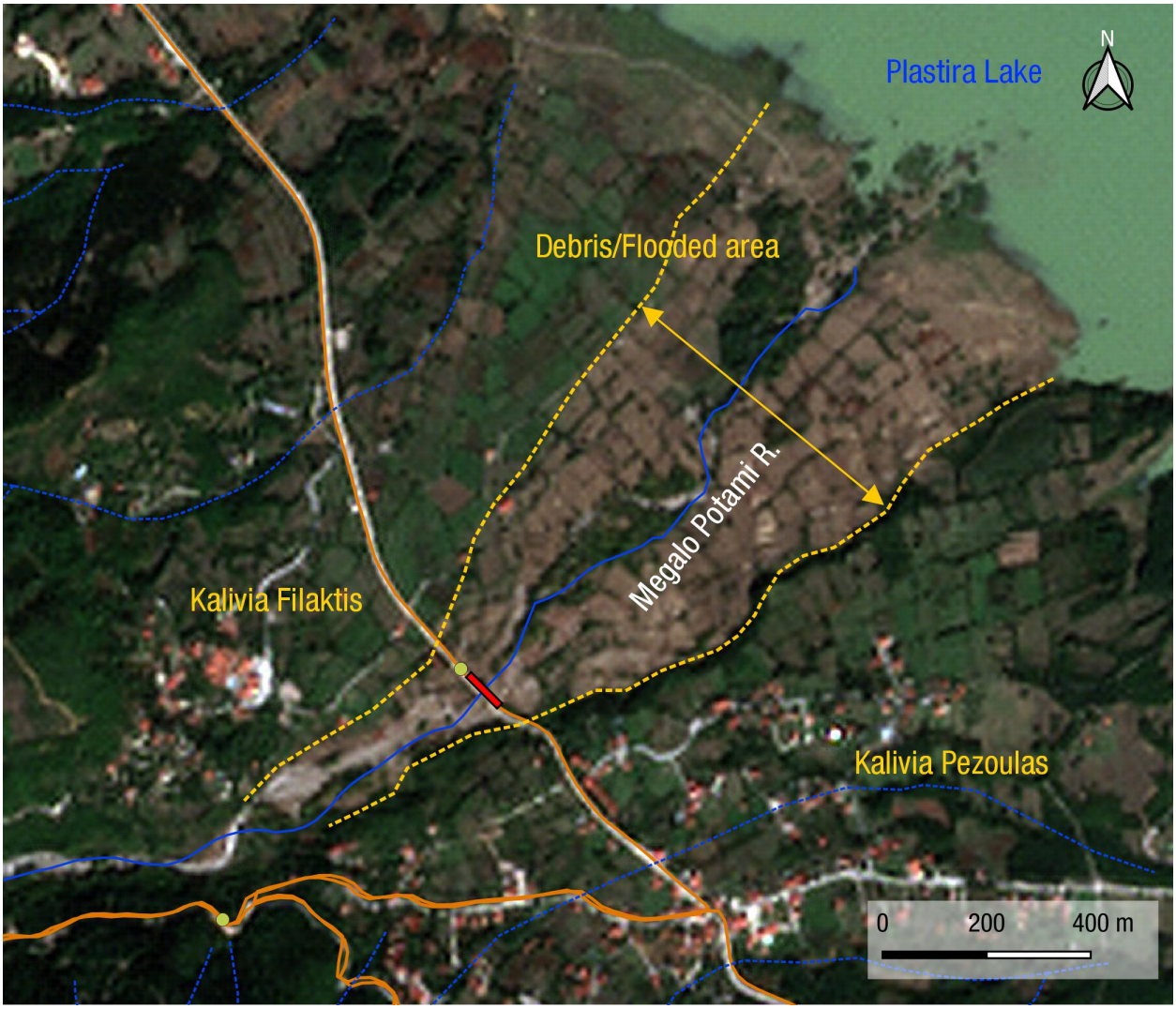

Figure 7.21. Riverbank erosion and debris flow near Pezoula and Filakti, Plastira Lake. Brown-discolored area in Megalo Potami river fan shows the extent of flooding and debris deposition. Red bar marks the location of the damaged road bridge (39.31226°N, 21.7109°E). Sentinel-2 (super-resolution) satellite imagery acquired on September 25.

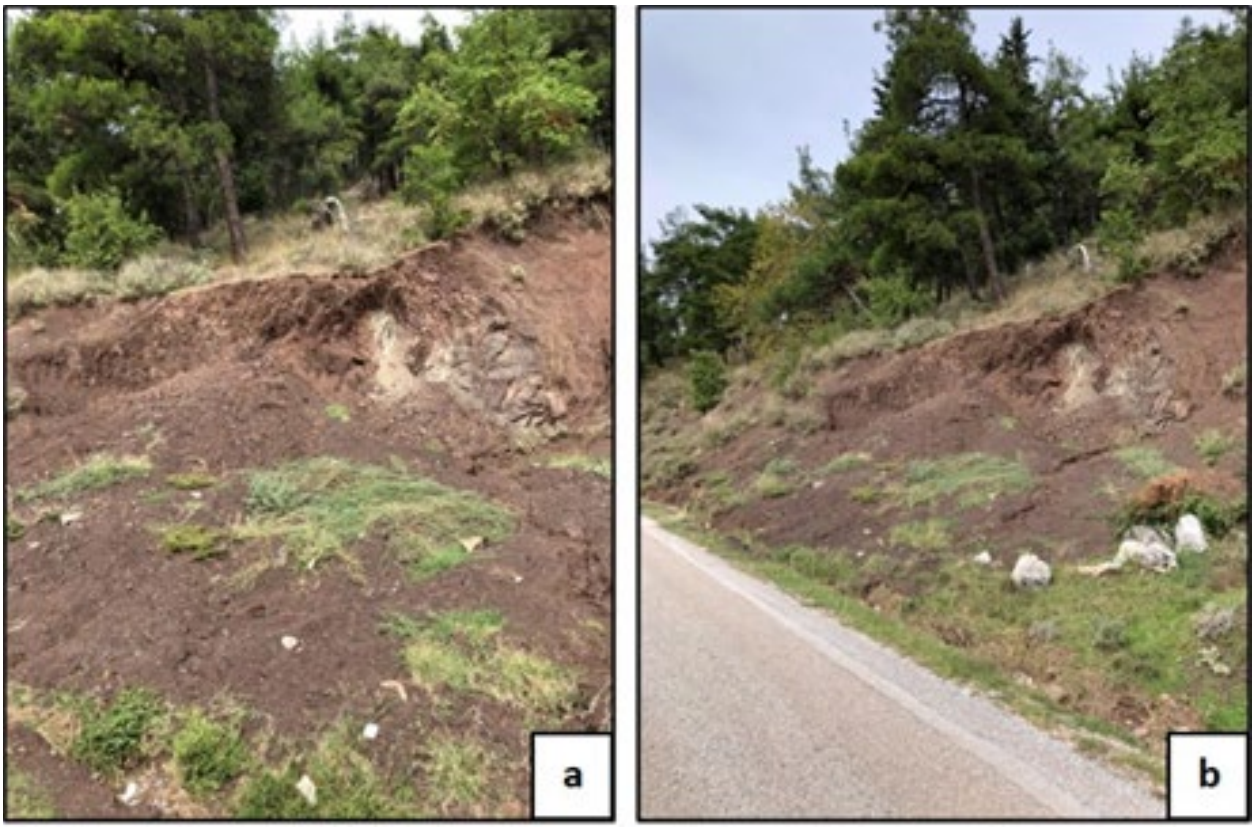

Figure 7.22. Surface erosion on Mouzaki to Porti road (39.410556°N, 21.658611°E).

Figure 7.23. Extensive surface erosion on the side of Belokomiti - Karditsa road. (39.26022°N, 21.72556°E).

Figure 7.24. Riverbank erosion – slope failure that totally damaged the road at Vlasi village (39.2906260°N, 21.5862230°E).

Figure 7.25. Riverbank erosion – slope failure that partially damaged the road (39.2515460°N, 21.8736180°E).

Figure 7.26. Extensive surface erosion on the side of Kastania – Rachoula road. Failure of retaining wall (39.2314830°N, 21.8016040°E).

8. Flood Protection System in Karditsa

A flood protection system that consists of levees and bridges on the southern part of Karditsa protect the city from a potential flood event of the Gavria Creek, which is intersected by the Gavras River to the west and the Karampalis River to the east, as can be seen in Figure 8.1. The system failed to withhold the flooded waters, during the heavy rainfall (reportedly 214 mm of water in 24 hours, or 54,000,000 tons of water) between September 17-18, 2020, and as a result, the city of Karditsa flooded (reportedly over 80 cm of water). A team of two civil engineers, supported by Mr. Konstantinos Pistrikas, a local hydraulic engineer with over 40 years of experience in the local hydrology of the broader area of Karditsa, inspected the flood protection levees during a two-day trip from 2 – 3 October 2020 and reported their failures. Table 8.1 summarizes the assets that were inspected, which fall into two categories: levees and bridges (asset coding is consistent with that of Figure 8.1 and with that of Table 5.1). The Gavria Creek flows to the east, and is inhibited from flooding Karditsa from a system of levees on its northern bank, which are intersected by highway bridges (one or two lanes/ direction). Right next to the bank lies an irrigation channel of significantly lower section. On its southern bank, the creek is not contained by any levees, and is hence free to overflow. Figure 8.5a provides a conceptual overview of the arrangement of the flood protection levees of the Gavria Creek.

Out of the five bridges inspected, which are both newly constructed, and old with obvious signs of ageing and poor maintenance (e.g. exposed rebar for the case of Bridge No. 6), none had signs of structural damage or abutment distress/ extensive displacement (see also 5.1.3). However, they all had signs of overflowing by the flood discharge of the Gavria Creek, which hints to poor hydraulic design, since their hydraulic sections were proven inadequate for this flood event. More specifically, Bridge No. 3 (Figure 8.2a, 8.2b, and 8.2c) is built next to an old and obsolete bridge, which apparently exacerbated the flood discharge, by reducing further the already insufficient hydraulic section. Bridge No. 3, as well as a utility bridge right across the flow of the creek (Figure 8.2c), have clear marking of the maximum height of the water, leading to the conclusion that the flooded waters overtopped the old bridge, whose deck is on a lower elevation. Bridge No. 6 (Figure 8.2d, 8.2e, and 8.2f), Bridge No. 5 (Figure 8.2a; 8.2b, and 7.27c), and Bridge No. 4 (Figure 8.3d, 8.3e, and 8.3f) also contributed to the flooding of Karditsa by "blocking" the creek flow. Poor maintenance of the riverbed was also an issue, further reducing the effective hydraulic sections beneath the bridges. Tree trunks, mud, debris, even corpses of animals from livestock facilities upstream were found in the riverbed (Figure 8.3f). Figure 8.3e shows the lower elevation of the Bridge No. 4 deck compared to the crest of the flood protection levee. The waters merely overtopped the bridge and flooded the area to the north. Railway Bridge No. 1 (Figure 8.4) is an out-of-use old railway steel bridge, which had a clear mud line, indicative of the maximum discharge height. Notably, a permanent concrete dam with temporary lags is placed slightly upstream this bridge (Figure 8.4c). The lags are used in the summer months, to confine the river flow and create a small-scale reservoir for irrigation purposes. As per local narratives, the lags were not placed in the dam during the flood, thus did not further constrain the flow.

Table 8.1: Damage assessment on levees and bridges across the Gavria Creek levee system

Asset Type & ID	Latitude (N)	Longitude (E)	Damage Assessment
Bridge No. 3	39.344589°	21.894189°	Hydraulic failure - No Structural Failure
Bridge No. 6	39.345069°	21.926347°	Hydraulic failure - No Structural Failure
Bridge No. 5	39.346522°	21.920672°	Hydraulic failure - No Structural Failure
Bridge No. 4	39.348575°	21.904591°	Hydraulic failure - No Structural Failure
Railway Bridge No. 1	39.346627°	21.9352050°	Hydraulic failure - No Structural Failure
Levee 01	39.347550°	21.890664°	Local Collapse of Irrigation Channel; Extensive Erosion and Partial Collapse of Levee to the north
Levee 02	39.343994°	39.343994°	Minor Surface Erosion of Levee to the north on the upper part
Levee 03	39.348173°	21.915506°	Extensive Erosion of Levee to the north

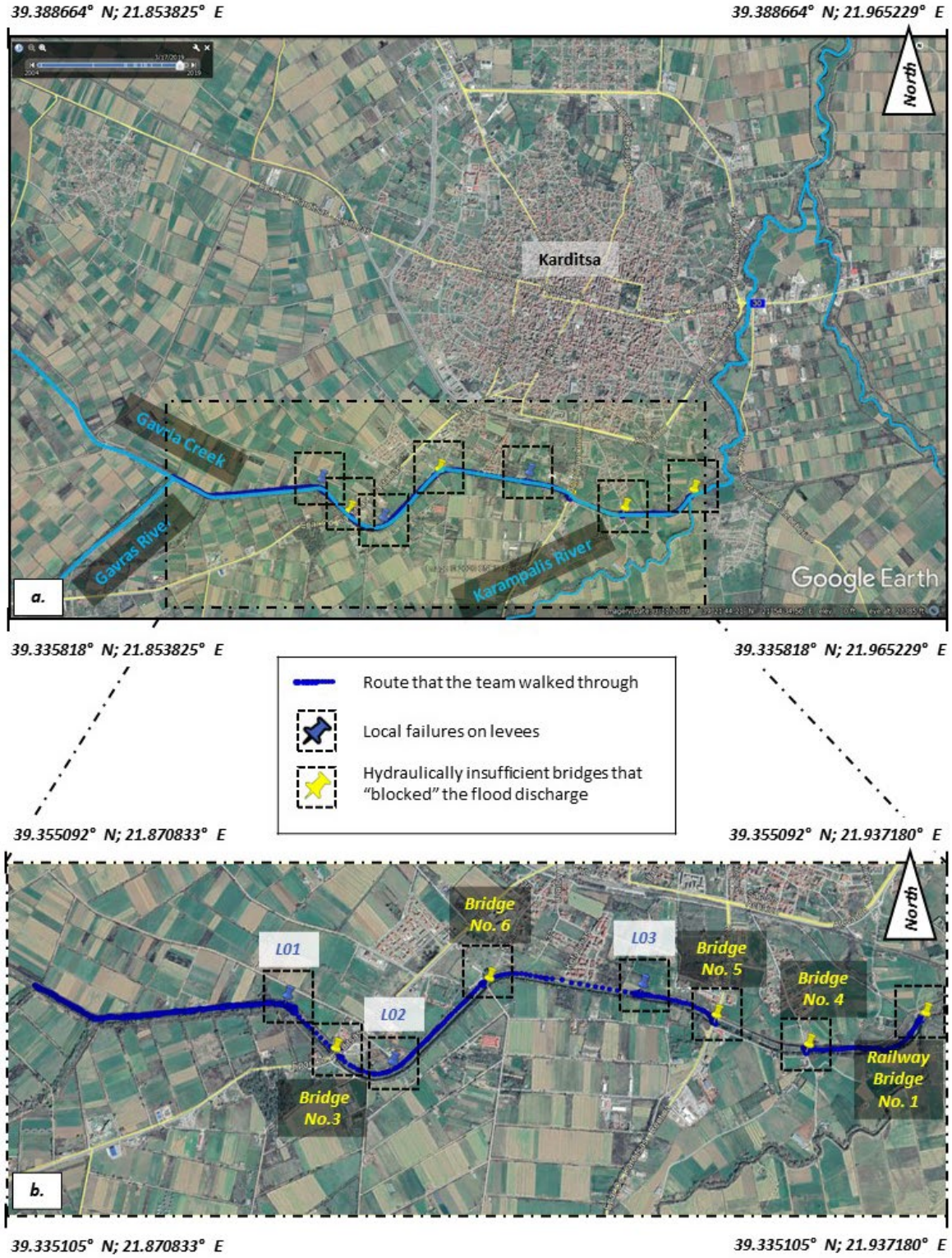

Figure 8.1. (a) Overview of the rivers and creeks that flooded the city of Karditsa; (b) Levees with local failures (*L##*) and hydraulically insufficient bridges (*Bridge No. #*) along the Flood Protection Levee of the Gavria Creek and the Karampalis River.

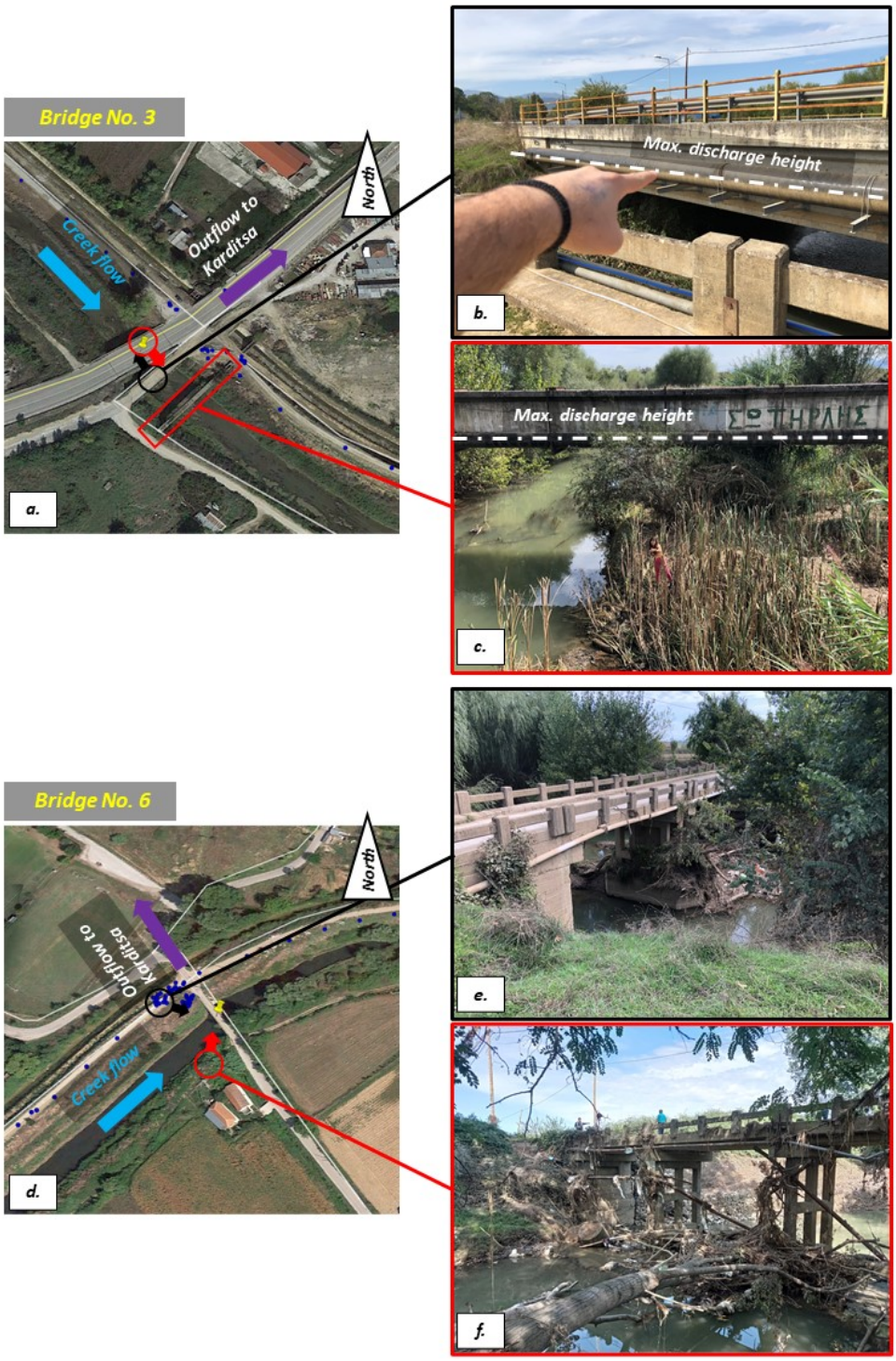

Figure 8.2. (a; b; c) Bridge No. 3 (39.34458922°N; 21.89418983°E): (a) location, (b) evidence of overflow from the horizontal mudline (photo taken from the old bridge on the SE of Bridge No. 3), (c) evidence of overflow on an old utilities bridge (on the SE of Bridge No. 3); (d; e; f) Bridge No. 6 (39.34506944°N; 21.92634722°E): (d) location, (e) section that failed to discharge the flow during the flood event, (f) debris leftovers on the riverbed.

Figure 8.3. (a; b; c) Bridge No. 5 (39.34652222°N; 21.92067222°E): (a) location, (b) section that failed to discharge the flow during the flood event, (c) debris leftovers on the bridge girders (photo taken below the bridge); (d; e; f) Bridge No. 4 (39.348575°N; 21.90459167°E): (d) location, (e) the Flood Protection Levee is lowered at the location of Bridge No. 4, hence leaving a free pass to the flooded water to the north, (f) debris leftovers on the riverbed.

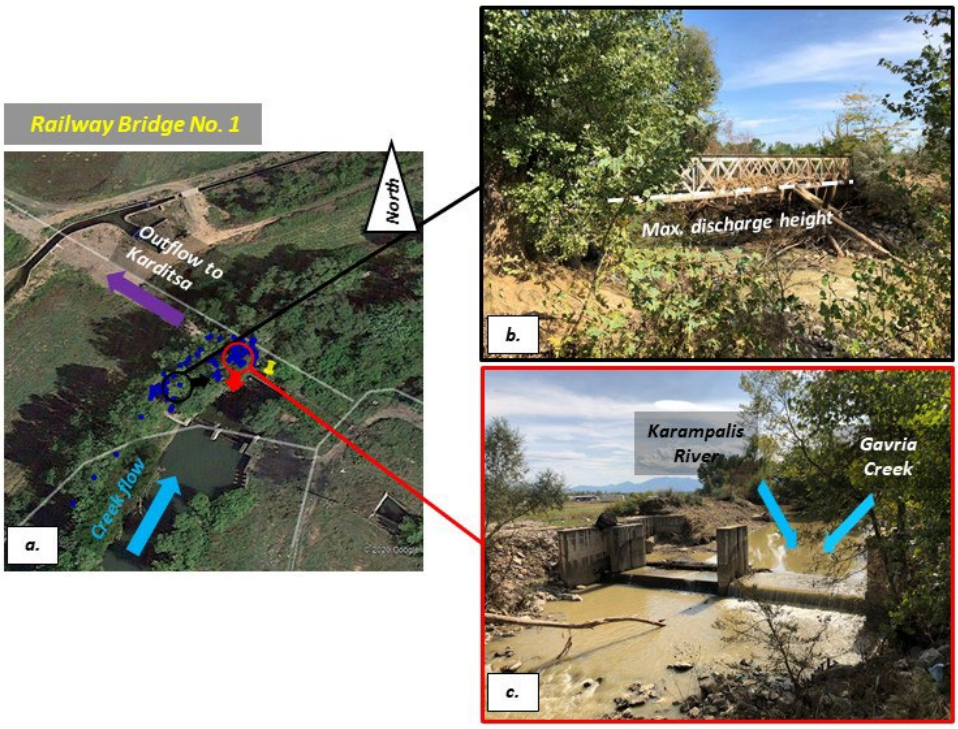

Figure 8.4. Railway Bridge 01 (a) location (39.346627°N; 21.935205°E), (b) photo of the railway Bridge 05 (the max. discharge height is estimated from the horizontal mud line on the bridge); (c) permanent concrete dam with temporary horizontal lags upstream Railway bridge No. 5 – the dam is placed at the intersection of the Gavria Creek with the Karampalis River.

All three inspected levees had evidence slight to extensive erosion to the northern side (to Karditsa). This side has lesser vegetation, hence is more vulnerable against erosion, but at the same time is more accessible. The southern side (the bank of the Gavria Creek) of the levees sustained lower to no damage, but the inspection was not carried out as meticulously there, due to the presence of high vegetation and trees. Presumably, the latter protected this side of the levee more effectively. No levee collapsed, indicating that the water did not reach the crest elevation, but rather overflew to the south, or to the north from the passages created by Bridge No. 3 - No. 6, which is also demonstrated in Figure 8.5 conceptually. The particular location of the erosive patterns (Figure 8.5b) regardless of their extent (slight to extensive) indicates that they were caused by the flooding of the irrigation channel, due to the discharge of the creek flow over the bridges to the north. Presumably, once the waters passed over the bridges, they inundated the channel, and eroded the northern side of the protection levees.

More specifically, Levee 01 had signs of extensive erosion, and the irrigation channel had collapsed locally, allowing the flooded waters to flow to the north uninterruptedly (Figure 8.6). A light green and a light blue zone can be seen in Figure 8.6a, indicative of slight and extensive damage zones, respectively. Increased water velocity due to reduced hydraulic section, circular longitudinal segments of the channel, or the presence of obstacles, such as the water-gate a few

hundred meters downstream the blue zone (close to point 1 of Figure 8.6a) could have led to the extensive erosion and the local failure of the irrigation channel concrete section at this specific location, while the flow upstream caused less severe distortion. Levee 02 (Figure 8.7) had minute damage, and the surface erosion may be irrelevant to the flood event, as no other indications exist suggesting that the irrigation channel was flooded at this point. On the contrary, at the location of Levee 03 (Figure 8.8), the irrigation channel was fraught with mud debris depositions, and extensive erosion was observed. What is more, by the arrival of the reconnaissance team (October 2, 2020), part of the levee had already been restored with layers of compacted soil, suggesting that (1) the traffic on the crest would have been imperiled by the degree of section loss due to erosion, and (2) the local authorities wanted to fix the levee quickly, for preparedness against a new flood event in the near future.

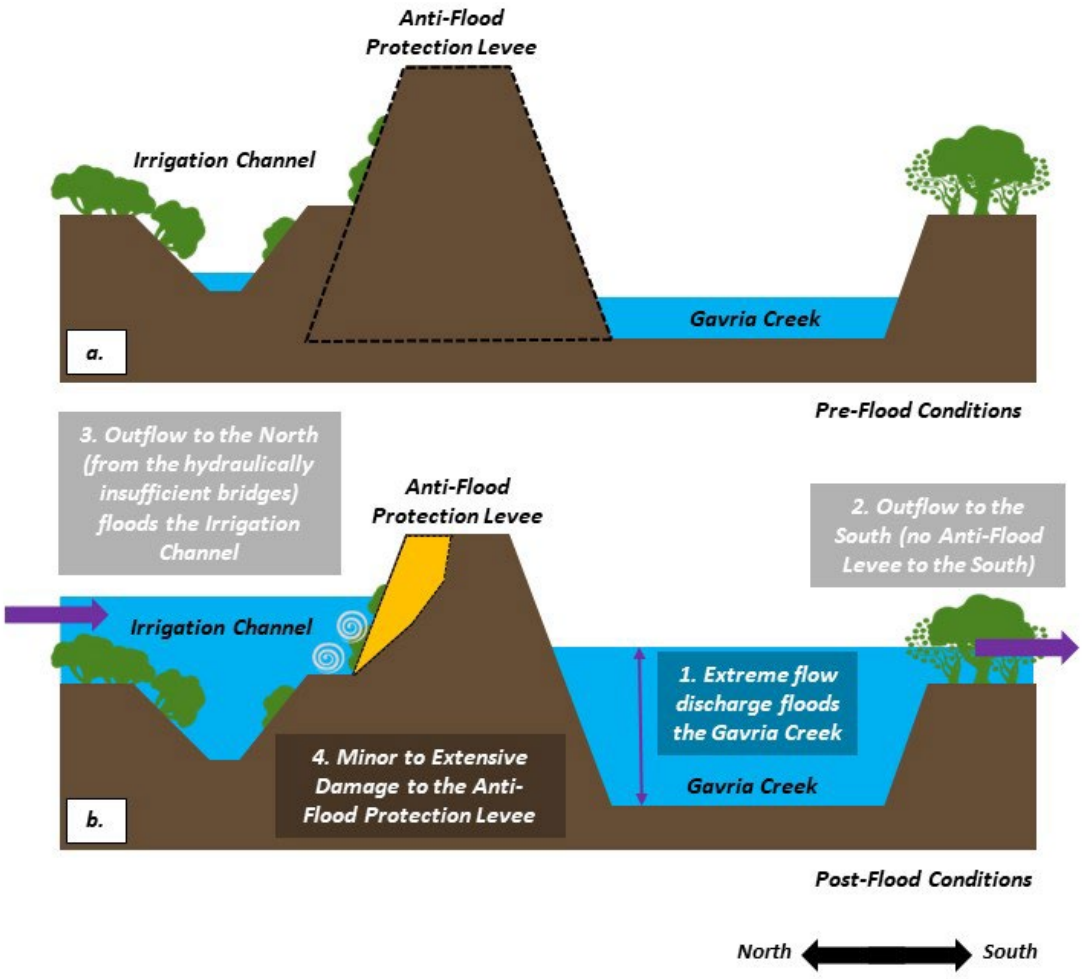

Figure 8.5. Conceptual sketches of the erosion damage on the Flood Protection Levee, on its northern side: (a) pre-flood conditions & (b) post-flood conditions and 4-step explanation of the erosion mechanism.

Figure 8.6. (A) location of Flood Protection Levee 01 (39.347550°N; 21.890664°E) – the Flood Protection Levee sustained extensive damages over an area of ~ 2,500 m2 (light blue) and slight damage over an area of ~ 5,500 m2 (light green); (1) extensive damage with bottom-up erosion of the levee (courtesy of *Mr. Apostolos Vergis*); (2) local collapse of the irrigation channel section, (3) extensive erosion of the levee downstream the irrigation channel failure.

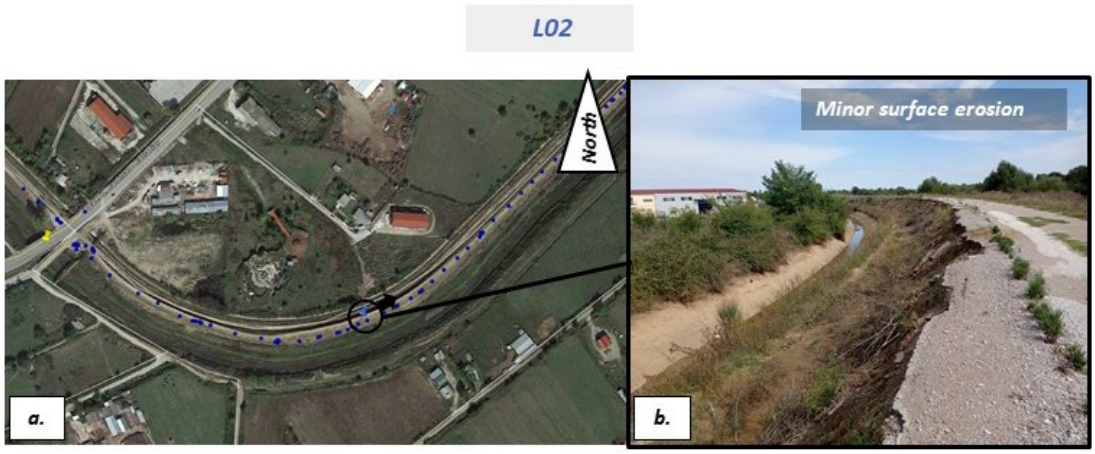

Figure 8.7. (a) location of Flood Protection Levee 02 (39.343994°N; 21.898058 E); (b) minor surface erosion on the crest of the levee.

Figure 8.8. (A) location of Flood Protection Levee 03 (39.348173°N; 21.915506°E); (1) extensive damage with loss of a significant part of the levee section (was compacted when we arrived there on October 2, 2020); (2) extensive erosion caused most probably by vortices of the flooded irrigation channel; (3) debris build up on the irrigation channel (photo looking downstream).

9. Conclusions and Recommendations for Additional Work

9.1. Conclusions

Based on the Medicane Ianos post-event reconnaissance, the following general conclusions can be drawn:

- Cephalonia and Lefkada Islands

    1. The northern part of Cephalonia, characterized by steeper slopes and narrower basins was heavily affected, mainly, by extensive debris flows that typically traveled long distances.
    2. The road network of Cephalonia proved to have inadequate flood protection capacity against phenomena such as Medicane Ianos.
    3. In Lefkada, geo-related effects were not pronounced with the exception of the western coastline that was affected by landslides during the 2015 earthquake where there is evidence of sediment transport and continued landsliding.

- Lamia Region

    1. The northern part of Spercheios River basin, and particularly the south side of mount Orthrys, was affected by extensive erosion and scouring.
    2. Road and railway embankments, some under construction, proved vulnerable to erosion/scour during intense precipitation.
    3. Landsliding phenomena were not observed.

- Karditsa Region

    1. Significant landsliding and ground failures occurred in this region. The two study areas (Northwest and Southeast of Plastiras reservoir) show significant differences in the pattern of mass movements.
    2. In the northwest part, the dominant feature is the increased transport of debris and boulders in the streams resulting in debris flows and earth flows. The morphology in this area is steeper and the erosion is more pronounced.
    3. This resulted in the damage of many bridges primarily in this area.
    4. In the southeastern part, landsliding is more pronounced. The flysch type is mostly characterized by alternations of shale and sandstone and the weathered mantle is thick.
    5. The pattern and density of landslides, spotted by the satellite imagery, agrees well with the data collected in the field.

6. Extensive damage occurred on the railway network. The main source of damage in the railway network was ballast scouring and washout in the flooded sections of western Thessaly plain.

9.2. Recommendations for Additional Work

Medicane Ianos demonstrated that many communities are vulnerable to such high intensity precipitation events. The Phase 1 deployment collected valuable perishable data, but also identified the need for additional investigations that can be completed as part of a Phase 2 deployment or other research studies.

More than 1,400 landslides are already identified by the satellite, and several of them have been assessed in-situ, however, a more complete assessment of landsliding, is still needed. The current data indicates that there is a pronounced geological aspect on the landslide densities observed, but this needs to be explored further. Large areas affected by landslides were inaccessible at the time of the reconnaissance due to damage, flooding and landslides intercepting the road network. Particularly, possible areas for further study, include Kastania – Rachoula section (between location 12 and 51), Itamos area (since there was no access to the village after location 48), and Livadia area (locations 42 – 43). Mapping along the roadways will be particularly valuable. In addition, a better characterization of the rock units involved will be prudent.

Additional field work is also needed along the western coastline of Lefkada where clearly there is ongoing landslide activity and previous data were collected. Some imagery was collected, but Lidar based data will prove particularly useful. The collected data can be compared against available satellite imagery and/or previous UAV deployments to the island.

The damage on the bridges was particularly pronounced. Bridges were washed out in some areas, or in other areas moved or were distressed. An assessment of the mode of failure of these bridges as well as the embankments built to access them is particularly interesting. The vulnerability of these and other bridges is a critical consideration in assessing the resiliency of these communities.

REFERENCES

Briaud, J.-L. (2008). Case histories in soil and rock erosion: Woodrow Wilson Bridge, Brazos River Meander, Normandy Cliffs, and New Orleans levees; 2007 Ralph B. Peck lecture. *J. Geotech. Geoenviron. Eng.*, **134**(10), 1pp. 425–1447.

Briole, P., P. Elias, I. Parcharidis, C. Bignami, G. Benekos, S. Samsonov, C. Kyriakopoulos, S. Stramondo, N. Chamot-Rooke, M.L. Drakatou and G. Drakatos (2015). The seismic sequence of January–February 2014 at Cephalonia Island (Greece): constraints from SAR interferometry and GPS, Geophysical Journal International, 203, 1528-1540, doi:10.1093/gji/ggv353

Dafis, S., Ch. Claud, V. Kotroni, K. Lagouvardos, and J-F Rysman (2020). Insights into the convective evolution of Mediterranean tropical-like cyclones. *Quarterly Journal of the Royal Meteorological Society* https://doi.org/10.1002/qj.3896

FHMP (2018). Flood Hazard Management Plant for Thessaly Water District (EL 08). FEK 2685B 6-07-2018. Ministry of the Environment and Energy. Athens, Greece, 2018. https://floods.ypeka.gr/

GEER/EERI/ATC (2014), "Earthquake reconnaissance January 26th/February 2nd 2014 Cephalonia, Greece events," Version 1: June 6. 2014

González-Alemán, J.J., Pascale, S., Gutierrez-Fernandez, J., Murakami, H., Gaertner, M.A. and Vecchi, G.A. (2019). Potential increase in hazard from Mediterranean hurricane activity with global warming. *Geophysical Research Letters* **46**, pp. 1754–1764. https://doi.org/10.1029/2018GL081253.

Govindasamy, A. V. (2009). *Simplified method for estimating future scour depth at existing bridges*. Ph.D. dissertation, Texas A&M Univ., College Station, TX.

Huffman, G., Bolvin, D., Braithwaite, D., Hsu, K., Joyce, R., Kidd, C., Nelkin, E., Sorooshian, S., Tan, J., Xie, P. (2019) NASA Global Precipitation Measurement (GPM) Integrated Multi-satellitE Retrievals for GPM (IMERG), version 6.0. NASA's Precipitation Processing Center, accessed October 2, 2020, https://jsimpsonhttps.pps.eosdis.nasa.gov/imerg/early/202009/

Kotroni V., and K. Lagouvardos (2008). Lightning occurrence in relation with elevation, terrain slope and vegetation cover over the Mediterranean. *Journal Geophysical Research - Atmospheres* **113**, D21118, https://doi.org/10.1029/2008JD010605.

Lagouvardos K., V. Kotroni, S. Nickovic, D. Jovic, and G. Kallos (1999). "Observations and model simulations of a winter sub-synoptic vortex over the Central Mediterranean". *Meteorological Applications* **6**, pp. 371-383.

Lagouvardos K., V. Kotroni, A. Bezes, I. Koletsis, T. Kopania, S. Lykoudis, N. Mazarakis, K. Papagiannaki, and S. Vougioukas (2017). The Automatic Weather Stations Network of the National Observatory of Athens: Operation and Database. *Geoscience Data Journal* **4**, 4-16, https://doi.org/10.1002/gdj3.44.

Lagouvardos K., S. Dafis, Ch. Giannaros, Ath. Karagiannidis, V. Kotroni (2020). Investigating the role of extreme synoptic patterns and complex topography during two heavy events in Crete in February 2019. *Climate* **8**, 87. https://doi.org/10.3390/cli8070087.

Stathopoulos, N., Lykoudi, E., Vasileiou, E., Rozos, D., Dimitrakopoulos, D. Erosion Vulnerability Assessment of Sperchios River Basin, in East Central Greece - A GIS Based Analysis. Open J. Geol. 2017, 7, 621-646, doi:10.4236/ojg.2017.75043

Pyrgiotis L. (1997). Engineering geological conditions in Karditsa Prefecture. Landslide phenomena in the flysch formation. PhD thesis. Univ. of Patras.

Rondoyanni, Th., Sakellariou, M., Baskoutas, J., Christodoulou, N., 2012. Evaluation of active faulting and earthquake secondary effects in Lefkada Island, Ionian Sea, Greece: an overview. Nat. Hazards 61 (2), 843–860.

Scordilis, E.M., Karakaisis, G.F., Karacostas, B.G., Panagiotopoulos, D.G., Comninakis, P.E., Papazachos, B.C., 1985. Evidence from transform faulting in the Ionian Sea: the Cephalonia island earthquake sequence of 1983. PAGEOPH 123, 387–397.

Tsangaratos, P., Loupasakis, C., Nikolakopoulos, K., Angelitsa, V., Ilia, I (2018). Developing a landslide susceptibility map based on remote sensing, fuzzy logic and expert knowledge of the Island of Lefkada, Greece. Environ. Earth Sci., 77, 363.

Tsubaki, R., Kawahara, Y., Sayama, T., and Fujita, I. (2012) Analysis of geomorphic and hydraulic conditions causing railway embankment breach due to inundation flow. *Journal of Hydroscience and Hydraulic Engineering*, **30**, 87–99.

Tsubaki, R., Bricker, J.D., Ichii, K. and Kawahara, Y. (2016). Development of fragility curves for railway embankment and ballast scour due to overtopping flood flow. *Nat. Hazards Earth Syst. Sci.*, **16**, 2455–2472. https://doi.org/10.5194/nhess-16-2455-2016

Tsubaki, R., Kawahara, Y., and Ueda, Y. (2017). Railway embankment failure due to ballast layer breach caused by inundation flows. *Natural Hazards*, **87**, 717–738. https://doi.org/10.1007/s11069-017-2789-3